Dynamics of a Tidal Estuary

BSc. J.P. de Boer

Engineering Mechanics
Kungliga Tekniska Högskolan
Stockholm

supervisors
Prof. H. Alfredsson
Prof. dr. L.R.M. Maas
Dr. J. Nauw
MSc. S. Groeskamp

Texel, December 13, 2010

This page intentionally left blank.

Preface

This thesis is the result of 8 months work at the NIOZ institute for sea research, at which I performed my Master's thesis.

In 2004 I started with my (Bachelor) studies of Mechanical Engineering at Eindhoven University of Technology (TU/e). During this broad orientation I found out that the field of fluid mechanics drew my attention the most. Especially numerical models, with which I worked during my Bachelor's thesis on boundary layer stability.

To combine the experience of living abroad and have more concrete courses on fluid mechanics, I applied for the Master in Engineering Mechanics at the Royal Institute of Technology (KTH). From 2008 I studied both courses on solids as well as fluids, but now choosing as many elective courses related to fluid mechanics as possible. By the course in Turbulence I met Henrik Alfredsson, KTH supervisor of this thesis.

Almost by accident I met Sjoerd Groeskamp (IMAU, Utrecht University) in Stockholm, through which I got in touch with the Royal Netherlands Institute for Sea Research (NIOZ) on the island of Texel, The Netherlands. Although I passed by this institute numerous times during the visits to my family on this island, before I met Sjoerd I had no idea of what interesting research was performed actually. Soon I agreed with Leo Maas (supervisor at NIOZ) on the topic of this final thesis: the dynamics of a tidal estuary.

Contents

1 Introduction **5**

2 Theoretical background **7**
2.1 Tidal Helmholtz resonator 7
2.2 Adding damping 10
2.3 Simple sloping bottom 12
2.4 Inviscid response 12
2.5 Viscous response 14

3 Methodology **16**
3.1 Approach 16
3.2 Measurement site and setup 17
3.3 Bathymetry 20
3.3.1 Depth measurements 20
3.3.2 Assumptions, uncertainties and errors 21
3.3.3 Dimension estimates 24

4 Data **27**
4.1 Data collection 27
4.2 Uncertainties 28
4.3 Data cleaning 29
4.4 Filtering and running-mean averaging 32

5 Results **33**
5.1 Traditional Linear Analysis 33
5.1.1 Harmonic Analysis 33
5.1.2 Fourier Analysis 37
5.1.3 Rotary component spectra 38
5.2 Oscillations in the Mok Bay 47
5.2.1 Attributing resonance 50
5.2.2 Mechanisms for generation of resonance 54
5.2.3 Damping properties 58

6 Self-oscillations **59**
6.0.4 Phase space 60
6.0.5 Simplification and linearization 63

7 Discussion **78**

8 Aknowledgements **79**

A Photographs **80**

B Non-dimensionalization of the Helmholtz equation **83**

C Derivation of the Harmonic Analysis **85**

D Analytic derivation of the inviscid and viscous response **90**
D.1 Inviscid response 90
D.2 Viscous response 91
D.2.1 General solution 92
D.2.2 Exact solution 94

E Nomenclature **96**
E.1 Symbols 96
E.2 Abbreviations 98

Chapter 1

Introduction

Tides have been of great interest and importance in coastal areas for a long time. Not in the least place for fishermen, sailors and navigators who used simple rules of thumb to 'predict' the tide during medieval times (Mooers, 1999). More recently, the interest has shifted towards coastal engineering (harbor management, flooding areas, tidal energy), oceanography (tidal mixing, (Beerens, 1995)) and applied mathematics (Khokhlov *et al.*, 2007). Already in 1908 investigations were done to study 'secondary undulations' of oceanic tides, in the light of basin response to tsunamis (Honda *et al.*, 1908). Some coastal areas like the Baltic and Mediterranean Sea hardly experience tidal elevation, others have semi-diurnal or diurnal tides, which in turn can be amplified in coastal basins (Cartwright, 1999). The Bay of Fundy is the most famous of these, for its tidal difference of 16 meter.

The periodic orbits of the earth, moon and sun have been linked to the tides for many centuries. These orbits range in period from 12 hours (S_2) to 18.6 years (Lunar nodal), resulting in a fixed forcing of the earth's deep oceans. Due to hydrodynamic effects and local bathymetry the frequency content of the tidal wave changes as it approaches shallower seas and coastal basins (Parker, 1991). Prediction at such sites is often done by analyzing the present tidal constituents in water level measurements and extrapolating this behavior into the future.

For shallow estuaries however, such linear prediction of tidal water level elevation might be inappropriate (Maas, 1997). Almost-enclosed tidal basins with a nonlinear bathymetry (i.e. an increasing water surface area for increasing water level) might experience multiple equilibriums (Maas, 1997) or even chaotic behavior (Maas and Doelman, 2001) to the deterministic tidal forcing. Such a nonlinear bathymetry can be a simply triangular (Maas, 1997), hyperbolic (Doelman *et al.*, 2002) or stepwise linear (examined in this thesis) cross section of the bay.

An amplified tidal response can induce increased mixing and flushing of an estuary, being of importance for nutrients, silt deposition and the local

ecosystem (Sanford, 1985).

The aim of this thesis was to investigate the behavior of a co-oscillating estuary (Mok Bay) and to see if any of the theoretical mechanisms of oscillation is present in practice. Current research on coastal co-oscillation characterizes the measurements rather than the underlying mechanism (Khokhlov *et al.* (2007), Frison (2000), Abarbanel *et al.* (1993), Flinchem and Jay (2000)). Concerning the tidal Helmholtz oscillator, most work is theoretical (Maas (1997), Maas and Doelman (2001) or laboratory-experimental Terra (2005)).

Measurements have been carried out and show the presence of oscillations with a frequency one order higher as compared to that of the tidal forcing. Water level oscillations are two orders of magnitude smaller than the tidal elevation; the oscillating flow at the bay's entrance is almost of the *same* order of magnitude as the tidal flow.

A simplified analytic model of the Mok Bay (viscous, forced, stepwise-linear Helmoltz resonator) has been set up to extend the bathymetries which have been implemented in tidal Helmholtz oscillators so far, in the search for nonlinear behavior. The stepwise bathymetry introduces a stepwise-linear restoring force and consequently the possibility of self-oscillations in the basin. This dynamic system is to some extent comparable to a Duffing-oscillator (where the restoring force changes sign instead of magnitude) for which nonlinear (chaotic) behavior is known to exist (Kreuzer *et al.*, 1991). Simulations for different parameter settings showed period-adding bifurcations (nonlinear and possibly chaotic behavior) but do need further research.

Chapter 2

Theoretical background

The theoretical base of this thesis is the principle proposed by Maas (1997) that a basin can experience multiple equilibriums or even chaotic behavior to deterministic forcing. This chapter will show the complete derivation for an inviscid Helmholtz oscillator (a frictionless almost-enclosed bay) and its corresponding behavior. After this, friction will be included but further details regarding that derivation are left out: the analytic base of an Helmholtz oscillator is shown and only the consequences of the added friction are of interest here.

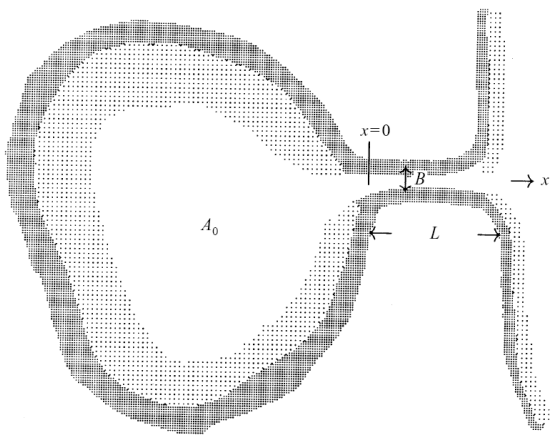

Figure 2.1: Schematic representation of a tidal estuary, showing an almost-enclosed basin connected to a tidal sea by a small channel (from Maas 1997).

2.1 Tidal Helmholtz resonator

A simplified model of a tidal estuary ('basin') connected to a tidal sea can be set up as follows. Let H be the maximum depth in the basin, its water

surface area A_*, and B and H be the width and depth of the connecting strait respectively, see figure 2.1. The vertical coordinate z_* is measured depth upward from the mean water level.

A first assumption is that the basin's length scale $A_0^{1/2}$ and the strait's length L are much shorter than the tidal wave length λ. The tidal wave is now expected to travel instantly through the basin and water level elevation will be in unison. Here $A_0 = A_*(0)$ is the basin surface at $z_* = 0$, the tidal wavelength $\lambda = 2\pi c/\sigma_e$ (where c is the wave velocity) and the lunar semi-diurnal frequency $\sigma_e = 1.4 * 10^{-4}$ rad s^{-1}.

The external tidal elevation at sea $\zeta_e(\sigma_e t_e)$ is a periodic function of time t_e and will be the forcing of the system in the following. In the case of a relatively broad basin, the momentum equations are reduced to lowest order and the horizontal pressure gradient vanishes. This implies that horizontal gradients in surface elevation vanish too and the response will be dominated by a *spatially uniform* Helmholtz mode.

The parameter describing the state of the system is taken to be the excess volume of water in the basin, i.e. the volume added to mean sea level state. This excess volume is defined as $V_* \equiv \int_0^{\zeta_i} A_*(z_*/H_*)dz$. The change of excess volume is related to the volume flux through the strait

$$\frac{\mathrm{d}V_*}{\mathrm{d}t_*} = -u_0(H + \zeta_0)B, \tag{2.1}$$

where the subscripts 0 indicate evaluation at the entrance of the basin ($x = 0$). Furthermore, $u(x, t_*)$ is the depth-averaged flow along the channel and $\zeta_*(x, t_*)$ is the surface elevation within the strait. The flow through the strait is described by the momentum equation

$$\frac{D\mathbf{u}}{Dt} = -\frac{1}{\rho}\nabla p + \nu\nabla^2\mathbf{u}, \tag{2.2}$$

to which the Reynolds decomposition will be applied according to Pope (2000). This decomposes the instantaneous velocity and pressure (u and p) into their ensemble averages $\langle u\rangle$ and $\langle p\rangle$, and the fluctuations

$$\mathbf{u}' = \mathbf{u} - \langle\mathbf{u}\rangle \tag{2.3}$$

$$p' = p - \langle p\rangle. \tag{2.4}$$

The material derivative in (2.2) can be expanded (using tensor notation) as

$$\frac{Du_j}{Dt} = \frac{\partial u_j}{\partial t} + \frac{\partial}{\partial x_i}(u_i u_j), \tag{2.5}$$

which has the mean

$$\langle\frac{Du_j}{Dt}\rangle = \frac{\partial\langle u_j\rangle}{\partial t} + \frac{\partial}{\partial x_i}\langle u_i u_j\rangle. \tag{2.6}$$

Substituting (2.3) yields

$$\begin{aligned}\langle u_i u_j \rangle &= \langle \left(\langle u_i + u_i' \right) \left(\langle u_j \rangle + u_j'\right) \rangle \\ &= \langle \langle u_i \rangle \langle u_j \rangle + u_i' \langle u_j \rangle + u_j' \langle u_i \rangle + u_i' u_j' \rangle \\ &= \langle u_i \rangle \langle u_j \rangle + \langle u_i' u_j' \rangle.\end{aligned}$$

The derivative of the first term on the RHS can be expanded to

$$\begin{aligned}\frac{\partial}{\partial x_i} \langle u_i \rangle \langle u_j \rangle &= \langle u_i \rangle \frac{\partial}{\partial x_i} \langle u_j \rangle + \langle u_j \rangle \frac{\partial}{\partial x_i} \langle u_i \rangle \\ &= \langle u_i \rangle \frac{\partial}{\partial x_i} \langle u_j \rangle,\end{aligned}$$

using the continuity equation ($\partial \langle u_i \rangle / \partial x_i = 0$). The ensemble average of the material derivative can now be written as

$$\begin{aligned}\langle \frac{Du_j}{Dt} \rangle &= \frac{\partial \langle u_j \rangle}{\partial t} + \frac{\partial}{\partial x_i} \left(\langle u_i \rangle \langle u_j \rangle + \langle u_i' u_j' \rangle \right) \\ &= \frac{\partial \langle u_j \rangle}{\partial t} + \langle u_i \rangle \frac{\partial \langle u_j \rangle}{\partial x_i} + \frac{\partial}{\partial x_i} \langle u_i u_j \rangle.\end{aligned}$$

Here, $\langle u_i u_j \rangle$ represent the Reynolds stresses which are obtained by the decomposition of the flow field. Application of (2.3) to the remaining terms of (2.2) finally yields the mean-momentum equations

$$\frac{\partial \langle u_j \rangle}{\partial t} + \langle u_i \rangle \frac{\partial \langle u_j \rangle}{\partial x_i} = \nu \nabla^2 \langle u_j \rangle - \frac{\partial \langle u_i u_j \rangle}{\partial x_i} - \frac{1}{\rho} \frac{\partial \langle p \rangle}{\partial x_j}. \tag{2.7}$$

For the x-direction (aligned with the channel, $j = 1$) this can be simplified to

$$\frac{\partial u}{\partial t} = -\frac{1}{\rho} \frac{\partial p}{\partial x} - u \frac{\partial u}{\partial x} + \frac{1}{\rho} \frac{\partial \tau}{\partial z} \tag{2.8}$$

The mean flow velocity notation $\langle u \rangle$ is replaced by u and τ represents the shear stresses consisting of a laminar and turbulent part

$$\begin{aligned}\tau &= \tau_{lam} + \tau_{turb} \\ &= \mu \frac{\partial u}{\partial z} - \rho u' v'.\end{aligned}$$

The momentum equation including turbulent stresses (2.8) can be integrated over the channel height $H + \zeta_*$ in order to implement an approximation for the friction:

$$(H + \zeta_*) \frac{\partial u}{\partial t} = -(H + \zeta_*) \frac{\partial g \zeta_*}{\partial x} + \frac{1}{\rho} \left(\int \frac{\partial \tau}{\partial z} dz \bigg|_{z=\zeta} - \int \frac{\partial \tau}{\partial z} dz \bigg|_{z=-H} \right), \tag{2.9}$$

where also the pressure gradient due to water level elevation $p = \rho g \zeta$ is included. Here the first integral on the RHS (evaluated at $z = \zeta$) is the expression for surface stresses, for example wind-stress. Such stress is neglected here and thus set equal to zero. The second integral however, is the shear stress evaluated at the channel bottom. This is related to bottom friction, the vertical transfer of horizontal momentum. Since there is no explicit expression for the Reynolds stresses available, it is approximated by the relation

$$\frac{1}{\rho} \int \frac{\partial \tau}{\partial z} dz \bigg|_{z=-H} \approx k|u|u, \tag{2.10}$$

and now related to the mean flow velocity u. In this, k is the bed-stress coefficient and $k \approx 0.0025$. Dividing the obtained result by $(H + \zeta_*)$ yields

$$\frac{\partial u}{\partial t} = -\frac{\partial}{\partial x}(g\zeta_* + \frac{1}{2}u^2) - \frac{k}{H + \zeta_*}|u|u. \tag{2.11}$$

After integration in the vertical direction (2.11) is now integrated over the channel length L. This results in the final expression containing only known quantities and system parameters. Because the flow velocities just outside the channel are different, a pressure gradient over the channel is present. The integration is thus performed from $x = 0^-$ to $x = L^+$ to include this; the exact derivation of the different velocities (due to spread inflow and jet-like outflow) is shown later.

The expression for the momentum equation applicable to the complete length of the channel (using $t_* = t$ for consistency with Maas (1997)) is found as

$$L\frac{\mathrm{d}u}{\mathrm{d}t_*} = g(\zeta_i - \zeta_e) + \frac{1}{2}(u_i^2 - u_e^2) - L\frac{k}{H}|u|u. \tag{2.12}$$

The surface elevation ζ_* is assumed to be much smaller than H, being no longer present in the last term on the RHS. Practically this means that the channel is modeled as a pipe. The subscripts i and e refer to the evaluation at the interior- and exterior-side of the channel respectively. To include the depth-dependence of the flow, an additional factor can be included in the dynamic pressure term (second term on the right), but is excluded here. The third term in the above expression arises from bottom friction. The modeling of the channel by a pipe also simplifies the expression for the excess volume (2.1) to

$$\frac{\mathrm{d}V_*}{\mathrm{d}t_*} = -uHB. \tag{2.13}$$

2.2 Adding damping

Several processes can be modelled as damping in the current simplified system. Inflow to the channel occurs in a potential-flow-like way; outflow

roughly in a jet-like way. Let δ be an empirical proportionality constant, then a widespread inflow ($u_i > 0$) can be expressed as $u_i = (1-\delta)u < u$. Here, u is the flow velocity in the channel. A jet-like outflow initially keeps its width and thus can be approximated by $u_e = u$, so that for small values of δ, ($0 < \delta \ll 1$), the pressure difference can be expressed as

$$\frac{1}{2}(u_e^2 - u_i^2) = \frac{1}{2}u^2 - \frac{1}{2}[(1-\delta)u]^2 = \frac{1}{2}\left(2\delta u^2\right) + \mathcal{O}(\delta^2) \approx \delta u^2. \tag{2.14}$$

Note that ρ was already eliminated from the momentum equation. For reversed flow ($u_i < 0$), $u_i = u$ and $u_e = (1-\delta)u$ so that this contributes as -δu^2. The dynamic pressure difference can thus be implemented as $-\delta|u|u$. Since this form is similar to the term of bottom friction, they will be combined in the following.

Apart from the dynamic pressure drop and bottom friction, also radiation of waves into the sea adds to the damping of the system, albeit linearly. When the oscillating motion is amplified inside the basin, waves transmit energy from the basin back to the sea. Not only does this influence the damping, by making the sea oscillate the 'mass' in the system increases: the effective length of the channel L increases as

$$L_E = L - \frac{B}{\pi}\left[\ln\left(\frac{\pi B}{\lambda}\right) + \Gamma - 3/2\right] \tag{2.15}$$

In this expression, Γ is Euler's constant ($\Gamma = 0.5772\ldots$). Increasing the channel length (involved mass) reduces the Helmholtz frequency, as can be seen in the following expression for the Helmholtz frequency σ_H. The additional linear damping by radiation will then be visible too.

Non-dimensionalizing is done by using $z_* = Hz$, $\zeta_i = H\zeta$, $A_*(z_*/H) = A_0 A(z)$, $V_* = A_o HV$, where the non-dimensional excess volume V now is expressed as

$$V \equiv \int_0^\zeta A(z)\mathrm{d}z. \tag{2.16}$$

Also, $\zeta_e = HZ_e$ and $t_* = t/\sigma_H$, where the Helmholtz frequency σ_H (in rad/s) is

$$\sigma_H^2 = gHB/A_0 L. \tag{2.17}$$

Substitution of the above into (2.12) and (2.13) results in the following expression for the Helmholtz resonator in terms of the excess volume $V(t)$:

$$\frac{\mathrm{d}^2 V}{\mathrm{d}t} + \zeta(V) = Z_e(\sigma t) - r\frac{\mathrm{d}V}{\mathrm{d}t} - \gamma\left|\frac{\mathrm{d}V}{\mathrm{d}t}\right|\frac{\mathrm{d}V}{\mathrm{d}t}. \tag{2.18}$$

Here, $Z_e = F\cos(\sigma t)$, the radiation damping coefficient $r = \sigma B/2L$, $\gamma = (\delta/L + k/H)A_0/B$ is the combination of both quadratic damping terms (Maas, 1997). The complete process of non-dimensionalizing the expression

for the Helmholtz resonator in terms of the excess volume $V(t)$ can be found in Appendix B.

In this expression, the separate terms can be interpreted as follows. The evolution of the excess volume $V(t)$ in the basin is driven by the difference between the tidal forcing (first term on RHS) and the (restoring) water level *overshoot* (second term on LHS). The two negative terms on the right hand side represent the dissipation of system energy. This is, the radiation of waves back to the tidal sea (linear, second term on RHS) and the combined bottom friction and pressure difference over the channel (quadratic, third term on RHS).

2.3 Simple sloping bottom

For a basin with uniform water surface area, the non-dimensional excess volume is $V = \zeta$ since $A(z) = 1$. The restoring force is thus linear in this case. For many basins in the Wadden Sea, including the Mok Bay, the bottoms are sloped. Consequently, a nonlinear restoring term is formed in the momentum equation.

A simple form of a sloping bottom, is one with surface area increasing linearly with height. Using non-dimensionality again, the largest depth of the basin is at $z = -1$. Also, $A(0) = 1$. This results in the simple expression for area

$$A(z) = 1 + z. \tag{2.19}$$

Note that having a depth H which is not constant any longer, an *effective* depth should be used in determining the Helmholtz frequency σ_e. From (2.16), the excess volume is

$$V = \zeta + \zeta^2/2. \tag{2.20}$$

This relation can be inverted as

$$(\zeta + 1)^2 = 1 + 2V \quad \longrightarrow \quad \zeta(V) = (1 + 2V)^{1/2} - 1 \tag{2.21}$$

which will be used as the non-linear restoring force in (2.18) in the following.

2.4 Inviscid response

Recall the equation for a Helmholtz resonator, (2.18), which can be made inviscid by simply using $r = \gamma = 0$. Substituting (2.21), this becomes

$$\frac{\mathrm{d}^2 V}{\mathrm{d}t^2} + (1 + 2V)^{1/2} - 1 = Z_e(t). \tag{2.22}$$

Even though an inviscid tidal resonator will not be found in nature, it is interesting to have a look at this idealized model. For example, the amplitude of a *linear* inviscid (undamped) oscillator tends to infinity. A nonlinear

oscillator on the contrary is not necessarily singular, since it detunes itself at amplification. Possibly, this results into multiple equilibria (and even chaotic behavior) since the system might jump between different states.

In a numerical integration of (2.22), Maas (1997) found that for a fixed forcing (both frequency and phase) the corresponding oscillation is modulated slowly. A system near resonance has an amplified response, which in turn changes the system itself. This now leaves its resonance-state and experiences in turn a less amplified response, returning to the old state. This quasi-periodic behavior was not only found for forcing at the Helmholtz frequency σ_H, but also for $2\sigma_H$.

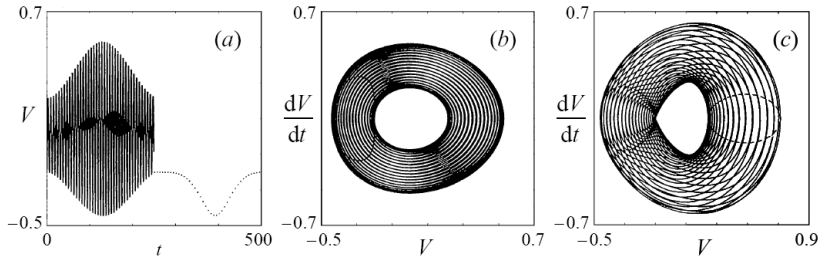

Figure 2.2: (a) Numerical integration of the inviscid forced evolution equation for the basin's excess volume V, demonstrating resonant growth, natural detuning and subsequent decay. (b) Phase-space trajectory of this solution and (c) with different initial conditions (from Maas 1997).

Figure (2.2) should be interpreted as follows. In (a) the response in time of the modelled system is shown, one modulation period as full response, the second modulation period only as a stroboscopic plot. For this stroboscopic part a frequency equal to the forcing frequency is used, resulting in one dot per period. In (b) a series of these stroboscopic 'dots' forms a trajectory within fixed bounds, shown in *phase-space*. Phase-space representation is a standard way of presenting self-similarities in periodic signals Cvitanovic (1983). Finally, (c) has different initial conditions for the system as compared to (b).

Switching between states was suggested by observations of Golmen *et al.* (1994), who observed a modulation of a resonance-like pattern in the Norwegian Moldefjord. This fjord can be regarded as a deep, almost-enclosed tidal basin. Especially in current measurements a *super-tidal* frequency was found, with evolving amplitude. The frequency of forcing was thus much larger than the observed 'resonance', i.e. $\sigma \gg 1$. Whether these observations can be attributed to chaotic behavior is unclear.

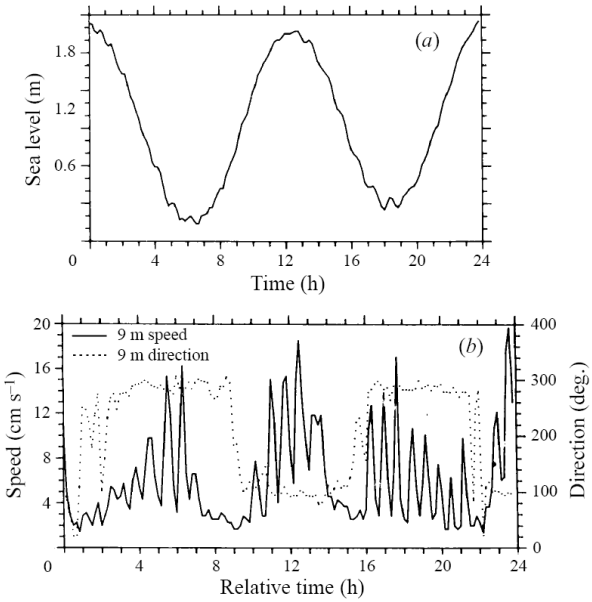

Figure 2.3: Irregular observed sea level (a) and current (b) observations over time in Moldefjord, Norway (from Golmen *et al.* 1994).

2.5 Viscous response

Now both energy dissipating terms will be included, as a more realistic approximation requires. Numerical integration of (2.18) using the sloping bottom as in (2.21) yields a steady state response to the fixed forcing. Although the steady state depends on the frequency of forcing, it does not necessarily have *one* response state. In the following, the amplitude response curve for the analyzed system is derived, from which *multiple equilibriums* appear for forcing close to the system's eigenmode.

Assuming only small changes in excess volume, forcing and friction, one can scale (2.18). More specific, $V \to \epsilon V, r \to \epsilon^2 r, \gamma \to \epsilon^2 \gamma$ and $F \to \epsilon^3 F$ (where $\epsilon \ll 1$) will result in an equation where damping, forcing and nonlinearity all appear at the same order in the perturbation scheme. Skipping intermediate steps, the solution up to second order is then given by

$$V = \hat{V}\cos(\sigma t - \phi) + \frac{1}{4}\epsilon\hat{V}^2\left[1 - \frac{1}{3}\cos\left(2(\sigma t - \phi)\right)\right] + \mathcal{O}(\epsilon^2). \tag{2.23}$$

The response is clearly phase-locked and from the steady-state amplitude and phase the frequency-response curve is (leaving further derivations out) presented as

$$\omega = \frac{1}{12}\hat{V}^2 \pm \frac{1}{2}\left\{\left(\frac{F}{\hat{V}}\right)^2 - \left(r + \frac{8\gamma}{3\pi}\hat{V}\right)^2\right\}^{1/2}. \tag{2.24}$$

This characteristic (see figure 2.4) shows that for certain parameter values two possible equilibrium amplitudes can be found in the response, while experiencing fixed forcing. On such 'resonance horn' two stable equilibriums are found (A,C) and one instable (B).

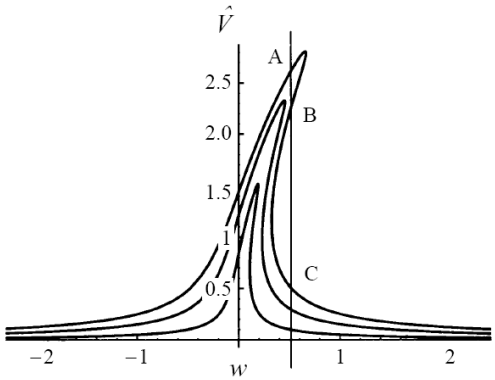

Figure 2.4: Amplitude response $\hat{V}$-curves against detuned frequency $\omega \equiv (\sigma - 1)/\epsilon^2$ (with $\epsilon \ll 1$ the detuning parameter). For cases of near-resonant forcing, $\sigma \approx 1$, it has bent 'resonance horns' indicating multiple equilibriums and an increased response when F increases from 0.1 to 0.3 and 0.5, for frictional parameters $r = \gamma = 0.01$. Near $\omega \approx 0.5$ three equilibriums, A, B and C, are obtained where the vertical line intersects the amplitude-response curve (for $F = 0.5$). The smallest and largest of these intersections are stable and correspond to a choked (C) and amplified (A) regime respectively. (from Maas 1997)

If one approaches the frequency $\omega \approx 0.5$ from a lower frequency, the system will experience the response amplitude at A. On the contrary, when approaching from a higher frequency (say, $\omega = 1$), the response amplitude at C will be found. Such possibility of different responses is called *multiple equilibriums* (Nayfeh and Mook, 1979). For only minor changes in system state such sudden jump can take place, being a first step to unpredictable (chaotic) behavior (Maas, 1997).

Chapter 3

Methodology

3.1 Approach

As the title of this thesis implies, part of the behavior of the estuary will be caused by the tidal forcing outside the estuary. An important distinction between the mathematical descriptions of different tidal estuaries can be made based on their shape: the size of their connection to the tidal sea.

Mainly open bays

A mainly open bay (i.e. with a wide connection to the tidal sea) can respond as a so-called quarter-wavelength resonator (Rabinovich, 2009). The lowest eigen-mode of a mainly open bay corresponds to the motion of a quarter wavelength inside the bay, always having a node at the entrance. Standing waves have their largest flow velocity at the nodes, here being the entrance of the bay. For a lake, in fact being a completely enclosed bay, similar standing-wave modes are called 'seiches' (and in fact half-wave oscillations). When forced at one (or more) of such eigen-frequencies, the bay or lake will start to resonate.

Almost-enclosed bays

Harbor oscillations are named after the oscillations in typical almost-enclosed bays: harbors. The fundamental mode is now the so-called *Helmholtz mode*. Equal elevation of the water level will occur throughout the bay, resulting in a pumping motion at the entrance. This distinct difference in surface elevation –a fixed node at the entrance or equal surface elevation– makes it possible to distinguish between the two types of oscillatory motion.

As will be shown later, the restoring force in the system of a Helmholtz resonator is related to the bay's water surface area. If this area is not constant during a change in water level, a non-linear relation occurs (Maas,

1997). For the Mok Bay (and other basins in the Wadden Sea) this is the case, resulting in non-linear behavior, possibly even chaotic.

3.2 Measurement site and setup

To investigate the dynamic properties of the Mok Bay, measurements will be performed at two different locations. The water level should be measured at the head and mouth of the bay in order to distinguish the two above mentioned types of resonator. Photographs about the used setup, installation of the equipment and performed measurements can be found in Appendix A.

A global view of the location of the Mok Bay can be found in figure 3.1, the specific locations of measurement are shown in figure 3.7.

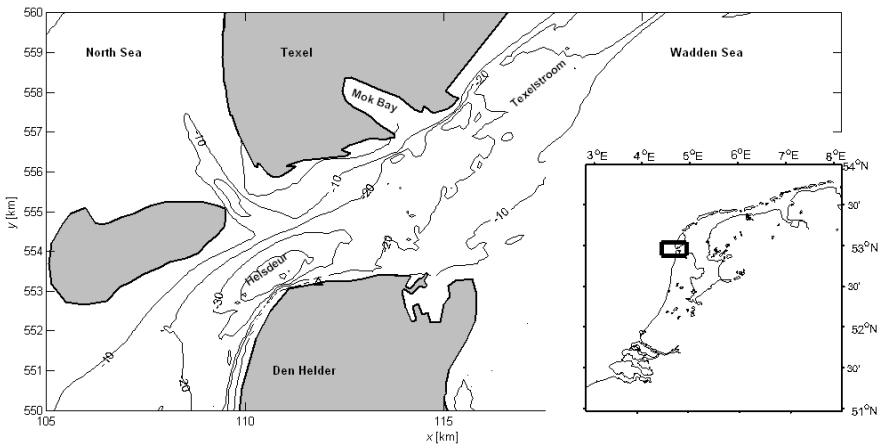

Figure 3.1: Location of the Marsdiep inlet (main panel) in the Dutch coast (bottom right panel), connecting the North Sea to the Wadden Sea. The Mok Bay on the Southern part of the island Texel is in turn connected to the Marsdiep inlet. The Marsdiep bathymetry is shown in 10-meter contour lines, relative to mean sea level.

The moored frame - MK2

A frame is moored at the bottom of the entrance of the ship route into the Mok Bay. An Acoustic Doppler Current Profiler (ADCP) is mounted on the aluminum frame, which is filled with lead. Furthermore, it is connected by a steel cable to a beacon named *MK-2* and owned by the Ministry of Public Works and Water Management (Rijkswaterstaat). This steel cable avoids any tension in electronic wires connected to communication electronics, mounted at the MK-2 beacon.

The ADCP measures the water current profile in the whole column of water in sight of the ADCP. Here, the ADCP is facing upward and thus

measuring from bottom to the water surface. The principle of measurement is based on the acoustic backscatter to determine the Doppler based velocity. Backscatter occurs from solvents and particles carried by the water. The resulting Doppler shift of the four spread ADCP beams is decomposed into a vertical and two horizontal velocity components. A specific time interval in the received acoustic backscatter corresponds to the reflections at a certain distance from the ADCP. This allows to resolve the velocity over the complete water column in sight of the ADCP, being the major advantage as compared to a traditional (single point) current meter. For internal calculations, the temperature and depth are measured by the ADCP.

Depth meter - Mok Harbor

Mok Harbor is located at the head of the Mok Bay, see figure 3.7. At high water this is not the furthest point, but it is during low water. Because of this, the relatively deep ship route that ends in the Mok Harbor is expected to have large contribution to the bay's behavior. Consequently, an identical pressure sensor is mounted inside the Mok Harbor to find any phase delay in water level. The pressure sensor measures pressure relative to the ambient air by using a thin reference tube that extends above the water surface. Atmospheric pressure differences are now ruled out and only differences in water level cause a pressure difference. From here on, the pressure meter is referred to as depth meter.

Communication and recording

As an experiment, communication between the two sites of measurement and the NIOZ institute was done by two wireless CPE Ethernet bridges instead of local data storage. These LAN-bridges work as long as the devices are in optical sight of each other: if the chain is broken on one place the complete communication 'downstream' is blocked. The NIOZ institute is the location of the main computer and thus defined as the 'upstream' edge. The first bridge was formed from the NIOZ institute to the MK-2 beacon (communication with the moored frame), the second bridge from the MK-2 beacon to the Mok Harbor.

The purpose of such set-up is twofold. It allows to directly read the measured data and to detect instrument failure. Also, for the ADCP communication *to* the sensor is possible: instrument settings can be changed on distance using the main storage computer. Especially in the first week of measurements different setups for ADCP-settings were planned to be tested, to find an optimum in power consumption, accuracy and sample rate among others. The main properties of the used instrumentation can be found in table 3.1, properties of the NIOZ Jetty pressure sensor are available upon request.

Instrumentation		Depth $[m]$	Vel. $[m/s]$	Temp. $[°C]$
Workhorse	*Range*		± 5	$-5 - 45$
Rio Grande	*Acc.*	N/A	± 0.005	± 0.4
	Res.		0.001	0.01
Keller	*Range*	$0 - 3$	N/A	$0 - 50$
0.3bar/8935	*Acc.*	N/A	N/A	N/A
	Res.	0.01	N/A	0.01

Table 3.1: Instrumentation properties (working range, accuracy and resolution) of the setup as used during the measurements from February 25th to March 6th. Measured quantities are depth, velocity and temperature. Note that depth (or, pressure) is not measured directly by the ADCP and consequently no properties are available (N/A). Instruments and application: Workhorse Rio Grande (ADCP) and Keller PR-46XH/0.3bar/8935 (depth meter).

To resolve the tidal behavior of the Mok Bay to a good approximation, the largest tidal constituents and their modulation should be measured for at least a few periods. The largest constituents in the Marsdiep inlet are M_2 and S_2, which are modulated with a 14.76-day cycle (M_{sf}) (Buijsman and Ridderinkhof, 2007). This constituent is in turn modulated by a 7-month period, being too long to resolve in measurements during this thesis. The desired time of deployment was set to be two months, both to capture the 14-day cycle more then once and to be able to find the best ADCP settings in practice.

Overconsumption by communication electronics made this impossible though. The available battery capacity could power this setup for only one month. Apart from this, a higher discharge rate reduces the capacity even more. When discharging the batteries at a rate larger than 25 mA, the capacity is not the rated 19000 mAh, but drops to 15000 mAh. Furthermore, the low temperature decreased the capacity to 11000 mAh at a temperature of about zero degrees. In the end, the battery pack powered the setup for only 9 days, which can be explained by the above and the fact that the batteries were already five years old. Table 3.2 summarizes the estimated power consumption of the individual components of the measurement setup. Different load cases illustrate the gap between the expected and final output capacity that powered the setup for only 9 days.

Other mounted instruments were an OBS (optical backscatter) and CTD (conductivity, temperature, depth meter) to investigate any possible relations with sediment, salinity and/or temperature. The CTD suffered from failure within two days and the short time of deployment shifted the focus of the research to water level and flow measurements, leaving the OBS (sediment) and CTD (salinity, temperature) out of further consideration.

Water level measurements from the NIOZ Jetty (less than 500 meter

Consumption					
	q	$[A]$	$[V]$	$[Wh]$	$[mA]$
ADCP	1	0.10	14.0	1010	
OBS	1	0.02	14.0	202	
Depthmeter	1	0.01	14.0	101	
T/R-unit	2	0.25	14.0	5040	
UDS	2	0.10	12.0	173	
Hub	1	0.10	12.0	864	
Total				*8930*	*29.5*

Capacity	Load case		Output		
	$[°C]$	$[mA]$	$[Ah]$	$[Wh]$	$[d]$
TekCell	20.0	1.00	19.0	266	
	0.00	1.00	18.5	259	
	0.00	29.5	11.0	154	
(30 × 4pack)	20.0	1.00		7980	26.8
(30 × 4pack)	*0.00*	*29.5*		*4620*	*15.5*

Table 3.2: Total power consumption of electronics mounted at the MK-2 beacon and moored frame (top) and battery capacity for different load cases (bottom). The CTD has its own power supply and is not listed. Communication electronics (quantity q) consume the most power by far (85%): osBridge transmitter/receiver (T/R-unit), universal device server (UDS) and communication hub. Assumed time of power consumption: 30 days (720 hours). Battery capacity calculated for TekCell SB-D02 ($3.5V$, Lithium-ion D-cell), assembled as 4-pack ($14V$). Note the decrease in battery capacity (Ah) due to the increased applied load (mA), and consequently the reduced time of employment (d).

separated from the MK-2 beacon) will be used to determine long-term tidal behavior, local events will be looked for in the 9-day spanning data set.

3.3 Bathymetry

3.3.1 Depth measurements

Depth measurements of the Mok Bay are available from both the Ministry of Public Works and Water Management (Rijkswaterstaat) measured in 1998 and by Stema Survey Services B.V. (measured 2009), after the ship route was dredged. The 1998 measurement covers the shallow part of the bay, in 0.20 meter steps, the 2009 measurement covers only the dredged ship route. Since the shallow part is roughly that part that floods during high water, it is as important as the ship route itself in determining the hypsometric curve of the bay: the increase of water surface area as function of water level.

The quickest and still an accurate way of charting the Mok Bay's depth

was by means of the jet ski that the Delft University of Technology (TUD) equipped with an echo sounder. Not only their horizontal position (x- and y-coordinates) was measured by GPS, but a satellite-correction made localization in the (vertical) z-direction possible. Despite the shallow depth of the jet ski itself, the blanking distance of the echo sounder (1.20 meter) made it impossible to measure the shallow part of the bay (shown in red in figure 3.2).

Using a hand-held GPS and the NIOZ Jetty Pier water level measurements as a reference, the shallow part of the Mok Bay was charted. The main assumption is that the water level at the NIOZ Jetty is equal to the water level within the Mok Bay. Standing at the waterline within the bay at the instant the water level at the Jetty is at +0 N.A.P., the current position given by GPS corresponds to +0 N.A.P. within the bay. Aligning the GPS-tracked waterline and the water level measurements of the Jetty in time, a complete correction for the z-coordinate of the walked x- and y-coordinates can be made. Having this, the waterline's level relative to N.A.P. can be traced from ebb to flood (or vice versa) and by walking along it, the depth of the complete bay can be charted. The GPS device stores its position every 5 seconds and a typical average walking velocity was 1.27 meter per second, resulting in a measurement (roughly) every 6.35 meter. This allowed to capture small creeks and ponds fairly well, without running out of memory.

About 52.1 kilometer of waterline is tracked with the hand-held GPS and the jet ski track covers about 21.0 kilometer. The combined result of all depth measurements is shown in figure 3.2. Since tidal banks flood in a short amount of time, the spatial density of the waterline-tracked paths is not constant throughout the bay, see figure 3.3. The bird reservate in the most Northwestern part of the Mok bay resulted in lack of measurements, whereas oyster beds could not be walked around just Northwest of the center of the bay. It is almost impossible to stand on the bottom next to the beds due to the silt, the razor sharp edges of the oysters are another danger.

3.3.2 Assumptions, uncertainties and errors

As described above, not every part of the Mok Bay is covered by the jet ski measurements or GPS-tracked water lines. Especially the Northwestern part lacks localization measurements of the flood line. The available coastline from Rijkswaterstaat is used to define the outermost edge of the bay and is set to +1 N.A.P. At interpolations, the profile of the bay is assumed to increase linearly to this edge. At this edge the boarders are steep and no further increase in water surface area is found. Another important assumption is that there is no significant time delay between high (or, low) water at the NIOZ Jetty and the water level inside the bay as tracked using the GPS device. Figure 3.4 shows that there indeed is no significant difference, except for a few centimeters at the quick flooding during flood phase. This

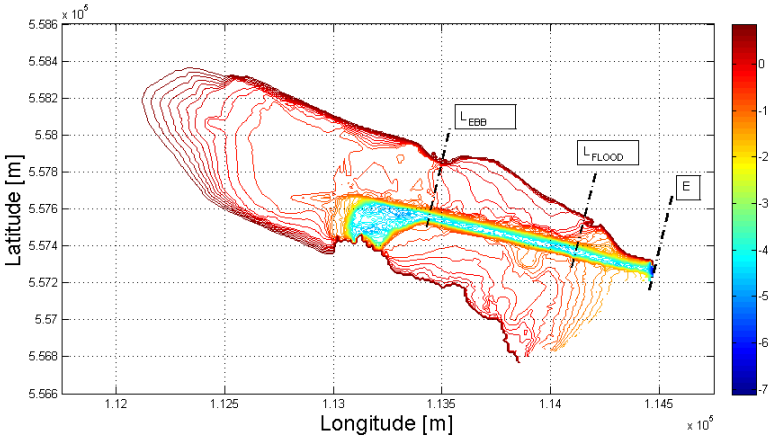

Figure 3.2: Top view of the Mok Bay, containing depth contours estimated from all depth measurements, relative to N.A.P. (Amsterdam Reference Level). Broken lines indicate the location of the Mok Bay's entrance (E) and the length of the channel during low- (L_{EBB}) and high water (L_{FLOOD}). All wet area Northwest of such L_i contributes to A_0 as listed in table (3.3).

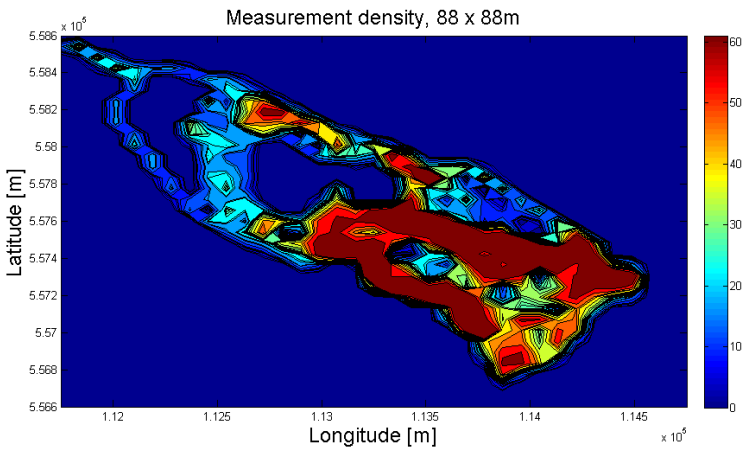

Figure 3.3: Measurement density throughout the Mok Bay. The measurement density as defined here is the number of GPS-located depth measurements per 88 by 88 meter. Jet ski measurements performed in the ship route result in a high measurement density by the closely aligned measurement paths. Tracked water lines at the (flat) tidal banks result in a low measurement density. Two areas are not covered (density: 0) by GPS-tracked waterlines: the bird reservate at the complete head of the bay and an oyster bed at 5.5775e5 N, 1.1275e5 E, in meter from Paris.

allows to link a position of the waterline inside the Mok Bay to a water level measurement at the Jetty. Apart from this last assumption, still an offset between both data sets is present, as will be shown later.

Uncertainties occur in the localization by the GPS, but are expected to be of $\mathcal{O}(1m)$ and consequently not significant. Typical length scales of creeks, ponds and oyster beds is one order of magnitude larger. The

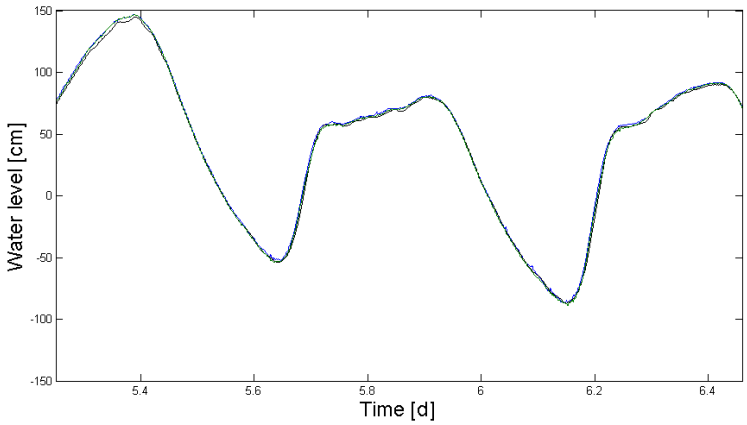

Figure 3.4: 1-Day fragment of water level measurements from the Mok Harbor (black), MK-2 mooring (blue) and NIOZ Jetty (green). Oscillations at the Mok Harbor and the absensce of any significant time delay are visible. Time relative to ADCP start-up.

GPS-tracked water line is walked by multiple persons, possibly interpreting 'waterline' slightly different. The definition of waterline is clear when the slope of the beach is visible, but less clear when rough parts of the beach flood slowly. Interpolation between the tracked waterlines, the skipped bird reservate and between jet ski and waterline tracks is linear and brings uncertainties especially over larger distances.

The main errors can be found in the estimation of the water area of the Mok harbor, which is not included in the jet ski or walked paths. From the chart after dredging by Stema Survey this area is estimated to be 7500 m^2 but might differ due to the difficult shape of the bay. As stated earlier, the bird reservate and the oyster bed in the Northwestern part of the Mok Bay are large surfaces that are simply interpolated, while in fact being little hills or ponds within the bay. Finally, the Mok Bay has no distinct separation from the Wadden Sea. The sudden increase of depth at the ship route is set to be the 'entrance', the jet ski measurements showing depths less than -5 meter N.A.P. are taken to be the boarder with the Wadden Sea.

Another error is found in the overlap between jet ski and GPS-tracked measurements. This error in overlap might be present throughout the complete overlap from jet ski to GPS-tracked depths, but was noticed too late (the combined depth measurements interpolated to a grid does not show a sudden jump) in this thesis to find the cause of. There is no significant time delay from NIOZ Jetty to the Mok Harbor (see figure 3.4) to cause this 20 cm gap, nor was the cut-off frequency of filtering of the NIOZ Jetty data too low to cause this amplitude difference.

This will consequently decrease the accuracy of the estimated bathymetry (the sudden increase of area and volume in figure 3.6 will occur at a lower water level value). For the remainder of this thesis however, this finding is

not significant. At high- and low water the water surface area estimation is still valid, yielding no change in accuracy in the estimation of the Helmholtz frequency.

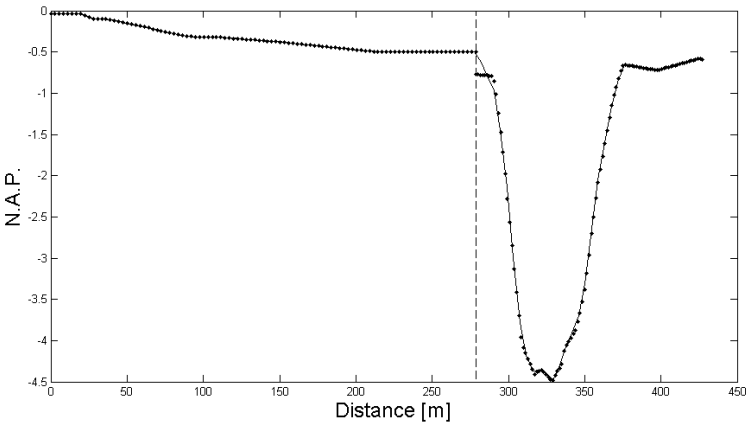

Figure 3.5: Typical cross section of the interpolated water depth of the Mok Bay. Dots indicate interpolated measurements from the GPS-tracked water line (0-280 meter) data set and jet ski data set (280-430 meter), the solid line indicates the interpolation of the combined data set, covering up the gap between the two sets. Intersection from $5.5700 \cdot 10^5$ N $1.13500 \cdot 10^5$ E to $5.5780 \cdot 10^5$ N $1.1375 \cdot 10^5$ E.

3.3.3 Dimension estimates

Using the depth measurements performed by the team from Delft University of Technology, good estimates of the relevant length scales within the Mok Bay are made. The high-density measurements covering the ship route and the connection to the Wadden Sea results in estimates for H, B, L and A_0 at low water (see figure 2.1). The hypsometric curve that is obtained from the GPS-tracked water lines yields the estimate for A_0 at high water. It shows that the water surface area of the Mok Bay increases rapidly from -0.5 meter N.A.P. and higher, see figure 3.6. It is the aim of this thesis to find the consequences of this shape to the Mok Bay's dynamics. An important note is that the area considered to be the bay's 'surface area', is the wet area Northwest of the separation line marked by L in figure 3.2. Although at high water no distinct channel is visible between the 'bay' and Wadden Sea, it is used for modeling in the following chapters.

Dimensions			
	Ebb	*Flood*	unit
H	3.0	5.0	m
B	$44 \pm 10\%$	$54 \pm 10\%$	m
A_0	$9.02 \cdot 10^4$	$1.46 \cdot 10^6$	m^2
L	1050	$300 \pm 10\%$	m

Table 3.3: Estimated dimensions using the combined depth measurements and corresponding theoretical Helmholtz frequency for both ebb and flood state of the Mok Bay.

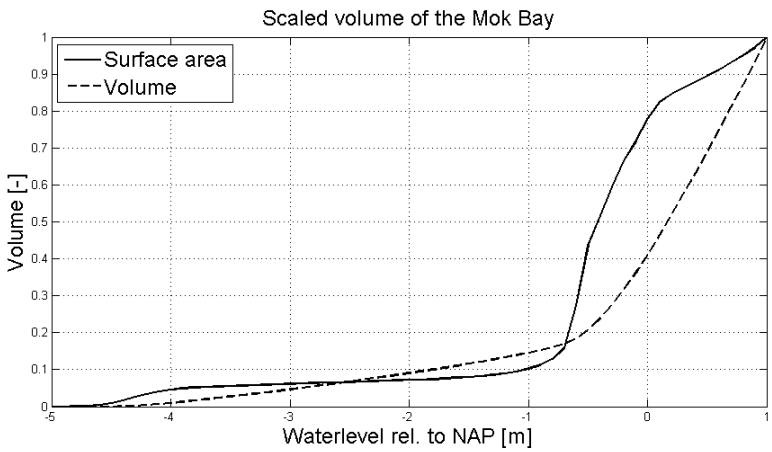

Figure 3.6: Hypsometric curve for the Mok Bay, giving the relation between water level and corresponding water surface area and volume (considering the distinction between bay 'content' and 'connecting channel', shown in figure 3.2) of the Mok Bay.

The Mok Bay in summary

With a typical salinity of $25 - 29$ PSU[1], the Mok Bay can be considered brackish. The fresh water discharge from the Lake IJssel into the Marsdiep (which feeds the Mok Bay) is the major cause for this (Buijsman and Ridderinkhof, 2007), natural run-off of fresh water into the Mok Bay is very small. During the period of measurements the temperature of the sea water was typically $2 - 4°C$ and tidal currents at the mouth of the bay typically 0.3 ms^{-1}. In this range of temperature and salinity, the difference in density was $\pm 0.2\%$. This justifies the assumption that pressure can be used to calculate depth directly, using constant density throughout the measurement period.

[1]PSU: Practical Salinity Unit, defined in terms of the ratio K_{15} of the electrical conductivity of the seawater sample at the temperature of 15 ° C and the pressure of one standard atmosphere, to that of a potassium chloride (KCl) solution, in which the mass fraction of KCl is 32.4356 $\cdot 10^{-3}$, at the same temperature and pressure.

Figure 3.7: Aerial picture of Mok Bay (1999) in Westward direction: at the horizon the North Sea is visible. Vertical arrows indicate the locations of MK-2 beacon (A), TESO Harbor of the ferry to the main land (B), NIOZ Jetty Pier (C), and Mok Harbor(D). The broken white line indicates the ship route inside the Mok Bay, the bold arrow indicates the location and direction in which the picture of figure 5.23 is taken.

Chapter 4

Data

4.1 Data collection

The measurements that extend the theoretical base of this thesis were performed during the early spring of 2010. Two depth meters were placed to recognize and distinguish different resonator models. By measuring the water level at both the entrance and head of the bay, a difference in water level can be quantified. At the entrance of the bay also the velocity profile over the depth is measured: oscillations in surface motion might be more visible in velocity fluctuations, especially in the narrow entrance of the Mok Bay.

In the following one can find the details and consequences of the data collection. The setup ran out of power after nine days (the depth meter at the Mok Harbor was externally powered) so the water level data set was expanded by including measurements from the NIOZ Jetty. The details regarding the time of employment for the individual instruments can be found in table 4.1. Additionally, this chapter describes the uncertainties in the measurements and the first step of post-processing: cleaning and filtering of the collected data.

Time of deployment	Start-up date	End date	Time [d]
ADCP	25/02	05/03	7.7
depth meter, MK-H	25/02	06/03	9.1
depth meter, MK-2	24/02	06/03	11
NIOZ Jetty	19/01	09/03	44

Table 4.1: Time of deployment for the separate instruments during the early spring of 2010. Water level is measured at the moored frame next to the MK-2 beacon (depth meter, MK-2), in the Mok Harbor (MK-H) and (standard) at the NIOZ Jetty, water velocity is measured by means of the ADCP at the moored frame only. The 44-day period of NIOZ Jetty data coincides and extends the period of water level as measured by the two depth meters. Details about the used instrumentation are listed in table 3.1.

4.2 Uncertainties

At every passage of the nearby ferry, the magnetic field of the ferry's steel hull influences the internal compass of the ADCP. This passing is visible as spikes in the *orientation* data, the angle of the ADCP relative to the magnetic North. With a magnitude of about 0.5° this can be neglected, see figure 4.1. Also, during the total time of employment the change in orientation is negligible: $\approx 1°$. This change might be explained by the fact that the heavy lead-filled frame settles in the sand under the influence of the tidal motion in the bay's mouth. The periodic deviation (at 1.75, 2.25, 2.7, 3.25, ... days) might be due to slight movement of the ADCP in its rubber mounting, again under the influence of the tidal current. This has an even smaller magnitude (0.25°) and is neglected as well.

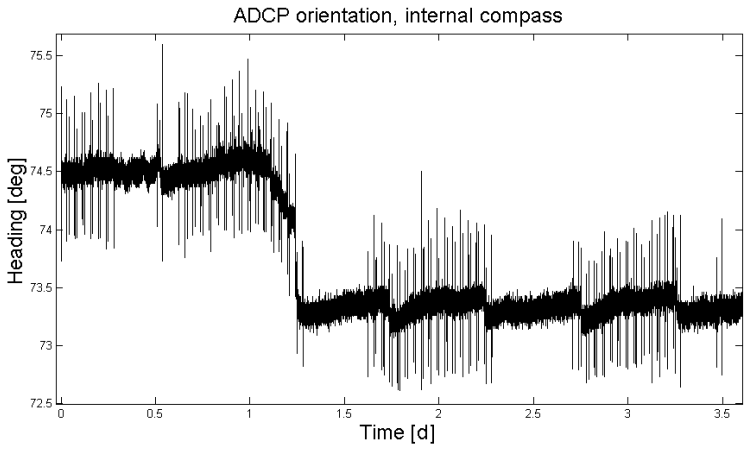

Figure 4.1: Raw output data from internal compass of ADCP. Note the settling of the heavy frame (or ADCP within the frame) after one day from the drop-off, and the influence of the ferry passage to the internal (magnetic) compass. Time relative to start-up of the ADCP.

To avoid difficulties in mounting the depth meters from an anchored ship, no exact depth for mounting the depth meters was specified. This resulted in an unknown offset between the depth meters at the MK-2 beacon and the Mok Harbor relative to the NIOZ Jetty. It is no surprise that the depth meter located at the MK-2 beacon shows practically the same water level measurements (difference from NAP, see figure 3.4) as the NIOZ Jetty, since they are separated by less than 500 meter. The offset relative to the NIOZ Jetty (output relative to N.A.P.) is calculated as the difference of a 7-day mean from both sensors, being -1.70 meter for the depth meter at the MK-2 beacon and -2.24 meter for the depth meter at the Mok Harbor. This assumption neglects the influence of local (temporary) swell in the Mok Bay and any oscillatory motion within the Mok Bay. A longer period of measurements yields a more accurate value for this offset, but for most

parts of the data analysis the *relative* water level is of importance, rather than the absolute level.

4.3 Data cleaning

Passage of the ferry

Every time the ferry to Texel approaches or leaves the Texel TESO harbor, it blocks the transmitted signal. This is not as visible as a data gap but more as spikes in the signal of the depth meters, see figure 4.2. Unrealistic depths are 'measured' at many of such events. These short periods are rejected and are on average 30 seconds in length. For the ADCP data this resulted not in such obvious incidents, which can be explained by the fact that the ADCP sends its data not as often. The depth meter reported its measurements every second, the ADCP averaged its measured values over 6 seconds before reporting it. Spikes that did appear in the measurements were rejected after comparison with a running mean.

In order to remove these spikes from the depth meter data, a running mean was used to compare each following measurement in time. If a following measurement would deviate by more than 10% from the calculated local mean, it was flagged as unrealistic. This value was then replaced by the current mean value, to reduce its influence but still have a equal-spaced dataset. Taking the running-mean window short relative to the tidal time scale ensures that the current mean value is a good replacement.

Although the unrealistic spikes are removed, the waves that appear at each ferry passage are still present. Interestingly, these waves have periods of several minutes and are already visible in the raw data from the depth meter at the MK-2 beacon. They go however beyond the scope of this thesis and are not analyzed.

Reflections in ADCP intensity

Solvents and floating particles reflect the signal that is transmitted from the ADCP transducer faces. Using the Doppler-shift that such particles induce, an estimate of the local flow velocity can be made. The water surface is found as a jump in intensity because the reflection from the surface is much stronger than the reflection from scatterers in the water.

But not just the surface reflects the signal that is sent out from the ADCP, it is reflected by the bottom and surface again too. In this case, the sound has traveled twice the distance before it reaches the ADCP, and a (twice) too large depth measurement is done, see figure 4.3 (upper). Comparison to the depth meters shows that apart from a good estimation, sometimes a 1.5 or 2 times too deep estimate is found. By specifying again a local

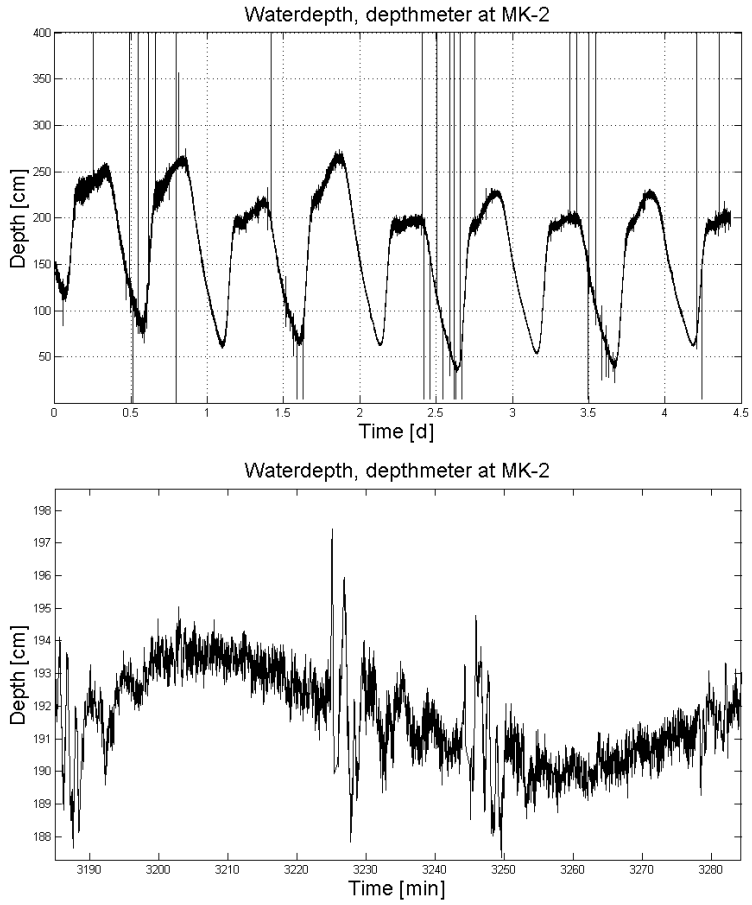

Figure 4.2: Raw (upper) and detail of corrected (lower) depth measurement from Keller depth meter measurements. Spikes due signal blocking by passage of the ferry, and long-period waves visible after ferry passage.

(running) mean, each following measurement in time is compared and divided by 1.5 or 2 depending on the size of the deviation from the mean. Instead of simply rejecting the data, it is now converted into useful data, see figure 4.3 (lower).

Once the depth estimate is finished, this distance is rounded off to the used bin size by the ADCP, here 0.25m. The acoustic backscatter that the ADCP receives is averaged over such bins along each beam and returned as a single value.

Since the transducer faces of the ADCP *ring* a little while after emitting the signal, it is not possible to immediately start recording the received echo signals. This results in a *blanking distance*, a distance in front of the ADCP in which the water velocity cannot be determined. For the used 1200 kHz RDI Rio Grande this blanking distance is equal to 0.25 meter.

A signal sent out at an angle of 20 degrees from the vertical returns at

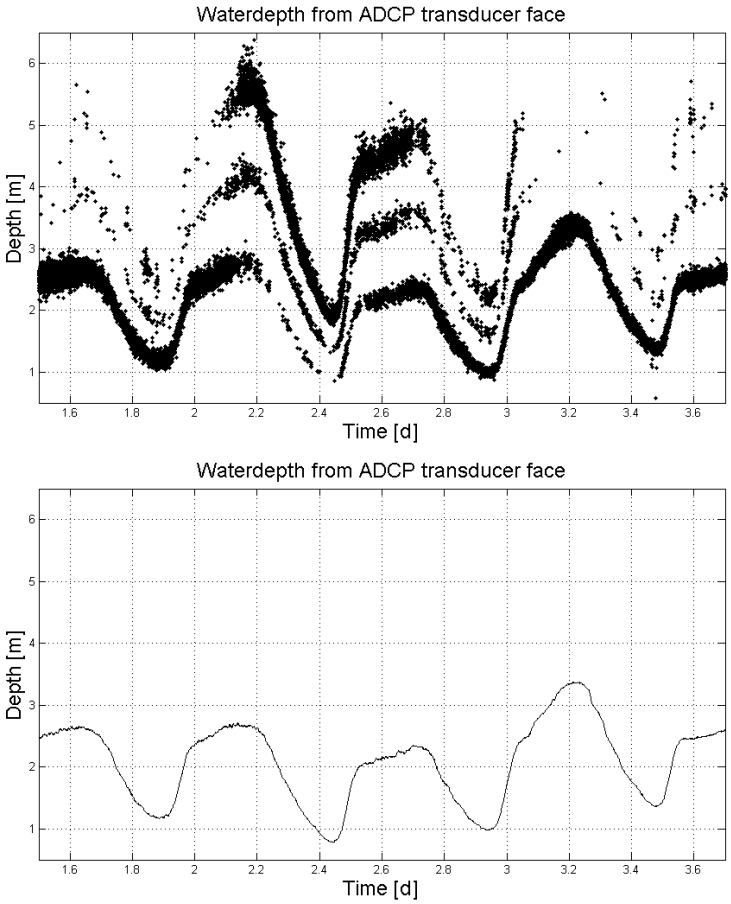

Figure 4.3: Raw (upper) and corrected depth estimate (lower) from ADCP intensity measurements. Reflections by the water surface and bottom are used to estimate the (distance to the) surface water level.

the same time as the (radiated and reflected) signal that travels the shortest (vertical) way to the surface. To avoid confusion between these, the last 6% of the total beam length to the surface should be rejected.

The three-component velocity data in the remaining bins are used for analysis.

Processing of the NIOZ Jetty data

During 7 years the water level, wind speed and direction have been measured continuously and recorded at the NIOZ Jetty Pier. The water level is measured by means of a pressure sensor, recording at approximately 4 Hz. Data reduction is obtained by taking the 1-minute median of this and is converted to water level relative to N.A.P. (Amsterdam Reference Level).

Wind speed is recorded at about 1 Hz and converted to Beaufort scale.

By definition of the Beaufort scale, this means that a 10-minute running mean is taken of the recorded values. Together with the measured wind direction, wind data is stored in one-minute resolution.

4.4 Filtering and running-mean averaging

Waves appear over a large range of scales and many of them are captured with a sampling frequency of 1 Hz. By selective filtering, only those frequency ranges of interest remain in the analysis.

To remove high frequencies in the measurements, a digital fourth-order low-pass Butterworth filter is applied to data. A Butterworth filter is known for its flat response in the pass-band when compared to other filters (Bodén *et al.*, 2009). A higher order filter increases the suppression of higher frequencies faster, but the large range of coefficients due to the (very) low cut-off frequency make this impossible. Already for a fifth-order Butterworth filter the ratio of the largest (A_1) to the smallest coefficient is $1.0 \cdot 10^{-14}$, close to machine-precision. This will finally result in singularities when the filter is applied in the frequency domain. Typical cut-off periods vary from 3600 to 300 seconds (1 hour to 5 minutes respectively) and the low-, band- and high-pass filters are applied in Chapter 5 (Results) when the distinction between tidal, super-tidal and short (wind) waves is desired.

In Chapter 5 the method of running-mean averaging is also used to distinguish oscillations from slower evolving trends, similar to conversion to Beaufort scale of wind measurements. This method is applied directly in the time domain and its principle is very simple. Short-period variations are removed from the measurement by replacing an observed value by the mean of a surrounding window (a range of measurements in the time series). Such window 'runs' down the time series, and its length determines the strength of this crude low-pass filter.

Specific settings concerning the power density spectra (window length, percentage of window overlap, number of FFT-points, etc.) are stated below the graphs that present the processed data.

Chapter 5

Results

In tidal areas, frequency analysis is one of the major tools to explain observed flow fields. Least squares harmonic analysis (LSHA), Fourier analysis and rotary spectra are traditional tools for this (Emery and Thomson, 2001). In the search for any high-frequency oscillations, all three are applied to the collected data from the Mok Bay. The LSHA is used twice, to describe the presence of expected tidal frequencies but also to distinguish the frequency content at high- and low-water instants. A model is found that describes the measured high-frequency oscillations and different forcing mechanisms are suggested. Especially the properties that could be the driving mechanism for self-oscillations in the Mok Bay are investigated (Chapter 6).

5.1 Traditional Linear Analysis

5.1.1 Harmonic Analysis

In 1873 Sir William Thomson was able to construct a tidal predicting curve by means of ten main constituents. Constituent coefficients were determined from site-specific tidal records. Together with George Darwin this resulted in the systematic set of frequencies according to the Doodson number, not further discussed here. Later predictions were done using tidal machines: water levels for high- and low water were indicated mechanically. From 1966 on tidal predictions are done using computers (Cartwright, 1999).

Standard Fourier analysis determines amplitudes for integer multiples of the base frequency f_1. Since the highest possible analyzable frequency is the Nyquist frequency f_N, the frequencies f_1, $2f_1$, $3f_1$, ..., f_N are all analyzed (Emery and Thomson, 2001).

Harmonic analysis was originally designed to investigate the tidal variability, where the largest astronomical constituents are semi-diurnal and diurnal, then followed by fortnightly, monthly, semi-annual and annual variability. Since these constituents can differ greatly in period, equal spacing

of all periods in between would result in too many constituents not present in the forcing.

A more efficient method to determine corresponding amplitudes to these forcing frequencies, is thus to only analyze the (most important ones of the) frequencies which are known to be present in the forcing. For all constituents the corresponding amplitude and phase are calculated, yielding a simple prediction function. Since the number of measurements outnumbers the amount of present frequencies, the system is overdetermined. It can still be solved however, using the method of least squares: minimizing the approximation error yields the most accurate coefficients. Such a solving method allows for gaps in the time series, not allowed by Fourier analysis.

The discrete time series of a measurement $x(t_n)$, n=1, ..., N can be split into

$$x(t_n) = \overline{x} + x'(t_n) = \overline{x} + \hat{x}(t_n) + x_r(t_n) \tag{5.1}$$

where x is the measured value, $\overline{x}$ is the record mean and x' is a fluctuation. This fluctuation can in turn be replaced by a least squares harmonic analysis (LSHA) approximation $\hat{x}$ and a residual x_r. To avoid inaccuracies due to round-off errors, the mean value $\overline{x}$ of the record is subtracted, resulting in

$$x'(t_n) = \hat{x}(t_n) + x_r(t_n) = C + \sum_{q=1}^{M} C_q cos(2\pi f_q t_n - \phi_q) + x_r(t_n). \tag{5.2}$$

The approximation of the LSHA is done by determining the coefficients C_q and ϕ_q for all constituents f_q; the corresponding derivation of this method can be found in Appendix C.

Limitations on constituents

Any set of measurements is bounded by its length, temporal resolution and noise contamination (Emery and Thomson, 2001). These properties thus determine the amount of information that can be drawn from the set of measurements, i.e. they put bounds on the resolvability. In order to be able to extract useful information from a data set, a few criteria should be met.

First, the largest period (i.e. the lowest frequency) that can be resolved is equal to, or smaller than the length of the measured time series itself, T. This frequency is known as the *fundamental* frequency, and its period T_f is expressed as

$$T_f \leq T = N\Delta t, \quad f_f = \frac{1}{T} \tag{5.3}$$

where N is the length of the time series vector.

The second criterion is also known as the Nyquist criterion, limiting the highest resolvable frequency. Roughly said, it states that any sinusoidal

period should be 'caught' twice in order to resolve it. This means that the highest resolvable frequency is equal to half of the sampling frequency, being

$$f_{max} = \frac{f_s}{2} = \frac{1}{2\Delta t}, \quad T_{f,max} = 2\Delta t \tag{5.4}$$

where $T_{f,max}$ is the corresponding period. The third criterion that should be met is a bound on the maximum resolvable *frequency resolution*. This Rayleigh criterion states that two different frequencies can only be distinguished well if within the complete measured time T both frequencies are separated by at least one complete period, or,

$$|T_{f_i} - T_{f_{i+1}}| = T = \frac{R}{\Delta f}. \tag{5.5}$$

In Rayleigh's theorem $R = 1$, but if a measurement series is contaminated with noise R can be assigned a value larger than unity. This tightens the criterion and requires more than one complete period separation to distinguish frequencies properly.

Percentage of explained variance

From equation (5.1) one can define

$$SSE = \sum_{i=1}^{N} \left[(x_i - \overline{x}_i) - (\hat{x}_i)\right]^2 = \sum \left[(x_i') - (\hat{x}_i)\right]^2, \tag{5.6}$$

with SSE being the sum of squared errors. Equivalently, the measured (or, 'total') and fitted variances are respectively

$$SST = \sum_{i=1}^{N} {x'}_i^2, \quad SSF = \sum_{i=1}^{N} {\hat{x}_i}^2. \tag{5.7}$$

Combining this, one can rewrite (5.6) to

$$SSE = SST + SSF + \varepsilon$$

where

$$\varepsilon = -2\sum_{i=1}^{N} x_i'\hat{x}_i. \tag{5.8}$$

This residual, ε, will be used to find *one* number being a measure for the goodness of fit by the harmonic analysis.

$$\begin{aligned} -2\sum_{i=1}^{N} x_i'\hat{x}_i &= -2\sum_{i=1}^{N} x_i'\hat{x}_i - 2\sum_{i=1}^{N} \hat{x}_i^2 + 2\sum_{i=1}^{N} \hat{x}_i^2 \\ &= -2\sum_{i=1}^{N} \hat{x}_i^2 - 2\sum_{i=1}^{N} \hat{x}_i\left(\hat{x}_i - x_i'\right) \\ &= -2SSF + \epsilon. \end{aligned}$$

A second residual, ϵ, is obtained in this and is expressed as (using (5.1))

$$\begin{aligned}\epsilon &= 2\sum_{i=1}^{N} \hat{x}_i \left(\hat{x}_i - x_i'\right) \\ &= 2\sum_{i=1}^{N} \hat{x}_i x_{r,i}.\end{aligned}$$

The subscript r, i indicates the ith element of the residual between approximated fit and measured water level. Again, rewriting (5.6), one finds

$$SSE = SST + SSF + \epsilon. \tag{5.9}$$

The purpose of the above's derivation is to obtain a practical measure for the quality of the approximation by the fit. Numerically performed approximations yielded values of $\epsilon/SSE = 1 \cdot 10^{-13}$, indicating that the derived residuals actually can be neglected.

A measure for the goodness of fit by the least squares harmonic analysis can be expressed in terms of the fit SSF and the measured water level SST by

$$\sigma^2 = \frac{SSF}{SST} \cdot 100\%. \tag{5.10}$$

Application to data

Among the 22 largest constituents are the fundamental solar and lunar constituents, S_2 and M_2 respectively (Buijsman and Ridderinkhof, 2007). Others concern higher harmonics (or combinations) of these. According to the Rayleigh criterion (5.5), one needs at least 14.4 days of time data in order to resolve both S_2 and M_2. With 6 weeks of data already 22 constituents can be solved, and the resulting model gives a fairly good representation of the original signal, as can be seen in Figure 5.1. For modeling of the water level, Buijsman and Ridderinkhof (2007) found a goodness of fit of 81% for a 5-year ADCP data set, here 88.9% is found. Buijsman attributes such differences to the fact that wind set-up in the North Sea can make the water level locally differ by ± 0.5 meter. Such behavior cannot be explained by the tides, and thus decreases the goodness of fit, especially in this short-period time series.

Although the data is detrended before the LSHA is applied, at low frequencies still large amplitudes are found in the fit. Compared to Buijsman and Ridderinkhof (2007) the relative amplitudes of M_m and M_{sf} are very large. In their harmonic fit for the nearby Marsdiep water level, these amplitudes were 1.6 and 1.8% of M_2 respectively. As mentioned above, wind set-up can have a relevant influence on the water level. Measurements of

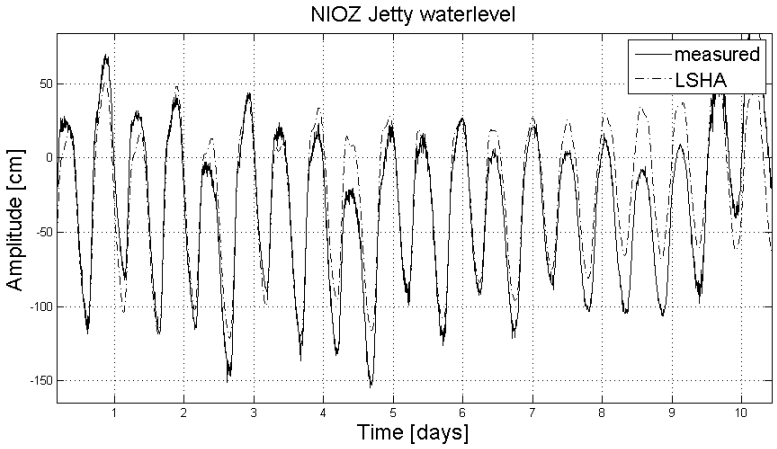

Figure 5.1: Least Squares Harmonic Analysis (LSHA)-fit to a 6-week time series of NIOZ Jetty water level measurements. Time series reconstruction using the best fit obtained with the Least Squares Harmonic Analysis (LSHA) from a 3-week NIOZ Jetty water level time series.

wind speed and direction performed at the same NIOZ Jetty indicate this, see Fig. 5.3. After 7 days of Easterly wind, 7 days of North Westerly wind is measured, again followed by Easterly winds. Such '14-day-period' of wind is not due to the astronomical forcing, but *is* approximated by the two closest frequencies present in the harmonic analysis: M_m and M_{sf} with 27.56- and 14.77-day periods respectively.

Finally, the ratio $(K_1+O_1)/(M_2+S_2)$ indicates if the site of measurement has a semi-diurnal (< 0.25), mixed (> 0.25 & < 1.25) or diurnal (> 1.25) tide. Using the data from the LSHA as presented in table 5.1, it follows easily that at the NIOZ Jetty the tide is mainly semi-diurnal (0.228). This agrees with the value of 0.20 from the multiple-year measurements in the Marsdiep inlet (Buijsman and Ridderinkhof, 2007).

5.1.2 Fourier Analysis

Fourier analysis can be applied if one wants to analyze more frequencies than just those which are expected to be present in the forcing. As described above, all integer multiples of the base frequency (up to the Nyquist frequency) are analyzed.

The largest downside of the Fourier analysis is however the fact that amplitudes are averaged over the complete analyzed period. This implicitly means that only stationary signals can be represented well. Another disadvantage is the fact that the discrete time series must be equally spaced. Finally, all time-information is lost when transforming from time domain to frequency domain. Since one already should be working with a stationary signal, this is no problem.

In this thesis it is however the aim to investigate the dynamics of an estu-

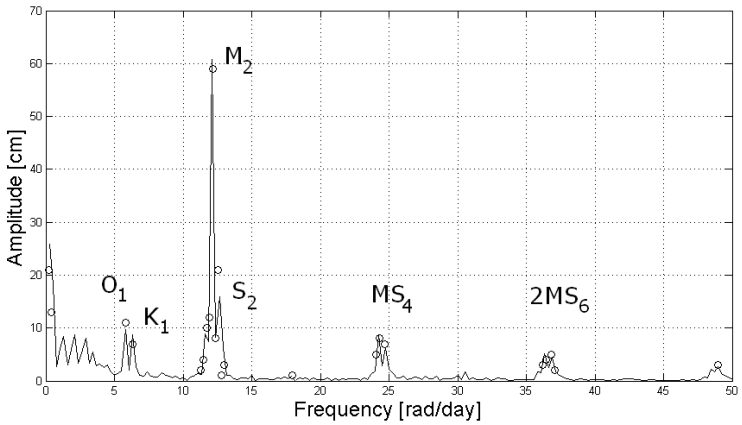

Figure 5.2: Frequency analysis of the NIOZ Jetty water level measurements LSHA-fit using Fourier analysis (black line) and LSHA (∘) of a 3-week time series. Results coincide well, showing the effectiveness of the harmonic analysis.

ary, which might evolve in time. The theoretical background suggested the possible presence of multiple equilibriums (single frequency forcing, (Maas, 1997)) and/or chaotic behavior (two-frequency forcing, (Maas and Doelman, 2001)), which is a non-stationary behavior.

Application to data

As can be seen in figure 5.2, the frequency components (constituents) that are used in the harmonic analysis are found with similar amplitudes by the Fourier analysis. The low-frequency content ($0.5 < f < 4$ rad/day) differs, but has been explained by weather influences. Both methods come to the same results, showing the effectiveness of the harmonic analysis. On the other hand, both methods also require a stationary signal, whereas the oscillations might occur at separate occasions.

5.1.3 Rotary component spectra

For a better analysis of the frequency spectra of the local velocity components, a local coordinate system is introduced. Using the mathematical coordinate convention for α, (taken counter clockwise from Eastward, see figure 5.4), the North-East frame will be rotated by $\alpha = 76°$ to obtain the Alongstream-Crossstream frame of reference. The following relation is used for the coordinate rotation:

$$v_{al} = v_N \cos\alpha - v_E \sin\alpha$$
$$v_{cr} = v_N \sin\alpha + v_E \cos\alpha,$$

Constituent	f $[rad/d]$	f $[cpd]$	A $[m]$	$\%M_2$	Φ $[°]$
A_0			0.03	5.25	
M_2	12.141	1.9323	0.59	100.0	-128.2
S_2	12.566	1.9999	0.21	35.9	-109.2
N_2	11.913	1.8960	0.12	20.9	36.2
μ_2	11.715	1.8645	0.10	17.1	5.70
L_2	12.369	1.9686	0.08	14.2	-135.0
M_6	36.422	5.7967	0.04	6.66	100.2
$2MS_6$	36.848	5.8645	0.05	9.36	96.9
M_4	24.282	3.8646	0.08	13.31	-63.9
O_1	5.8404	0.9295	0.11	18.44	-63.5
K_1	6.3004	1.0027	0.07	12.65	-4.4
$2MN_6$	36.194	5.7605	0.03	5.35	-108.5
MS_4	24.707	3.9322	0.07	11.99	-43.1
MN_4	24.054	3.8283	0.05	8.50	110.0
$3MS_2$	11.290	1.7969	0.02	2.99	172.6
$2SM_2$	12.992	2.0677	0.03	5.10	49.6
ϵ_2	11.487	1.8282	0.04	6.68	166.0
MSL_6	37.076	5.9008	0.02	3.39	75.5
$3MS_8$	48.989	7.7968	0.03	4.85	-166.6
$2MK_3$	17.981	2.8618	0.01	0.93	91.3
ζ	12.794	2.0362	0.01	2.09	-151.3
Mm	0.2280	0.0363	0.21	36.05	154.9
Msf	0.4255	0.0677	0.13	23.55	-29.0

Table 5.1: Frequency (f, in rad/day and cycles per day (cpd)), amplitudes (A) and phases (Φ) (relative to the start of measurement, 2010-02-25 14:00) of water level tidal constituents fitted to the NIOZ Jetty measurements for the period of January 19th to March 8th 2010. The 22 largest constituents are listed, together with the fitting constant A_0. Goodness of fit 88.9%, $\sigma = 18.52$ $[cm]$.

where v_N and v_E are the North- and Eastward components of the measured velocity, the subscripts al and cr indicate the alongstream and crossstream components respectively. Using this, one can construct a complex velocity w,

$$w = v_{cr} + iv_{al} \tag{5.11}$$

The Fourier spectra of the two transformed velocity components show –like the harmonic analysis– a large amplitude for the M_2 constituent, see figure 5.5. Such distinct spikes are present in the spectrum for *both* the along- and crossstream direction, indicating that the local flow is more complex than rectilinear motion (purely alongstream flow) in the entrance of the ship road.

The spectra of the two amplitudes and phases of the along- and crossstream

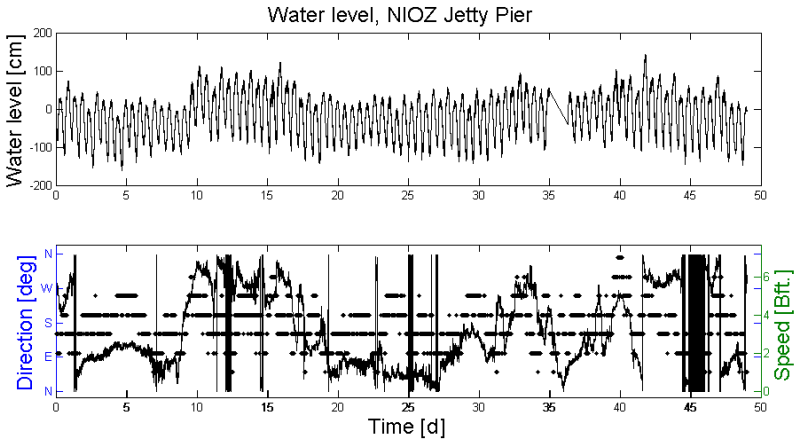

Figure 5.3: 49-day period of water level measurements (upper) at the NIOZ Jetty, relative to N.A.P. Wind speed and direction measurements (lower) performed at NIOZ Jetty over the same period. Note the set-up of water at lasting (North) Westerly winds, and the lower water level at Easterly winds.

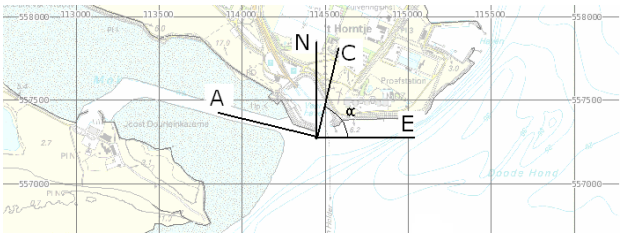

Figure 5.4: Coordinate systems at the MK-2 location. Magnetic North (N) and corresponding Eastward direction (E), rotated to alongstream (A) and crossstream (C) by an angle $\alpha = 76°$ CCW from East. The alongstream direction corresponds to the orientation of the local ship road in the Mok Bay. *Source: Ministry of Public Works and Water Management (Rijkswaterstaat).*

flow can be used to construct velocity *ellipses*. Two circles (a clockwise, CW, and a counter clockwise component, CCW) together describe an ellipse, being the 'particle path' at that location. Per depth bin (depth range) a spectrum of such ellipses can be calculated, describing the local flow field in a way which is easy to interpret. Here, the second bin from the ADCP transducers is used. This is motivated by the following: close to the bottom one will find lower velocities due to friction (underestimating the flow). On the other hand, close to the surface the motion is influenced by waves. During the period of measurements strong winds were present, of which the influence is reduced by not including the upper bins. During (very) low water, only 1 meter of water was present above the ADCP, increasing the need to exclude higher bins.

Using velocity ellipses, one can for example easily see if it is justified to assume that a major diurnal constituent (like M_2) is aligned with the ship

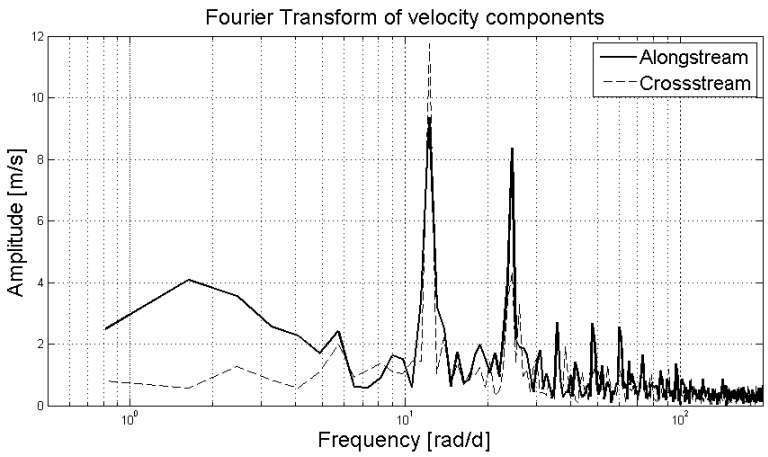

Figure 5.5: Fourier spectra of the transformed velocity components, in along- and crossstream directions relative to the ship road. M_2 constituent at 12.42 rad/day, period of measurement februari 26th to march 6th 2010, at MK-2 beacon.

road. If the clockwise (CW) and counter clockwise (CCW) components have a similar amplitude, the particle travels in a straight line: the semi-major axis of the ellipse. The orientation of this axis is dictated by the phase difference between the CW and CCW component. The complex velocity w now represents ellipses for a frequency range per location (depth); the seven largest frequencies can be found in figure 5.7.

As can be seen in figure 5.7, none of the largest ellipses is aligned with the ship road (alongstream direction). Possible reasons for deviations are an offset of the internal (magnetic) compass and/or significant local disturbance of the flow field (for example, by the bathymetry or the local coastline). The different orientations of the semi-major axes of the ellipses show again that the flow seems to be more complex than simply aligned with the ship road. Especially since the used data is obtained from the ADCP's lowest bin, i.e. the water 'layer' located the deepest inside the ship road.

The calibration procedure for the internal compass demands that the ADCP is rotated 360° relative to North twice, at about 5° per second. This calibration should have been done when the ADCP is in position (completely mounted and moored), so this is practically impossible. The influence of the steel cables, neighboring instruments and the steel MK-2 beacon on the internal compass is not directly known.

ADCP compass calibration

In the following, the standard oceanographic convention is used to indicate the direction of flow, i.e. Eastward corresponds to 90°, defined positive in clockwise direction (CW) from magnetic North (0°). In figure 5.8 the

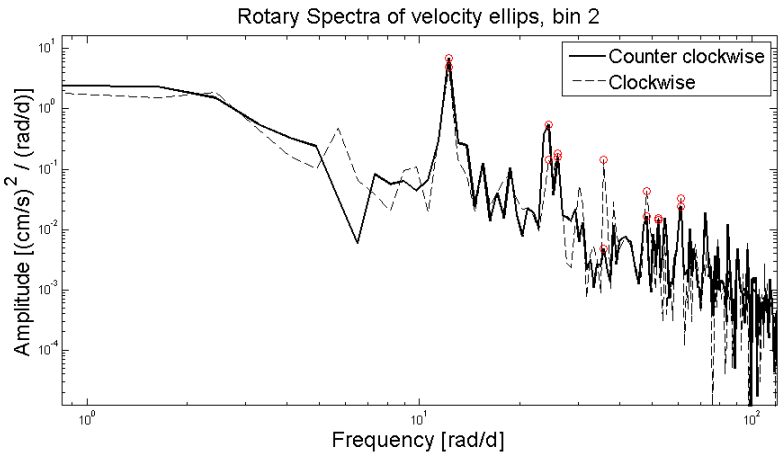

Figure 5.6: Rotary spectra of clockwise and counter clockwise components of the velocity ellipse. Seven largest separated frequencies are marked with circles for both components. Measured velocity data from februari 26th to march 6th 2010 at MK-2 beacon, second bin from ADCP transducer faces (∼70 cm from bottom).

rise of water level is accompanied by a $-20°$-flow direction according to the ADCP's internal compass. The ship road into the Mok Bay is however not aligned in this direction: the internal compass of the ADCP seems to suffer from the presence of surrounding metals. For almost the complete tidal cycle the flow direction at the moored frame is completely different as compared to the Marsdiep, but using the Marsdiep inlet as a reference and figure 5.8, most of the local flow field throughout a tidal cycle can be explained reasonably.

Measurements in the centre of the Marsdiep are available from Groeskamp (2010) for a timespan of 20 days and from this a typical velocity profile for a tidal cycle is extracted and used for reference. From these measurements the alongstream velocity magnitudes are used since they are considered to dominate over the crossstream by one order of magnitude (Groeskamp, 2010).

The main assumption in the following is that the offset of the internal ADCP compass relative to the magnetic North can be calibrated by the fact that inflow of the Mok Bay occurs in the direction of the ship road in the bay (alongstream direction). This offset is considered to be constant over time: the (magnetic) influence of the nearby ferry and the settling of the frame in the bottom are negligible, see Chapter 4. Also, the magnetic and true North are assumed to coincide.

The direction of flow at the moored frame is compared to that in the Marsdiep for one typical tidal cycle, using the above mentioned assumptions. The resulting flow field agrees with practical observations:

- A rise in water level (figure 5.8, A) just after low water (I) causes the outflow of the Marsdiep inlet to stagnate and become an accelerating

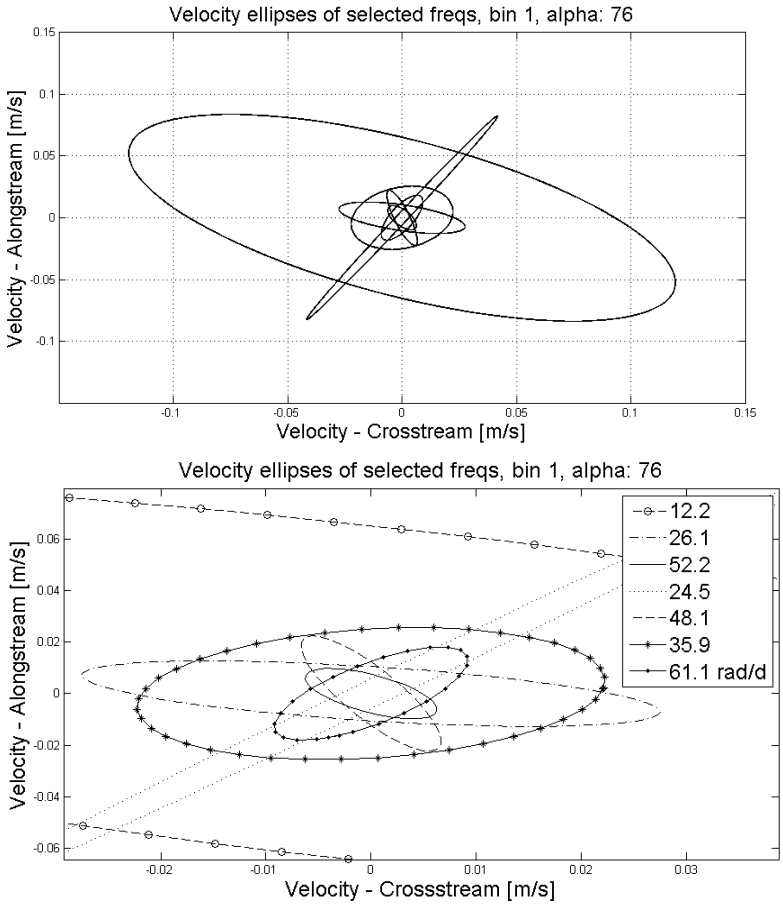

Figure 5.7: Velocity ellipses for the seven largest amplitudes present in the velocity (along- and crossstream) spectra. Measured velocity data from februari 26th to march 6th 2010 at MK-2 beacon, second bin from ADCP transducer faces (∼70 cm from bottom). The ellipse aligned with the large M_2 ellipse has a frequency of 26.1 rad/day and is not among the 144 largest constituents. This is to be investigated more, especially because its frequency is quite low for a resonance.

inflow (A). The water level in the bay can only rise if water comes in through the ship road, upper-left panel, figure 5.9;

- After first flood (II, B) the inflow of the Marsdiep is now at (constant) maximal velocity, but at the moored frame it decreases to nearly zero. Although the speed is small, the direction is consistent over this short period, upper-right panel, figure 5.9;

- In the Marsdiep inlet a period of decelerating inflow follows (C) while the water level still rises. The direction of flow at the moored frame turns away from the Mok Bay, towards the Marsdiep. This is also experienced by co-workers who daily check their fike, Southwest of the MK-2 mooring. Especially at the end of flood tide this is noticed,

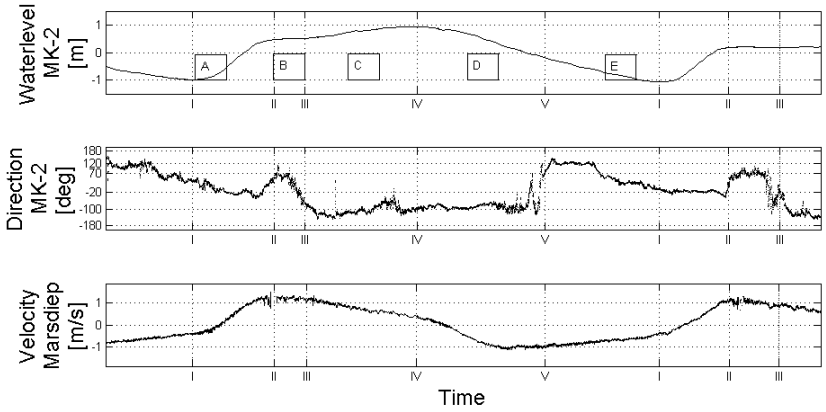

Figure 5.8: Detail of a period of waterlevel (top) and flow direction according to the ADCP internal compass (middle) at the moored frame. Reference (alongstream) velocity of a typical period of the nearby Marsdiep channel (bottom). Intervals indicate accelerating flood flow (A), constant flood flow (B), deccelerating flood flow (C), accelerating ebb flow (D) and deccelerating ebb flow (E) of the Marsdiep channel.

which agrees with the measurements during interval C (figure 5.8, after aligning the direction of inflow along the ship road). Compared to the NIOZ Jetty, there is no constant water level difference over the bay for this interval (a pressure difference that empties the bay), but again the direction is consistent. Possibly a large steady vortex is formed in this shallow bump in the coastline. At the end of this period the Marsdiep inflow has become a slight outflow, figure 5.9, bottom-left panel.

- The decreasing speed of the inflow is followed by an accelerating outflow (D), for which the direction is clear in the Marsdiep inlet. At the moored frame, this outflow is almost opposite in direction. The water mass leaving the Wadden Sea comes for a large part from the Northeast and is deflected by the sharp edge of the local coastline as indicated by the small arrow. Just after this sudden change in coastline orientation, also the local depth decreases from 26 to ∼8 meter, causing a back flow just next to the coast. The whole harbor of the ferry and also the mouth of the Mok Bay are in this wake; for the outflow of the Bay this means that it can follow the direction of the channel, and the contour of the local coastline (bottom-right panel, figure 5.9). The decreased (Southwestward) momentum in the wake allows the flow exiting the Mok Bay to maintain its bay-outward direction at least at the location of the moored frame and just in front of the entrance of the TESO harbor, as experienced by captains on the ferries;

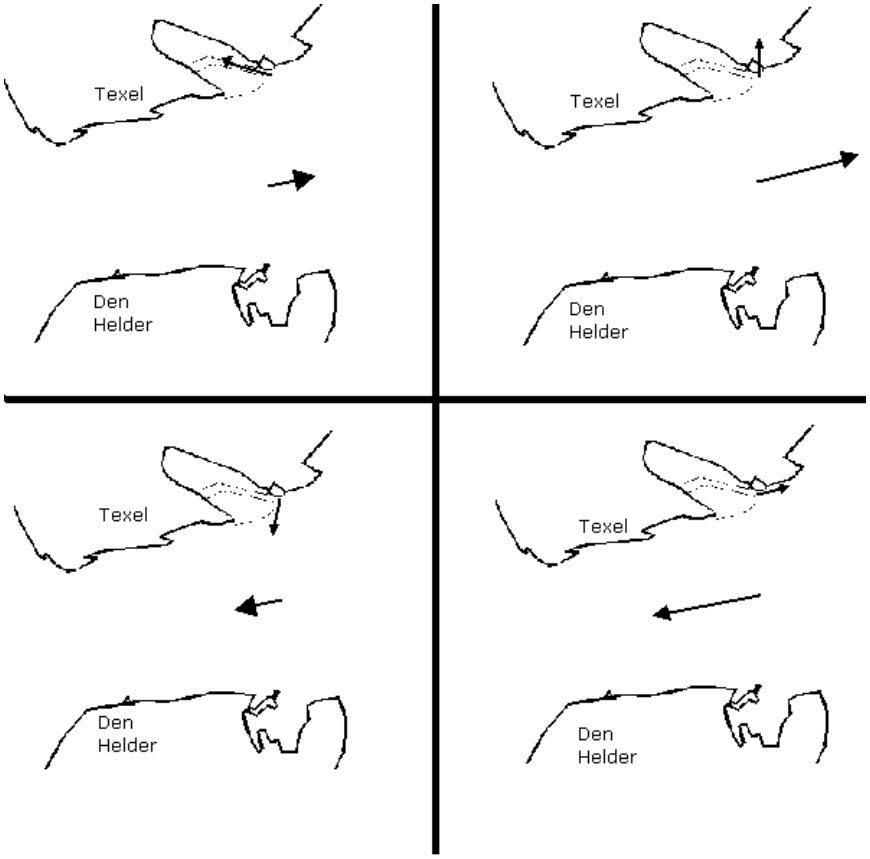

Figure 5.9: Schematic representation of the direction of flow in the Marsdiep inlet (large arrow) and at the inlet of the Mok Bay ship road (smaller arrow) during the four major stages of a tidal cycle. Accelerating inflow, just after low water (upper-left), constant maximal inflow (upper-right), decreasing inflow to slight outflow (lower-left) and accelerating outflow (lower-right).

- Finally, in a new tidal cycle the water level rises and the outflow of both the Mok Bay and the Marsdiep stagnate. The direction of flow at the mooring slowly turns back to the starting of the cycle, at $-20°$ relative to 'ADCP-North'.

A concrete offset of the ADCP internal compass can now be summarized as follows. The inflow of the bay occurs along a $-20°$ direction relative to ADCP-North, while this ship road is towards $-76°$ from true North according to maps of this area. Rotating the measured directions of flow to fit this, they now actually fit to the observations. The total influencing on the internal compass can thus be expressed as a $-56°$ offset, taking true North and magnetic North equal for now. Using this, the velocity ellipses are calculated again and shown in figure 5.11.

Knowing that the bay floods and 'empties' twice a day (the M_2 constituent has the largest amplitude), the direction of flow should for a large

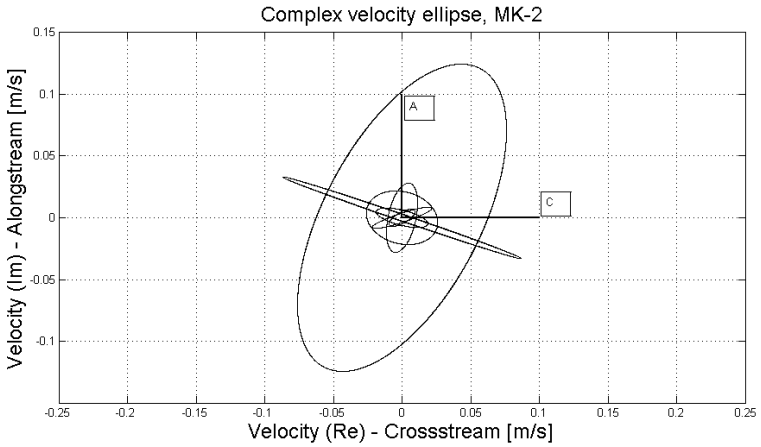

Figure 5.10: Complex velocity ellipses for the seven largest amplitudes as indicated in the rotary spectra of figure 5.6. Used frame of reference: along- and crossstream directions, $\sim$ 70 cm from bottom (second bin from ADCP transducer faces).

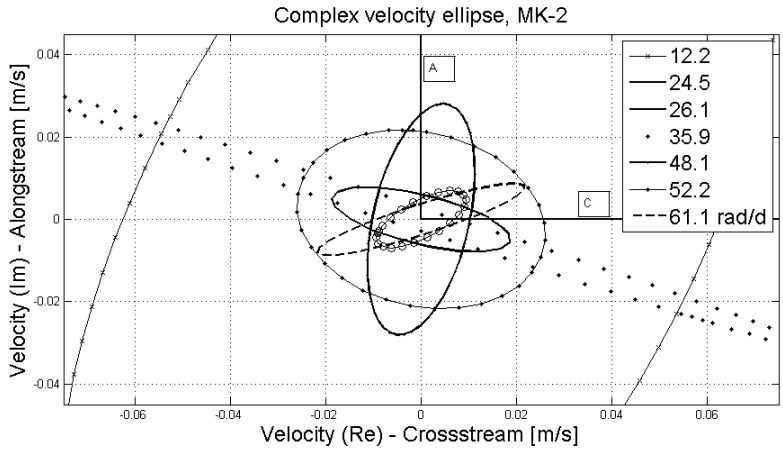

Figure 5.11: Detail of the complex velocity ellipses for the seven largest amplitudes as indicated in the rotary spectra of figure 5.6. The frequencies of 12.2, 24.5 and 35.9 approximate the tidal constituents of M_2, M_4 and M_6 respectively.

part be described by the M_2-ellipse. In figure 5.12 two instants of the tidal cycle are marked, flood- and ebb flow respectively. The rise in water level during flood flow means an inflow into the bay ($\circ$), in the alongstream (A) direction. During ebb flow, the bay empties and the 'jet' out of the bay follows the local coastline ($\otimes$). The calibration of the internal compass of the ADCP is summarized as a 56° offset from magnetic north, and is now possible to explain the measured and observed directions of flow during a tidal cycle.

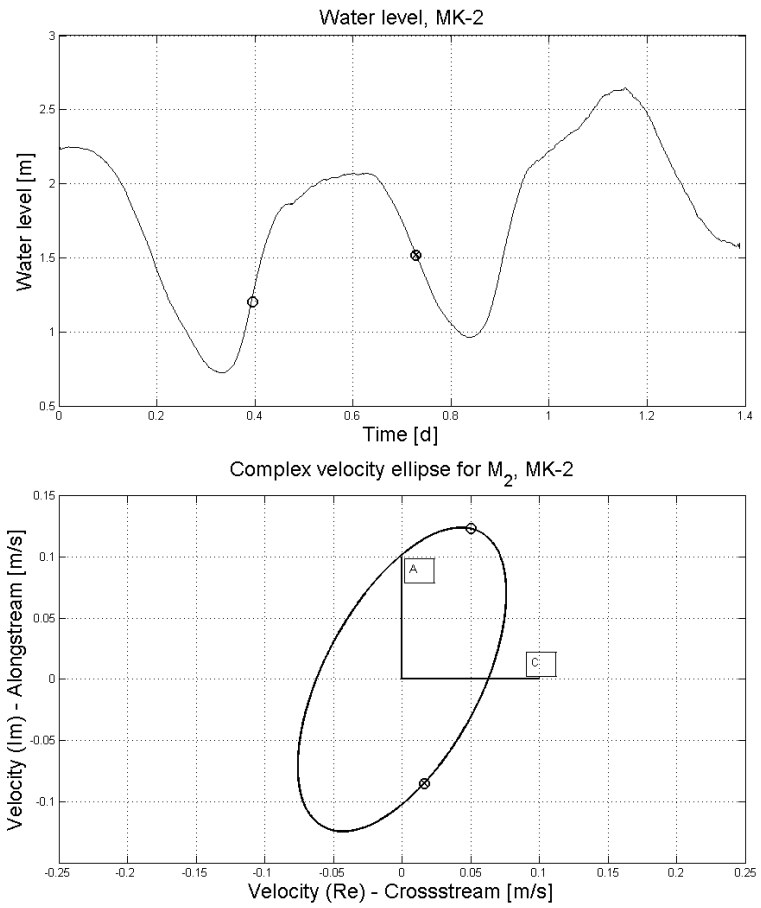

Figure 5.12: Local water level (upper) and complex velocity ellipse (lower) as obtained from the rotary spectra. Inflow (○) agrees reasonably with the alongstream direction (A), outflow (⊗) to a direction close to E, as indicated in figure 5.9.

5.2 Oscillations in the Mok Bay

Indications of oscillations

Similar as described in Golmen *et al.* (1994), measurements of the water level at both the head and mouth of the bay reveal super-tidal water level oscillations, albeit with smaller amplitude at the mouth. In the case of a Helmholtz resonator, the strait that connects the basin to the sea does not elevate as much as the basin itself does, but here the oscillations can be visible as an oscillating *flow*.

The water level as measured in the Mok Harbor seems to oscillate around the level as measured at the MK-2 beacon, see figure 5.13. If a running-mean (33-minute window) is subtracted from the water level measurements, the water level *residual* is obtained. This allows for an easier analysis of the oscillation around the tidal elevation. Since the amplitude of surface

oscillations is small ($\approx 1cm$) compared to the tidal elevations, it is magnified by a factor 10 in figure 5.13.

As can be seen in figure 5.2, there is a clear relation between the oscillations in water level as measured in the Mok Harbor and the measured current at the MK-2 mooring. This figure also gives an indication of the significance of the oscillating flow: it is with its $\mathcal{O}(0.1ms^{-1})$ of the order of magnitude of the tidal current! The small water level elevations ($\mathcal{O}(0.01m)$) needed to transport the oscillating volume through the narrow entrance in a relatively short time, being the cause for this. Figure 5.15 shows the calculated coherence between the oscillations in water level and flow velocity (alongstream). Clearly present is the high coherence at the frequencies of 31 and 48 cycles per day. As will be shown later, these are the Helmholtz frequencies of the bay for flood and ebb respectively.

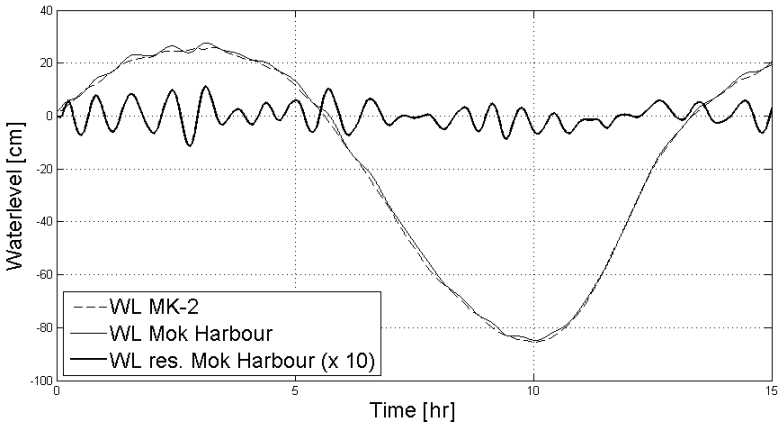

Figure 5.13: 15-Hour detail of water level (WL) observations, as measured at both the Mok Bay's mouth (moored frame at MK-2 beacon, broken line) and head (Mok Harbor, solid line). Subtracting the running mean yields the water level *residual*, indicated as *WL res.* (bold, solid line, magnified by factor 10).

For the three sites of water level measurements, a power spectral density is calculated. Using this, a spatial variation of any oscillations can be found; the PSD spectra of the three locations can be found in figure 5.16. Clearly less energy is present outside the Mok Bay for the frequencies of resonance (27.6 and 31.1 cpd). Outward radiated waves still contribute to the energy (water level) as measured at the NIOZ Jetty, but most of the oscillation's energy is shown to be concentrated within the bay.

Even more specific information can be obtained by splitting the period of measurements into an ebb and a flood part. The low water (LW) 'half' is defined as the moments at which the water level is below average, and defined as high water (HW) when it is above average. The measured water level consists not of purely sinusoids, so a linear spectrum is not the proper way to visualize results on ground of energy conservation (Bodén *et al.*, 2009).

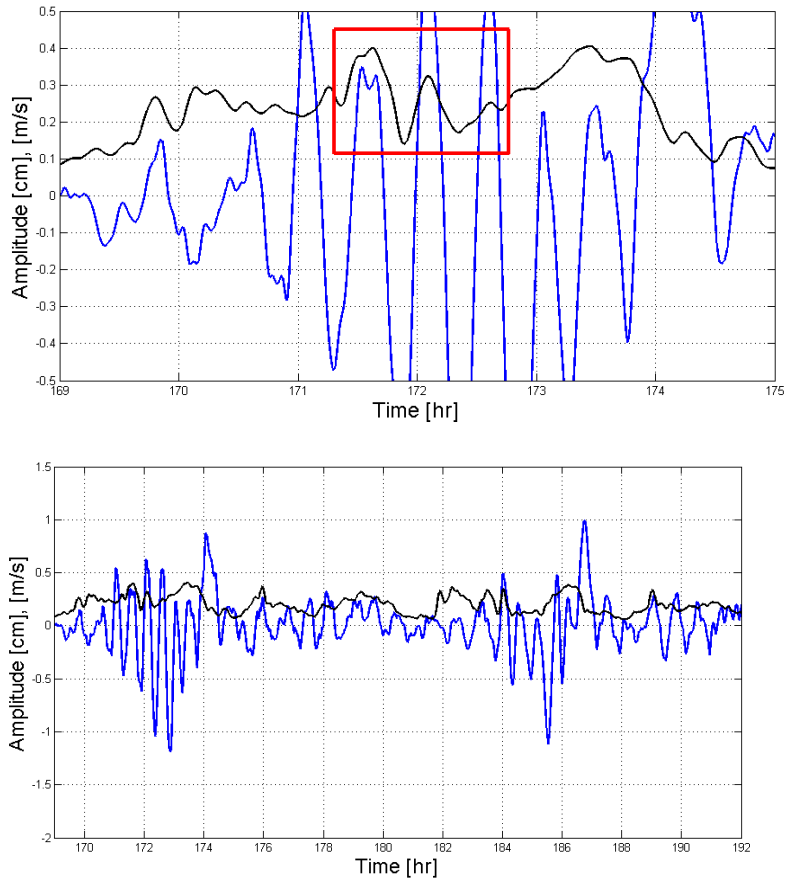

Figure 5.14: 23-Hour time window of flow velocity magnitude (black) and water level residual (blue, bottom) and detail (top). Water level residual obtained by subtracting a 20-minute running mean (tidal curve) from the low-passed water level measurements (Mok Harbor, cut-off period: 5 minutes). Flow velocity magnitude is low-pass filtered with a cut-off period of 10 minutes. At t=172 (t=176, 184, 189) hours the order of magnitude for water level oscillations ($\mathcal{O}(1cm)$, bottom frame) and magnitude of flow oscillations ($\mathcal{O}(0.1ms^{-1}$, top frame) is visible.

But only the earlier introduced harmonic analysis allows gaps in input time series, so a linear spectrum is used to show an important distinction between ebb and flood moments.

The least squares harmonic analysis (LSHA) is performed over the selected intervals that are flagged as 'ebb' or 'flood', and the resulting (band-passed) frequency content is shown in figure 5.17. Again, amplitudes should be interpreted *relative* to each other. Two things are visible here: during ebb moments resonances occur with ~ 48 cycles per day (~ 31 during flood) and during ebb tides the water level residual has larger amplitudes (for all $f < 85$ cpd) as compared to flood instants. The flooded tidal bank at high water allows water to enter and leave the bay without flowing strictly

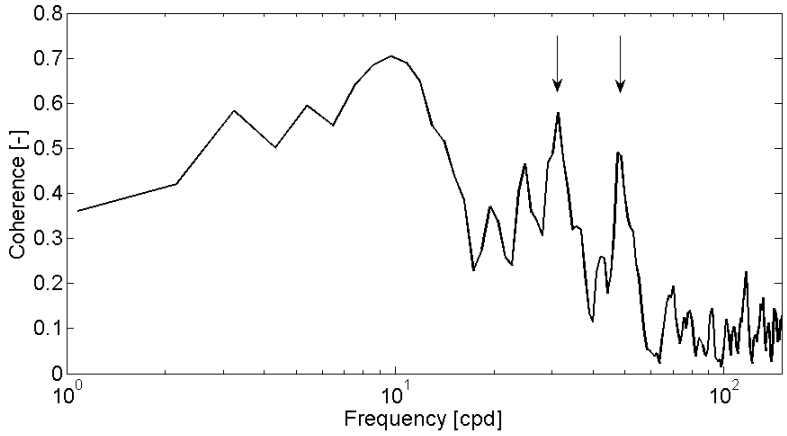

Figure 5.15: Coherence between low-pass filtered current measurement (MK-2 beacon) and water level measurements (Mok Harbor) of the 7.7-day period the ADCP was in use. High coherence at 31 and 48 cycles per day (cpd) is clearly present, as indicated by the arrows. Low-frequency content (<15 cpd) is due to tidal motion. Cut-off frequency for low-pass filter: 288 cpd (T = 5 min.). Settings for coherence calculation: $5 \cdot 10^4$-point Hanning window, 60% overlap, $5 \cdot 10^4$ FFT-points.

through the ship road, which might explain the lower amplitudes for this spectrum.

No clear peaks of the oscillations are found in the power spectral density of the alongstream velocity. Although the oscillations are found in the water level throughout the measurements (see figure 5.2 and 5.13), they do not necessarily have a similar (or, constant) phase lag relative to the tide. Moreover, if separate events of oscillations have opposite phase, they cancel each other in the calculation of the (complex) power spectral density. Averaging of amplitudes rather than complex vectors can in turn give insight on the existence of these peaks in separate PSD-windows.

5.2.1 Attributing resonance

The time for the ferry to leave and enter back into the TESO harbor (Texel) is approximately 44 minutes, repeating every hour during day (0600-2100 hour). This period is quite close to the observed period of water level oscillations. To make sure the 'measured' waves are not smoothed-out peaks in the data set, raw data from the Mok Harbor depth meter is compared to the ADCP internal compass. It is known that this compass has an offset relative to North, but now only the deviations due to the ferry's hull at every passing are relevant. Figure 5.19 shows that oscillations in the Mok Harbor are visible in the raw data also at times for which the ferry stopped sailing 3 hours earlier. So a simple check shows that the observed oscillations are not due to passage of the ferry (directly) or to data analysis.

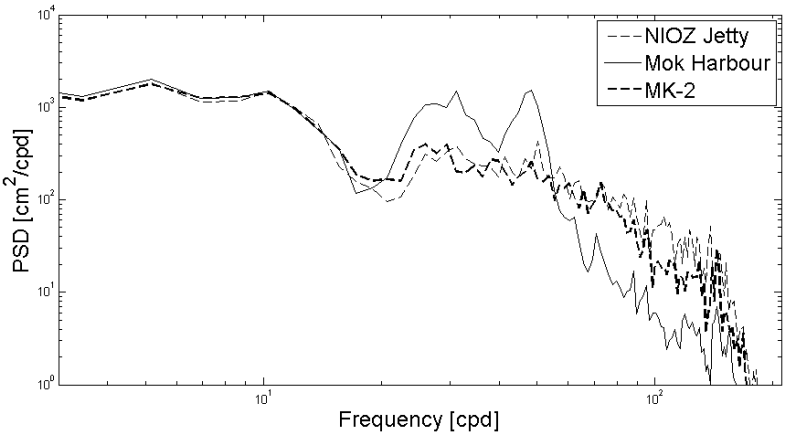

Figure 5.16: Power Spectral Density spectra for water level measurements at the NIOZ Jetty (broken line), Mok Harbor (solid) and MK-2 beacon (bold, broken line). Common low-frequency energy due to tidal movement, less energy in Mok Harbor for frequencies above 60 cpd by it's sheltered location. Resonance peaks at 31.1 and 48.4 cpd used to determine Q-factor of the Mok Bay.

The observed frequency of 30 cycles per day corresponds to a period of 48 minutes, close to the oscillations observed in the Norwegian Moldefjord by Golmen *et al.* (1994). Following their analysis and Rabinovich (2009), several models are tested to describe the oscillations.

Merian's formula for natural periods in a rectangular basin of uniform depth with an open entrance is

$$T_n = \frac{4L}{(2n+1)\sqrt{gH}}, \quad n = 0, 1, 2, 3, \ldots, \tag{5.12}$$

as described in Rabinovich (2009). Here $\sqrt{gH}$ is the shallow-water wave speed and L the basin's length. The lowest mode ($n = 0$) corresponds to a period of $T_0 = 12.8min$ ($L = 1200m, H = 4m$), and is too short to explain the observed period. Including a part of the Wadden Sea in L (similar to including the Sildegapet at the Moldefjord) is not justified since oscillations are shown to be localized to the Mok Bay. Higher modes have even shorter periods ($T_1 = 4.3min$), so this is not the suitable model.

For the lowest (or fundamental, $n = 0$) mode Wilson changed Merian's model to

$$T_0 = a\frac{2L}{\sqrt{gH}} \tag{5.13}$$

where a is a shape-factor (Rabinovich, 2009). For a semi-elliptic basin shape (and semi-circular shape as well) $a = 2.22$ and the fundamental frequency for the Mok Bay should be $T_0 = 14.2$ minutes. Wilson assumed a semi-paraboloidal depth profile, which is more applicable in a fjord than the

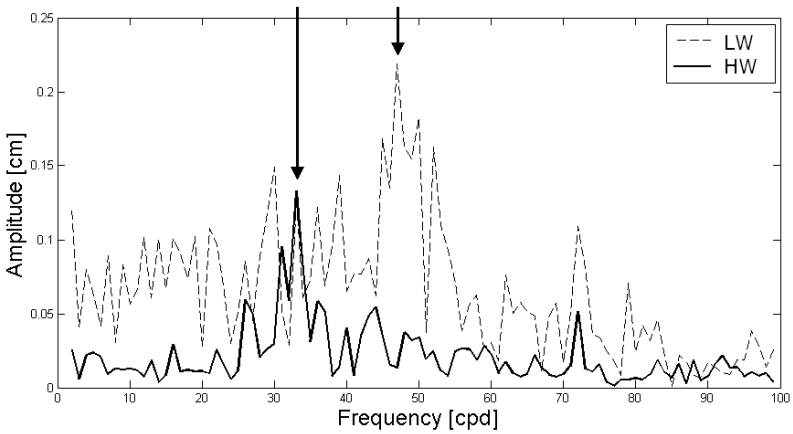

Figure 5.17: Frequency content of the least squares harmonic fit to the waterlevel residuals h at ebb ($h < \bar{h}$) and flood ($h > \bar{h}$) periods between februari 26th and march 6th 2010. Frequency of resonance at ebb tide $f^{ebb} \approx 48$ cpd ($T \approx 29$ minutes), $f^{flood} \approx 32$ cpd ($T \approx 45$ minutes) for flood tide. The common peak at $f \approx 72$ cpd (20 minute-period) is approximately the frequency of the ferry leaving and entering the TESO harbor.

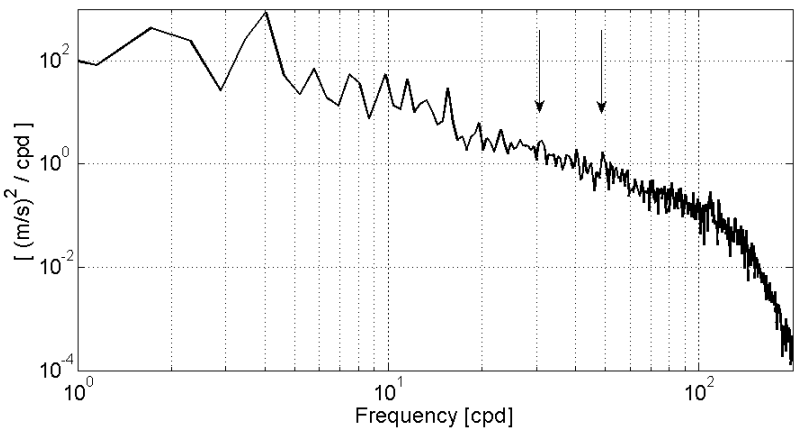

Figure 5.18: Power Spectral Density spectrum of the 7-day low-pass filtered alongstream velocity, as measured at the MK-2 beacon. Most energy present at tidal frequencies (2, 4, ... cycles per day), hardly visible is the energy present at the Helmholtz frequencies (31 and 48 cpd). Settings for power estimation using Welch's method: 56-Hour (Hamming) window, 75% overlap, $15 \cdot 10^4$ FFT-points.

shallow Mok Bay. Again, this is too short as compared with the observed 48-minute period. Moreover, the increased water depth (H) at high water decreases the period of oscillation (in both Wilson and Merian's model), opposite to the observations.

As with all resonators, the eigen frequency depends on the dimensions of the resonator. For the Mok Bay, the dimensions differ much between ebb

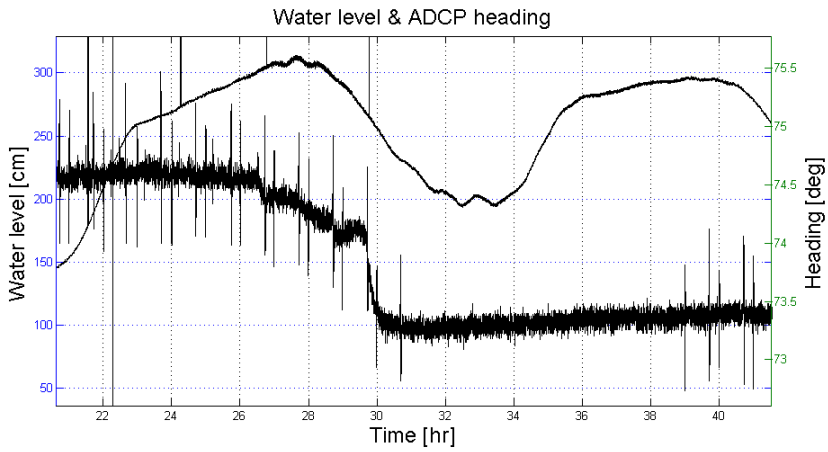

Figure 5.19: 40-Hour detail of raw depth meter (water level) data as measured at the Mok Harbor (left axis) and heading of the ADCP internal compass (right axis). The steel hull of the ferry causes spikes in the heading (magnetic compass) data, and shows no coherence with the observed oscillations in the water level of the Mok Bay. Step in heading-data at $t \approx 30$ hour due to settling of the heavy frame or settling of the ADCP within the frame. Time is relative to start-up of the ADCP.

and flood tide, so the Helmholtz frequency might as well. Equation 2.17 describes the Helmholtz frequency as a function of two dimensional length scales. Using this, the period T_H for a Helmholtz resonator can be estimated as:

$$T_H = 2\pi\sqrt{\left(\frac{A_0 L}{gHB}\right)}, \tag{5.14}$$

In Golmen *et al.* (1994) a Helmholtz resonator is ruled out as the driving mechanism for the oscillations, since the period $T_H = 50$ minutes demands an effective strait length being four times the real entrance length. An effective length includes mass outside the strait that oscillates too (outward radiated waves), and so increases the real channel length to an 'effective length' (Maas, 1997).

For the Mok Bay however, the Helmholtz model describes the measured frequencies of oscillation quite well. Table 3.3 lists the estimated dimensions and the resulting theoretical eigen frequencies are shown in table 5.2.

The difference in water surface area between high and low water is large, just as the length of the channel that connects the 'bay' (that part described by A_0) to the Wadden Sea. Their product, $A_0 L$ decreases by a factor 5.01 from flood to ebb, but also H decreases (factor 1.57). This all changes within the square root, resulting in a decrease of the Helmholtz frequency by only a factor of 0.56. This comes close to the observed ratio of 0.64 between 31 and 48 cycles per day for flood and ebb respectively.

Helmholtz Frequency	*Ebb*	*Flood*	unit
$[gHB/A_0L]^{1/2}$	53 ± 3	34 ± 3	*cpd*
Measured	48	31	*cpd*

Table 5.2: Theoretical Helmholtz frequency for both ebb and flood state of the Mok Bay, estimated using the dimensions as listed in table 3.3. Theoretical frequencies match well with the observed frequencies of oscillation, assuming the complete channel oscillates during ebb tide.

5.2.2 Mechanisms for generation of resonance

Oscillations in enclosed waters (lakes) are usually caused by direct external forcing on the surface, for example by atmospheric pressure changes or wind. The semi-enclosed Mok Bay can be forced by many possible mechanisms, for which the probability will be discussed here. If the oscillations match the basin's eigen frequencie(s), the basin's seiche (eigen frequency) is said to be resonantly forced. Opposite to this, oscillations are non-resonantly forced when driven at a different frequency (Rabinovich, 2009).

As with lakes, atmospheric pressure differences can cause long waves in the ocean. Due to nonlinearities they span a wide range of frequencies when they finally reach the basin. This holds as well for the interaction of wind waves and swell (set-up of water at coasts), although the latter are in general of higher frequency. Tsunami waves occur when an earthquake suddenly moves water masses. For increasing distance from the earthquake, the 'ringing' in the ocean increases, and energy concentrates in the local (basin's) resonance frequencies. Meteorological tsunamis exist as well, though be it with smaller amplitudes. Sudden changes in atmospheric pressure create a sea level difference, which is amplified if the pressure front travels with the wave speed. Internal ocean waves can have large amplitudes and travel over long distances before they reach a basin. For some basins close to an ocean these long waves showed direct correlation with resonance oscillations. Finally, a tidal current is in an extreme form related to basin-oscillations in Japan (Nakano, 1957). Here the tidal current reached a free stream velocity of $6m/s$ and large eddies triggered oscillations in coastal basins.

Most of the above described mechanisms can be ruled out for the Mok Bay however. In the ten-day period of water level measurements in the Mok Bay at almost every slack (of flood and ebb) oscillations were measured. This excludes causes like (atmospheric) tsunamis and nonlinear wind wave interactions on ground of their occasional character. Instead the tidal current present in the Marsdiep can be related to basin-oscillations in different ways.

Jet-like currents and shear currents

A tidal current can generate a chain of antisymmetric counter-rotating von Karman-like vortices behind an obstacle or (symmetrically) in a jet-like flow. If the frequency of passing of these vortices matches the frequency of a bay or harbor, standing oscillations can be induced (Rabinovich, 2009). In the Mok Bay oscillations are measured at both ebb and flood tide, so the production of vortices should take place at both parts of the tidal cycle. Although during ebb flow such vortices seem to shed-off due to flow deflection by the local coastline (see Fig. 5.20), for flood flow this is not so obvious.

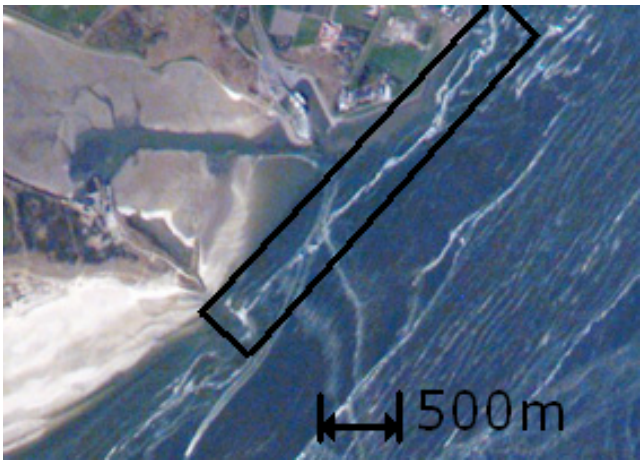

Figure 5.20: Picture taken from NASA ISS space station on May 1st 2007, 13:54:08 UTC above Marsdiep channel. Ebb flow (flow from upper-right to bottom-left) causes the vortex-like structures in the black-lined box, caused by (and downstream of) the sudden change in coastline and bottom topography (possibly a consequent local convergent flow) that causes a foam streak. Length measure inserted to indicate the distance between the mouth of the Mok Bay and the shear layer.

In Fabrikant (1995) the oscillation-problem is approached from the opposite side. Instead of looking for models that describe external pulsations that might force a basin to resonate, here the reflective properties of a shear flow are investigated. A disturbance from the basin itself (travelling outwards) can be reflected by the passing shear flow, and, dependent on a reflection coefficient and phase difference, its reflection can be amplified. Based on the principle that the reflection coefficient R is dependent on shear flow velocity U_0 and frequency ω, Fabrikant (1995) proposes a model that can explain harbor oscillations due to a shear flow.

The growth rate γ for a disturbance corresponding to Kelvin-Helmholtz instability of the vortex sheet (see Fig. 5.22) is expressed as:

$$\gamma = -\frac{\omega^2 a}{\pi n c \sqrt{2}} e^{-2\omega L/U_0} \sin\left(\frac{2\omega L}{U_0} + \frac{\pi}{4}\right). \tag{5.15}$$

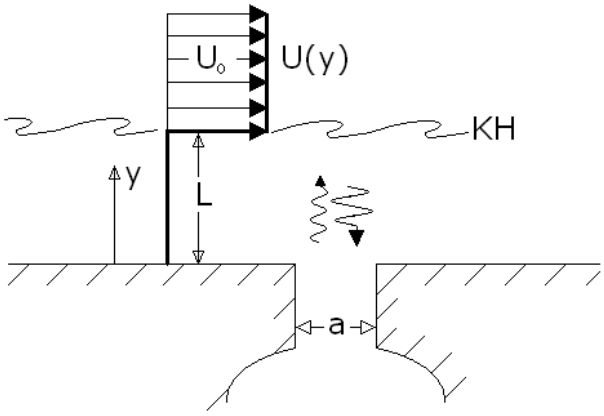

Figure 5.21: Schematic top view of a shear flow at a distance $y = L$ from the open end (with width a) of a basin. Formation of Kevin-Helmholtz instabilities (KH) in the shear layer allow frequency-specific amplification of disturbances from the basin.

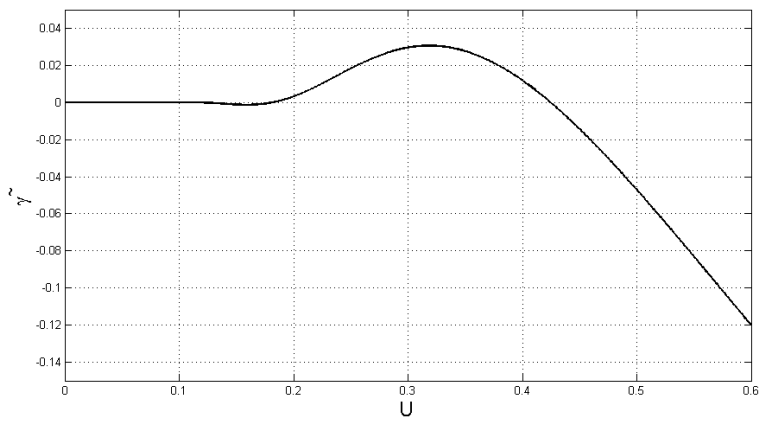

Figure 5.22: Scaled growth rate $\tilde{\gamma} = \gamma/\gamma_{max}$ of harbor oscillations generated by a vortex sheet as a function of the velocity $U = U_0/2\omega L$, as by Fabrikant (1995). Used scaling: $\gamma_{max} = \omega^2 a/(\pi n c\sqrt{2})$.

Here a is the channel width, n the number of wavelengths in the channel and $c = \sqrt{gH}$ the shallow-water wave speed. A uniform depth H in both the basin and the sea is assumed, just as a rectangular neck for the Helmholtz resonator. The maximum growth rate

$$\gamma_{max} = 0.03\frac{\omega^2 a}{\pi n c\sqrt{2}} \tag{5.16}$$

occurs when the flow velocity $U_0 = 0.3(2\omega L)$. From the measurements in the Mok Bay the frequencies of interest (resonance) ω^{ebb} and ω^{flood} are known.

13-Hour measurements in the nearby Marsdiep channel (being the shear flow at distance L from the mouth, with velocity U_0), showed a typical magnitude $U_0 = 1.5$ m/s. This consequently means that the shear layer reflects (the frequencies of interest) the most efficient at typical lengths of $L^{ebb} = 400$ meter and $L^{flood} = 600$ meter. If the foam streak in the black-lined box of figure 5.20 is considered the shear layer, on can see that this really is the typical length between the shear layer and the entrance of the Mok Bay.

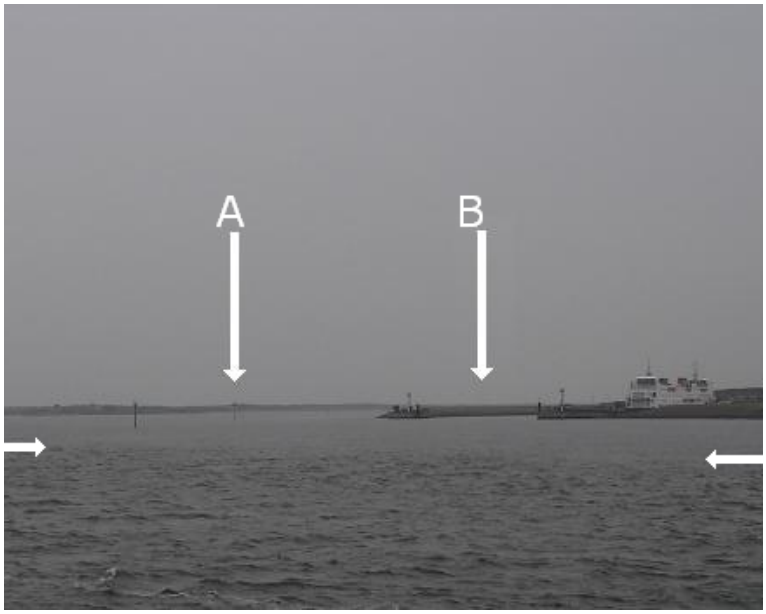

Figure 5.23: Observation of a shear current during flood flow, in front of the entrance of Mok Bay. The sharp border between wavy and calm water indicates the shear layer. Horizontal arrows indicate the shear layer, downward arrows show location of the MK-2 beacon (A) and entrance of TESO Harbor (B). Picture taken on June 8th 2010, approximately 12:00 UTC from R.V. Navicula. Estimated location and direction in which this picture is taken is indicated in figure 3.7

In figure 5.23 the shear layer is visible too, but distances are difficult to estimate. At least for both ebb and flood flow a clear shear flow is observed, which might contribute to the magnitude of the observed oscillations.

Another possibility for the generation of the observed oscillations is the principle of self-oscillation. At high water the Helmholtz frequency is different from the one at low water; it is a function of the water surface area. The sudden change in surface area between high- and low water is mathematically equivalent to a sudden change in system parameters. Such change can trigger oscillations without any external reflection or disturbance, as will be shown in Chapter 6.

5.2.3 Damping properties

A measure of the amount of damping in a harbor (or similar coastal) system can be found in Rabinovich (2009). From the spectral analysis a measure for the width of the resonance peak can be calculated, which is linked to the systems dissipative behavior. This width-measure is called the quality factor, or 'Q-factor', representing the quality of resonance. A highly resonant tuning fork has typically $Q = 1000$ whereas a damper on a door is typically $Q = 0.5$ (highly damped). The expression of the Q-factor according to Rabinovich (2009) is

$$\frac{\Delta f}{f_0} = Q^{-1}. \tag{5.17}$$

where $\Delta f = f^+_{1/2} - f^-_{1/2}$ and the resonant frequency $f_0 = 1/T_0$. Here $f_{1/2}$ indicates the half-power frequency, and can easily be found from the water level power spectra, see figure 5.16. For the Malokurilsk Bay (Japan), depending on the site of measurement within the bay, Q-factors of 9-10 (side) and 12-14 (centre) were found (Rabinovich, 2009).

Similar to the Japanese Malokurilsk Bay, the Mok Bay has distinct peaks in the power spectrum of water level measurements. One difference is that here only ten days of measurements are available, compared to multiple months for the Malokurilsk Bay. Probably more important is that the power spectrum of the Mok Bay represents two states: ebb and flood. According to figure 5.17 the main difference between the two states is at 31.1 and 48.4 cycles per day (roughly no other major changes in the spectra happen), which partly justifies the use of one figure representing two states.

From figure 5.16 two Q-factors can be estimated for the resonances, at 31.1 and 48.4 cycles per day: $Q_{48} = 5.6$ and $Q_{31} = 3.0$. The latter is lower due to the larger side-lobes. These values of Q are comparable to for example the Bay of Fundy and Gulf of Maine ($Q = 5.25$), the North coast of British Columbia ($Q = 9.5$) and as mentioned the Malokurilsk Bay ($Q = 12 - 14$). Super-tidal oscillations are found for large parts of the time series, and thus the Q-factor was not expected to be small. The Chesapeake Bay is considered highly dissipative, having a Q-factor of 0.9. The Mok Bay's characteristic is pretty average compared to the other bays, but more dissipative at flood tide. This again can be explained by the fact that most of the Mok Bay at flood is shallow and the bottom topography less 'even' compared to ebb.

Chapter 6

Self-oscillations

Various phenomena can trigger oscillations in a harbor, bay or lake as described in the previous chapter. Self-oscillations are especially interesting from a mathematical point of view. The different eigenfrequencies of the Mok Bay during ebb and flood tide indicate that the system parameters change as a function of water level. This classifies the system of the Mok Bay as a dynamic system: parameters change as a function of the state variable (water level, or excess volume).

The Mok Bay's bathymetry can roughly be simplified to a step function: a significantly smaller water surface area during ebb tide as compared to flood tide (see figure 6.1). In terms of modeling, this results in two linear systems that are connected by boundary conditions that are imposed by continuity. The separation of the two linear systems (i.e. the sudden change in surface area) is assumed to take place at mean sea level ($\zeta = 0$). This is clearly not the case for the Mok Bay (see figure 6.1), but this is assumed in the simplified model.

In the following both an inviscid and a viscous stepwise linear Helmholtz oscillator are analyzed. Numerical implementations of the analytic system are investigated for its recursive behavior to see any similarities with Maas (1997) and Terra (2005) (multiple equilibria) and Maas and Doelman (2001) (chaotic behavior).

The equation describing a Helmholtz oscillator in terms of the excess volume V (related to the water level ζ) is given by Maas (1997) as

$$\frac{\mathrm{d}^2 V}{\mathrm{d}t^2} + \zeta(V) = Z_e(\sigma t) - r\frac{\mathrm{d}V}{\mathrm{d}t} - \gamma \left|\frac{\mathrm{d}V}{\mathrm{d}t}\right| \frac{\mathrm{d}V}{\mathrm{d}t}. \tag{6.1}$$

In Appendix D the exact (analytic) derivation of the inviscid and viscous response of such system. Here the focus will be more on the system's behavior rather than the corresponding derivation.

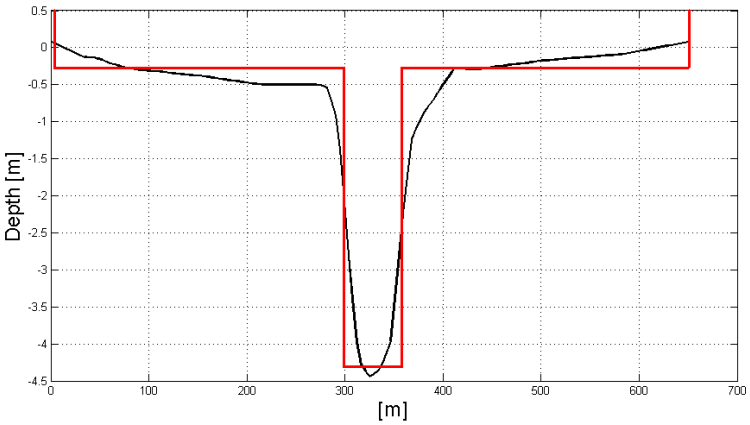

Figure 6.1: Typical cross section of the charted bathymetry of the Mok Bay (black) and simplified bathymetry being a step function (red) as function of height. Depth (in m) relative to N.A.P.

6.0.4 Phase space

A dynamic system is characterized by the fact that the future behavior is determined by its current state, more than being a direct function of time. The current state can be expressed in terms of current values for ζ and $\dot{\zeta}$. To exclude the direct dependence on time, the system's behavior is not plotted as function of time, but of in terms of instantaneous system state-variables. This can for example be water level against water level velocity. Another possibility is the evolution of a single parameter, which is then shown relative to previous values. The water level can for example be shown relative to the same water level but with a phase-delay. Repetitive patterns in time are now 'mapped' on top of each other, time is implicitly visible in the length of the plotted characteristic. This phase-shifted analysis is also called 'analysis in phase space', and will be applied in the following.

As described above, the solution of a driven viscous, linear oscillator consists of a decaying (homogenous) and steady-state (particular) part. The steady-state part is a response with fixed frequency and fixed phase relative to the forcing of the system. This state is reached after the influence of initial conditions has decayed, depending on damping properties. Since the forcing is periodic, the repetitive solution is a single ellipse in phase space. From the moment the system is started, it tends to reach this particular solution: the broken-lined circle in Figure 6.2. The radius of the particular solution is described by (D.18), or, rewritten in terms of the water surface area A,

$$A_P = \frac{F_0/A}{\sqrt{(k/A - \omega^2)^2 + r^2\omega^2}}. \tag{6.2}$$

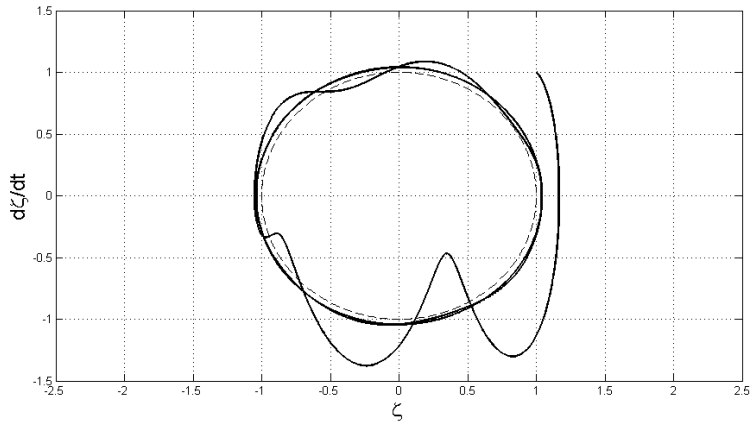

Figure 6.2: Relation between water level ζ and its instantaneous derivative $\dot{\zeta}$ for a simple oscillator. The particular solution (broken line) is reached after decay of the initial conditions, which clearly oscillate around this steady-state solution.

Figure 6.3 shows that a different water surface area (and consequently a different value of ω_0) of the modelled bay results in a new circle to which the system's behavior is 'attracted'. For $\omega < 0.1\omega_0$ however, such a change in amplitude is minor. Under the assumption that $\omega_0 \ll \omega$, (D.18) (which is equal to (6.2)) reduces to

$$A_p = \frac{F_0/A}{\sqrt{\omega_0^4}} = \frac{F_0}{A\omega_0^2}, \tag{6.3}$$

which is independent of ω.

For a step-wise linear oscillator, the transient part of the solution plays a more significant role. For high damping rates, the transient part can be significantly present. Each time the system passes a threshold (say, $\zeta = 0$), the system parameters change and it tries to reach a new end-state. Before the transient part has decayed it will pass the threshold again, keeping the oscillations present.

Continuity of inflow (or the bay's volume $V = \zeta A$) is satisfied by the condition:

$$\dot{\zeta}_{i+1} = \dot{\zeta}_i \frac{A_i}{A_{i+1}}. \tag{6.4}$$

The derivative used to calculate the future part of the analytic solution $(i+1)$ is compensated for a sudden change in water surface area A_{i+1}/A_i. Here, i denotes the HW or LW state. Otherwise an equal large jump would occur in the bay's volume and thus would require a discontinuous inflow. The (excess-) volume of the modelled bay is shown in figure 6.4, where the threshold that triggers the system to switch state is at $\zeta = 0$.

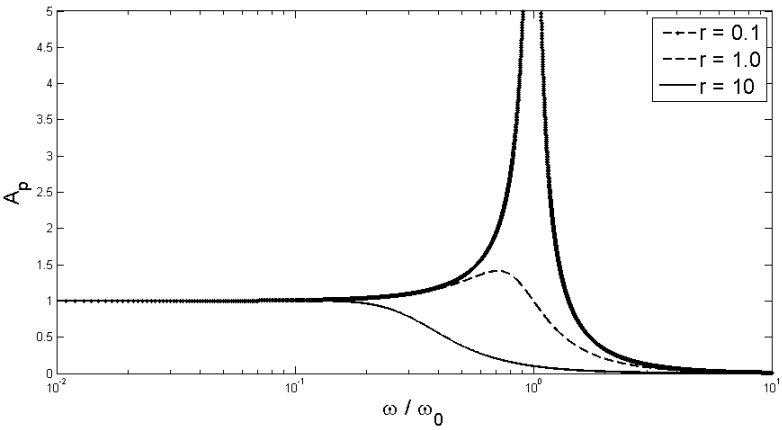

Figure 6.3: Amplitude of the particular solution A_p as function of water surface area A, for a few values of the damping parameter r. Surface area is for convenience defined as $A = \sqrt{\omega/\omega_0}$, when $\omega = 1$. For the range of interest ($\omega < 0.1\omega_0$) the change in amplitude due to change in surface area is very little.

System-locking

The direct time-dependence of the system has been removed from the plotting by using only system parameters, related to the system's current state. Repeating orbits of the system are now easy to detect, especially the repeating consequences of the switching between states (having different water surface area and thus different system parameters). To find whether the system switches states in a fixed pattern, the response within phase space will be investigated in more detail. Although the eigenfrequency of the system is not necessarily an integer multiple of the forcing (tidal) frequency, its response can still be phase-locked. Subsequent cycles of the solution coincide in this case. If more than one of such phase-locked solutions can occur, that are visited randomly, then the response is said to be chaotic. Subsequent crossings of the threshold can give insight in the sensitivity to different initial conditions to the 'amount of phase-lock' in the response. Although each crossing of $\zeta = 0$ (and consequently $V = 0$) new oscillations are triggered in the system, these periods of transient behavior reache a 'steady state'. The system is now said to be *locked* to the forcing. Figure 6.5 shows such behavior in phase-space for about ten steady-state cycles that coincide. The corresponding point of crossing $V = 0$ (for $dV > 0$) is approached as shown in Figure 6.6.

The set of equations ((D.18), (D.20), (D.21), (D.22) and (D.24)) still has plenty of system parameters to vary. This makes it very difficult to analyze the system's behavior throughout parameter space (the range of all possible parameter combinations) efficiently. By scaling amplitudes, phases

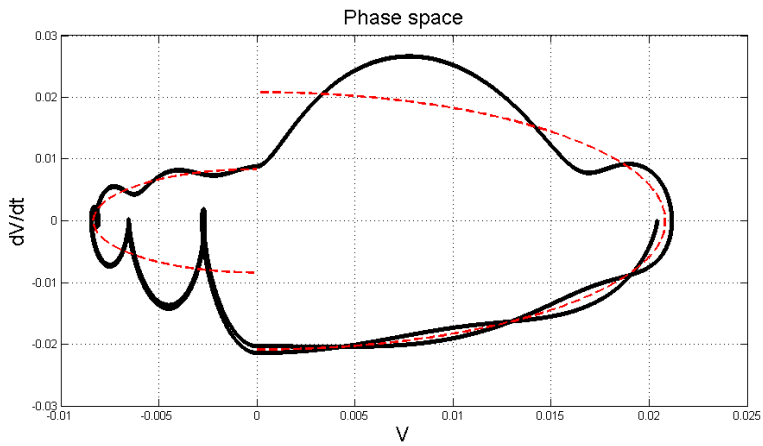

Figure 6.4: The use of continuity conditions around $\zeta = 0$ closes the characteristic to a continuous function ($dV/dt = \dot{\zeta}A$ and $V = \zeta A$). Broken-lined semi-circles (red) indicate the steady state solution for the separate steady-state solutions for each state of the bay (high, low water) to which the characteristic tends to decay. Used parameters: $\omega/\omega_n = 1/11$ (at LW), $\omega/\omega_p = 1/7$ (at HW), $r = 2.0$ and $k = 1.0$.

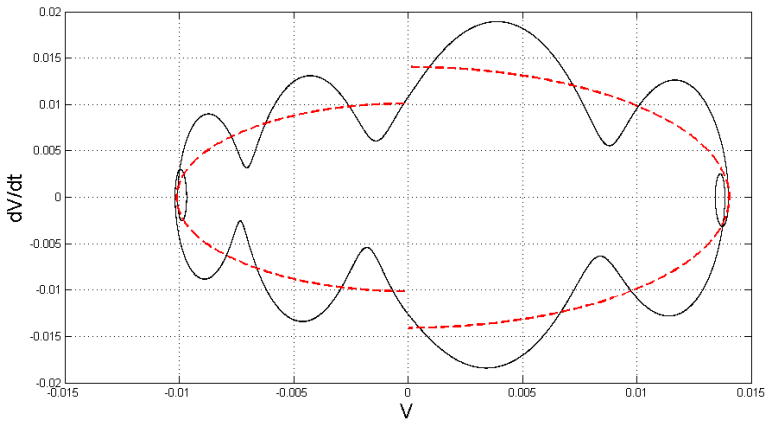

Figure 6.5: Steady-state behavior of the modeled Helmholtz oscillator. Used parameters: $\omega/\omega_n = 1/10.0$, $\omega/\omega_p = 1/8.50$, $r = 0.1$ and $k = 1$.

and frequencies, the number of parameters can be reduced. Linearization can in turn be done using some assumptions regarding various magnitudes.

6.0.5 Simplification and linearization

With the above mentioned set of expressions for A_h, ϕ_h, A_p and ϕ_p, the most general form of the exact solution can be composed. However we do not have an exact expression for the duration of a half cycle, which is obtained by

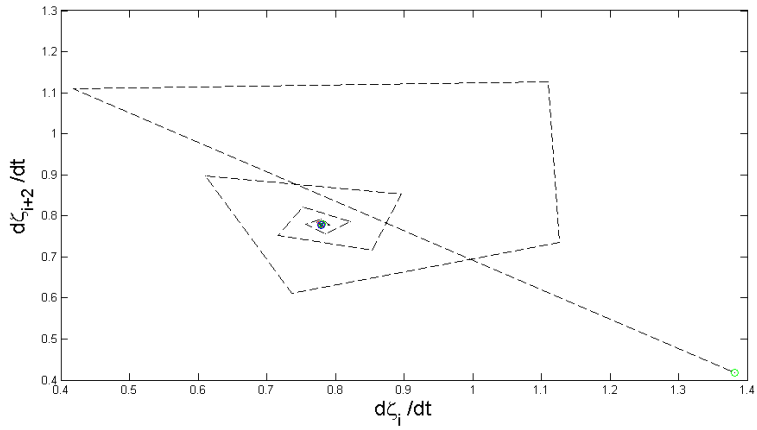

Figure 6.6: From the first low- to high water crossing (green circle) the subsequent crossing's behavior is attracted to a fixed equilibrium state, which is reached after about 15 forcing cycles. Used parameters: $\omega/\omega_n = 1/10.0$, $\omega/\omega_p = 1/8.50$, $r = 0.1$ and $k = 1$.

a zero-finding procedure. The simplified expression of this duration will be used to find a linearized expression for the next instant at which the system switches states (and thus its system parameters). Having such an expression, one can now try to find a recurrence relation describing the system *including* switching of states.

The exact solution is stated again here for convenience,

$$x(t) = A_h e^{-\gamma t} \sin\left(\omega' t + \phi_h\right) + A_p \cos\left(\omega t - \phi\right). \tag{6.5}$$

To eliminate ϕ and turn the forcing into a sine function (first zero at $t \approx \pi$), the following substitutions have been inserted:

$$\begin{aligned} \phi = \left(\omega t_* - \frac{\pi}{2}\right) \quad &\rightarrow \quad t_* = \left(\frac{\phi + \frac{\pi}{2}}{\omega}\right) = \left(\frac{\phi}{\omega} + \frac{\pi}{2\omega}\right) \\ t' = t - t_* \quad &\rightarrow \quad t = t' + t_* \end{aligned} \tag{6.6}$$

The solution now reads:

$$\begin{aligned} x(t) &= A_h e^{-\gamma[t'+t_*]} \sin\left(\omega'[t' + t_*] + \phi_h\right) + A_p \cos\left(\omega[t' + t_*] - \omega t_* - \frac{\pi}{2}\right) \\ &= A_h e^{-\gamma[t'+t_*]} \sin\left(\omega'[t' + t_*] + \phi_h\right) + A_p \cos\left(\omega t' - \frac{\pi}{2}\right) \\ &= A_h e^{-\gamma[t'+t_*]} \sin\left(\omega' t' + \omega' t_* + \phi_h\right) + A_p \sin\left(\omega t'\right) \end{aligned} \tag{6.7}$$

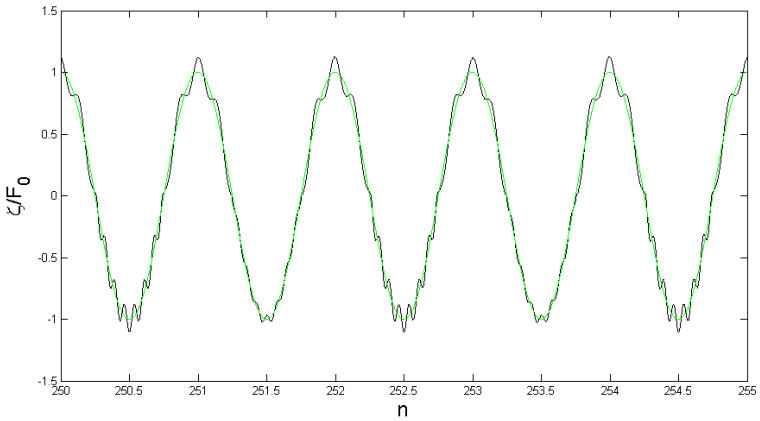

Figure 6.7: Time series of the viscous, stepwise linear Helmholtz oscillator. Amplitude of the response scaled by the forcing F_0, shown against the number of forced periods n. Oscillations are 'modulated' with a frequency being half that of the forcing, resulting in a period-2 motion. Used parameters: $\omega/\omega_n = 1/14.12$, $\omega/\omega_p = 1/7.06$, $r = 0.01$ and $k = 1$.

One expression containing ω, $\phi = \phi(\phi_d)$ and $\omega' = \omega'(\gamma)$ is obtained by using

$$\begin{aligned}\phi_h' &= \omega' t_* + \phi_h \\ &= \omega' \left(\frac{\phi}{\omega} + \frac{\pi}{2\omega}\right) + \phi_h \\ &= \frac{\omega'}{\omega}\left(\phi + \frac{\pi}{2}\right) + \phi_h, \end{aligned} \tag{6.8}$$

yielding

$$x(t') = A_h e^{-\gamma(t'+t_*)} \sin\left(\omega' t' + \phi_h'\right) + A_p \sin(\omega t'). \tag{6.9}$$

This can in turn be simplified by scaling time $\tilde{t} = \omega t'$, frequency $\tilde{\omega} = \omega'/\omega$, amplitude $\tilde{A}_h = A_h e^{-\gamma t_*}$ and $\tilde{x}(\tilde{t}) = x(\tilde{t})/A_p$ to find

$$\tilde{x}(\tilde{t}) = \tilde{A}_h e^{-\tilde{\gamma}\tilde{t}} \sin\left(\tilde{\omega}\tilde{t} + \phi_h'\right) + \sin\left(\tilde{t}\right), \tag{6.10}$$

where $\tilde{\gamma} = \gamma/\omega$. Initial conditions $\tilde{x}(\tilde{t} = 0) = 0$ require that $\phi_h' = j\pi$, for $j \in \mathbb{N}$. The case for which $j = 0$ has physically the same meaning as $j = 2, 4, \ldots$ so that only a distinction between $j = 0$ (first term on RHS positive) and $j = 1$ (first term on RHS negative) should be made. The term ϕ_h' is thus left out and the fact that $\tilde{A}_h$ can be both positive and negative is kept in mind:

$$\tilde{x}(\tilde{t}) = \tilde{A}_h e^{-\tilde{\gamma}\tilde{t}} \sin\left(\tilde{\omega}\tilde{t}\right) + \sin\left(\tilde{t}\right). \tag{6.11}$$

This form of the solution clearly shows two superposed sines which fulfill the initial conditions and have an amplitude ratio of $\tilde{\omega}$.

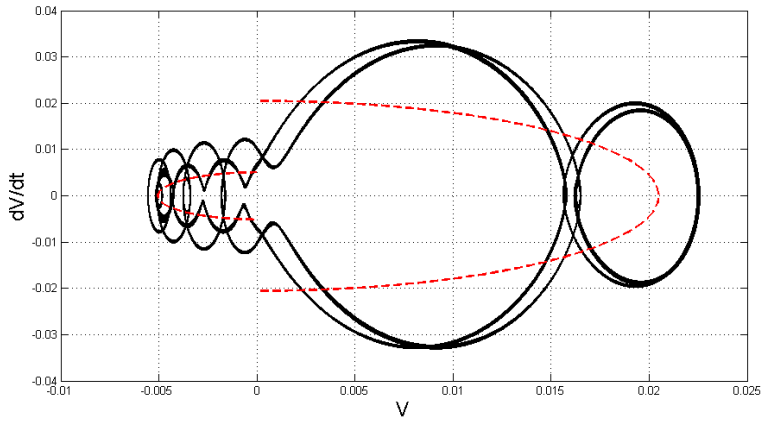

Figure 6.8: Phase-space representation of Figure (6.7), where the two states (alternated with $\omega = 0.5\omega$) are clearly present: the response passes through similar points every 2nd loop. Used parameters: $\omega/\omega_n = 1/14.12$, $\omega/\omega_p = 1/7.06$, $r = 0.01$ and $k = 1$.

Finding zeros in $\tilde{x}(\tilde{t})$

The first instant of $\tilde{x}(\tilde{t} > 0) = 0$ is estimated to be around $\tilde{t} \approx \pi$. An expression for this instant is

$$\tilde{t} = \pi + \epsilon\tilde{T}, \tag{6.12}$$

where $\epsilon \ll 1$ and $\tilde{T} = \mathcal{O}(1)$. Inserting this yields

$$\tilde{x}(\pi + \epsilon\tilde{T}) = 0 = \tilde{A}_h e^{-\gamma(\pi+\epsilon\tilde{T})} \sin\left(\tilde{\omega}(\pi + \epsilon\tilde{T})\right) + \sin(\pi + \epsilon\tilde{T}). \tag{6.13}$$

This can be fulfilled in two ways, either $\tilde{\omega} \in \mathbb{N}$ (zero by argument) or $\tilde{A}_h = \mathcal{O}(\epsilon)$ (equal but opposite amplitudes). So far, only the term $\epsilon\tilde{T}$ is considered small: both ω and ω' are still considered to be of the same order of magnitude. If they were not, $\tilde{\omega}$ did not have to be an integer (natural) number as will become clear later. Linearization of the separate terms in (6.13) around $\tilde{t} = \pi + \epsilon\tilde{T}$ gives the following approximations:

$$\tilde{A}_h e^{-\tilde{\gamma}(\pi+\epsilon\tilde{T})} = \left(1 - \tilde{\gamma}\epsilon\tilde{T}\right) \tilde{A}_h e^{-\tilde{\gamma}\pi} \tag{6.14}$$

$$\begin{aligned} \sin\left(\tilde{\omega}(\pi + \epsilon\tilde{T})\right) &= \sin(\tilde{\omega}\pi)\cos(\epsilon\tilde{T}) + \cos(\tilde{\omega}\pi)\sin(\epsilon\tilde{T}) \\ &\approx \sin(\tilde{\omega}\pi) + \epsilon\tilde{T}\cos(\tilde{\omega}\pi) \end{aligned} \tag{6.15}$$

$$\begin{aligned} \sin(\pi + \epsilon\tilde{T}) &= \sin(\pi)\cos(\epsilon\tilde{T}) + \cos(\pi)\sin(\epsilon\tilde{T}) \\ &\approx -\epsilon\tilde{T}, \end{aligned} \tag{6.16}$$

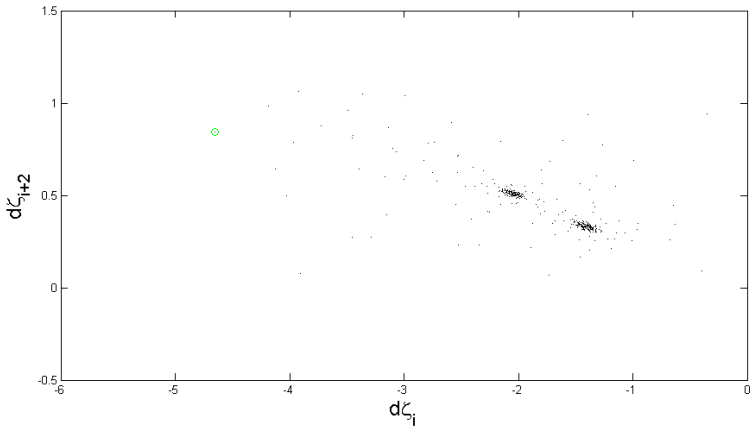

Figure 6.9: Phase-space representation of subsequent derivatives of the water level ($d\zeta/dt$) at the crossing from $\zeta < 0$ to $\zeta > 0$. After decay of the start-up behavior (last 25% of 400 periods are shown) an equilibrium position consisting of two states is visible.

so that

$$0 = \left(1 - \tilde{\gamma}\epsilon\tilde{T}\right) \tilde{A}_h e^{-\tilde{\gamma}\pi} \left(\sin(\tilde{\omega}\pi) + \epsilon\tilde{T}\cos(\tilde{\omega}\pi)\right) - \epsilon\tilde{T}. \tag{6.17}$$

Case I: $\omega/\omega' = \mathcal{O}(1)$

Consider the case where the frequency of forcing is close to the frequency of resonance, i.e. $\omega' = \mathcal{O}(\omega)$, then $\tilde{A}_h$ is expected to be finite and of order ϵ. Small-amplitude motion is required in order to find intersections of $x = 0$ close to those expected based on the forcing function. In this case the terms of order ϵ can be neglected in the first term on the RHS, yielding

$$\tilde{A}_h e^{-\tilde{\gamma}\pi} \sin(\tilde{\omega}\pi) - \epsilon\tilde{T} \approx 0. \tag{6.18}$$

Again use $\tilde{A}_h = A_h/A_p$ and insert $A = \epsilon A_h = \epsilon A_p \tilde{A}_h$from which follows that

$$\epsilon A_p(\tilde{A}_h \sin(\tilde{\omega}\pi) - \tilde{T}) \approx 0, \tag{6.19}$$

and consequently $\tilde{T}$ can be found as

$$\tilde{T} = \tilde{A}_h \sin(\pi\tilde{\omega}). \tag{6.20}$$

Case II: $\omega/\omega' \ll 1$

Obviously more applicable to the Mok Bay is the case where the frequency of resonance is much higher than the frequency of forcing, so that $\epsilon = \omega/\omega' \ll$

1. Insert this into (6.11) to find the expressions for $x(t)$ and its derivative $\dot{x}(t)$:

$$\begin{aligned} x &= \epsilon A e^{-\gamma t} \sin\left(\frac{\omega'}{\omega} t\right) + \sin(t) \\ &= \epsilon A e^{-\gamma t} \sin\left(\frac{t}{\epsilon}\right) + \sin(t) \end{aligned} \tag{6.21}$$

and its derivative

$$\dot{x} = A e^{-\gamma t} \left[\cos\left(\frac{t}{\epsilon}\right) - \gamma\epsilon \sin\left(\frac{t}{\epsilon}\right)\right] + \cos(t). \tag{6.22}$$

Again the instant at $t = \pi + \epsilon\tilde{T}$ is considered and using the linearization introduced earlier, this yields

$$x = \epsilon A e^{-\gamma\pi}(1 - \epsilon\gamma\tilde{T}) \sin\left(\frac{\pi}{\epsilon} + \tilde{T}\right) - \epsilon\tilde{T}. \tag{6.23}$$

Substitute $\hat{A} = Ae^{-\gamma\pi}$ and neglect terms of order ϵ in the first term on the RHS to obtain

$$\epsilon\left[\hat{A}\sin\left(\frac{\pi}{\epsilon} + \tilde{T}\right) - \tilde{T}\right] = 0. \tag{6.24}$$

The argument in the expression above has physical meaning only over a certain interval, defined by the floor function. Outside this interval, 2π can be added or subtracted to yield the exact same result. The floor function of the current argument is expressed as

$$\varphi = \lfloor\frac{\pi}{\epsilon}\rfloor = \pi\left(\frac{1}{\epsilon} - 2n\right), \tag{6.25}$$

where n is chosen such that the argument is within the effective interval, and $n \in \mathbb{N}$. Inserted into (6.24) this becomes

$$\hat{A}\sin(\varphi + \tilde{T}) - \tilde{T} = 0, \tag{6.26}$$

which can be written even simpler by using the substitution $E = \varphi + \tilde{T}$:

$$\varphi = E - \hat{A}\sin(E) \tag{6.27}$$

This expression is known as Kepler's equation describing the (polar) position of a celestial body (like a planet) and the time elapsed from a given initial point. Here it is the relation between ζ and $\dot{\zeta}$ in phase-space describing such orbit. Equation (6.27) has a known solution for E (provided $A < 1$) and consequently it can be solved for $\tilde{T}$, since $E = E(\tilde{T})$:

$$E = \varphi + \sum_{n=1}^{\infty} \frac{2}{n} J_n\left(n\hat{A}\right) \sin(n\varphi). \tag{6.28}$$

Substituting $\tilde{T} = E - \varphi$ back simply yields

$$\tilde{T} = \sum_{n=1}^{\infty} \frac{2}{n} J_n \left(n\hat{A} \right) \sin(n\varphi), \tag{6.29}$$

where J_n is the Bessel function of the first kind, i.e. the solution to the Bessel differential equation.

Application

It is now possible to write an analytic approximation for the time instants where $x = 0$. This in turn can be coupled to find similar crossings, i.e. being *one* cycle separated instead of half a period. The analysis of periodic similarities can give insight whether this system of coupled linear oscillators can experience nonlinear (and eventually chaotic) behavior.

From (6.29) an expression for $\tilde{T}$ is found and from (6.22) it follows that

$$\begin{aligned} \dot{x}_0 &= A + 1 = A + \frac{C}{C} \\ \dot{x}_{1/2} &= BA + C, \end{aligned} \tag{6.30}$$

at $(t = 0)$ and $(t = \pi + \epsilon\tilde{T})$ respectively, where

$$\begin{aligned} B &= e^{-\gamma(\pi+\epsilon\tilde{T})} \left[\cos\left(\frac{\pi + \epsilon\tilde{T}}{\epsilon} \right) - \gamma\epsilon \sin\left(\frac{\pi + \epsilon\tilde{T}}{\epsilon} \right) \right] \\ C &= \cos\left(\pi + \epsilon\tilde{T} \right). \end{aligned}$$

This can be rewritten to

$$\dot{x}_0 = A + \frac{C}{C}. \tag{6.31}$$

$$\frac{\dot{x}_{1/2}}{C} = \frac{B}{C} A + \frac{C}{C} \tag{6.32}$$

If one subtracts (6.31) from (6.32) and solves for $\dot{x}_{1/2}$, an analytic expression linking the derivatives of two subsequent crossings of $x = 0$ is found:

$$\dot{x}_{1/2} = \dot{x}_0 C + AC \left(\frac{B}{C} - 1 \right). \tag{6.33}$$

In the case of different water surface areas at low- and high water, continuity of inflow and water level require that the RHS of (6.33) is compensated according to (6.4). In (6.33), A itself is a function of $\dot{x}_0$ according to (6.30): $A = \dot{x}_0 - 1$. Similarly, $\tilde{T}$ is a function of A (and consequently of $\dot{x}_0$) and thus are B and C too.

$$\begin{aligned} \dot{x}_{1/2} &= \dot{x}_0 C + (\dot{x}_0 - 1)\, C \left(\frac{B}{C} - 1 \right) \\ \dot{x}_{1/2} &= B_1 (\dot{x}_0 - 1) + C_1, \end{aligned} \tag{6.34}$$

Subscript 1 indicates that the corresponding term is evaluated using ϵ_1 (being the HW for sine-forcing) and $\dot{x}_0$. For $\dot{x}_1$ this yields

$$\dot{x}_1 = B_2\left(\dot{x}_{1/2} - 1\right) + C_2. \tag{6.35}$$

Here the subscript refers to use of ϵ_2 and evaluation at $\dot{x}_{1/2}$, which can be rewritten to $\dot{x}_0$ using (6.34). Combine this to form

$$\dot{x}_1 = \left\{\frac{\epsilon_2^2}{\epsilon_1^2}\right\} B_2 \left\{ \left(\frac{\epsilon_1^2}{\epsilon_2^2}\right)\left[B_1\left(\dot{x}_0 - 1\right) + C_1\right] - 2\right\} + C_2, \tag{6.36}$$

where

$$\begin{aligned}
B_1 &= B\left\{\epsilon_1, \tilde{T}\left[\hat{A}(\dot{x}_0)\right]\right\} \\
B_2 &= B\left\{\epsilon_2, \tilde{T}\left[\hat{A}(\dot{x}_{1/2})\right]\right\} \\
C_1 &= C\left\{\tilde{T}\left[\hat{A}(\dot{x}_0)\right]\right\} \\
C_2 &= C\left\{\tilde{T}\left[\hat{A}(\dot{x}_{1/2})\right]\right\}
\end{aligned}$$

and the fractions containing ϵ_i are inserted by continuity. In order to eliminate $\dot{x}_{1/2}$ completely, again (6.34) will be substituted:

$$\begin{aligned}
\hat{A}(\dot{x}_0) &= \left(\dot{x}_0 - 1\right)e^{-\gamma\pi} \\
\hat{A}(\dot{x}_{1/2}) &= \left(\left[B_1\left(\dot{x}_0 - 1\right) + C_1\right] - 1\right)e^{-\gamma\pi}.
\end{aligned}$$

Calculation of recursive system behavior

As shown above, an analytic start is made to find properties of the periodic behavior of the coupled oscillators. Theoretically an infinite sum of Bessel functions is required to find $\tilde{T}$, according to (6.29). This is impractical by computational means and a simple calculation shows the outcome of $\tilde{T}$ as function of the number of summed Bessel functions. Figure 6.10 shows a typical behavior for the current calculations (model, assumptions, etc.) and thus no more than the first hundred Bessel functions of the first kind are used.

One can now find properties of the periodic crossing of $x = 0$ ($\dot{\zeta} > 0$), see Figure 6.12. The procedure to actually calculate the periodic behavior of the system is as follows:

- having an initial condition ($t = 0$, $\dot{x}(0) = v_0$), the solutions $x(t)$ and $\dot{x}(t)$ can be calculated exact using $A = v_0 - 1$ from (6.22) in (6.21);

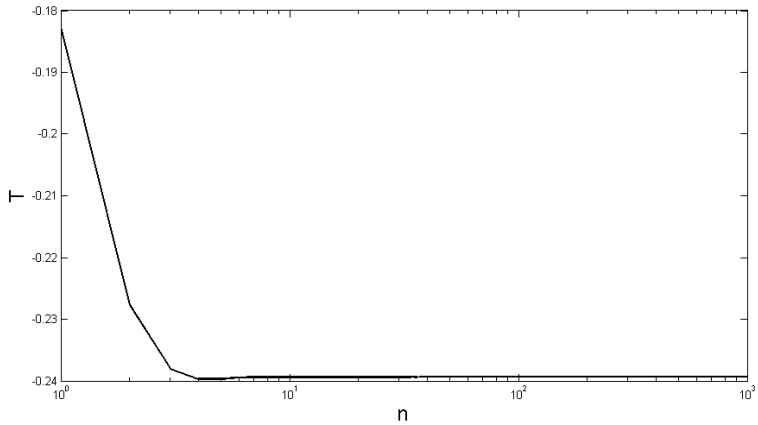

Figure 6.10: Asymptotic behavior of the number of summed Bessel functions (n) in the solution to Kepler's equation (T). For the calculation performed here no more than the first hundred Bessel functions (first kind) are necessary: the further increase in accuracy is very little.

- $\epsilon\tilde{T}$ is approximated by the finite Bessel summation under the condition $x(t = \pi + \epsilon\tilde{T}) = 0$;
- $\dot{x}(t = \pi + \epsilon\tilde{T})$ is interpolated from the exact solution;
- $\dot{x}(t = \pi + \epsilon\tilde{T})$ is multiplied by a factor expressing the areal ratio to assure continuity of inflow and water level of the modeled bay;
- having the new initial condition on $\dot{x}$ and defining the time at this instant to be zero, one follows the procedure from start again.

Although this procedure finds the subsequent (half-period) crossings of $x = 0$, every second result of it yields the one-cycle intersections with the Poincaré plane ($\zeta = 0$ and $\dot{\zeta} > 0$). Note that in the following $\dot{\zeta} = \dot{x} = v$ is used. In summary, one can state that

$$\dot{\zeta}\left(t_{1/2}\right) = F_a\left[\dot{\zeta}\left(t_0\right)\right]$$
$$\dot{\zeta}\left(t_1\right) = F_b\left[\dot{\zeta}\left(t_{1/2}\right)\right].$$

Equivalently, linking two passings of the Poincaré plane (being separated by one cycle), this corresponds to

$$\dot{\zeta}\left(t_1\right) = F_b\left\{F_a\left[\dot{\zeta}\left(t_0\right)\right]\right\}. \tag{6.37}$$

An example of such a function $F_b(F_a(\dot{\zeta}))$ is shown in Figure 6.11. The broken black line indicates the bisector. If the intersection with the bisector happens with a slope of less than -1, the following intersections will spiral

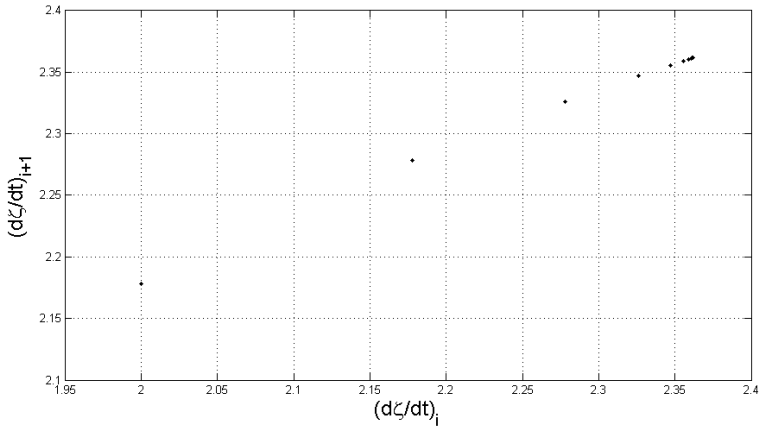

Figure 6.11: Subsequent values for $\dot{\zeta}$ of the intersections of the Poincaré plane over time. The initial value of $\dot{\zeta} = 2$ converges in time to $\dot{\zeta} \approx 2.36$. Used damping parameter setting: $\gamma = 0.11$.

away: this equilibrium is unstable. Having a slope of exactly -1, the system is in equilibrium and experiences two distinct intersections with the bisector. In the case of a slope larger than -1 the system will spiral towards one fixed intersection: the system is stable (Adams, 2002).

Poincaré plane

Now consider the plane $\zeta = 0$, $\dot{\zeta} > 0$ and mark all crossings of it with a dot. Such plane is called a *Poincaré plane* and shows the system's stability in a very easy way. If subsequent dots coincide, the system is apparently in a steady state, as a linear system would be. For a slightly different system parameter a new crossing of the Poincaré plane might be found, showing a new equilibrium state.

A typical example of a system consisting of simple nonlinear equations which experiences a chaotic response is the logistic map

$$x_{n+1} = rx_n(1 - x_n). \tag{6.38}$$

If the position of the crossing of the Poincaré plane is shown as function of a system parameter, one obtains a bifurcation tree, see Figure 6.14. Starting with $r = 2.4$, only one value for x is found. The system is thus in a steady-state (one-cycle motion). Increasing the system parameter r up to 3.0, a first *bifurcation* occurs. In such state, the system experiences similar crossings every *second* cycle: the two-cycle motion. This happens again for $r \approx 3.45$, bringing the system in a repeating cycle of four periods: the four-period motion. A bifurcation point is thus the point at which the circumstances force the system into a higher-period motion; further bifurcations occur before

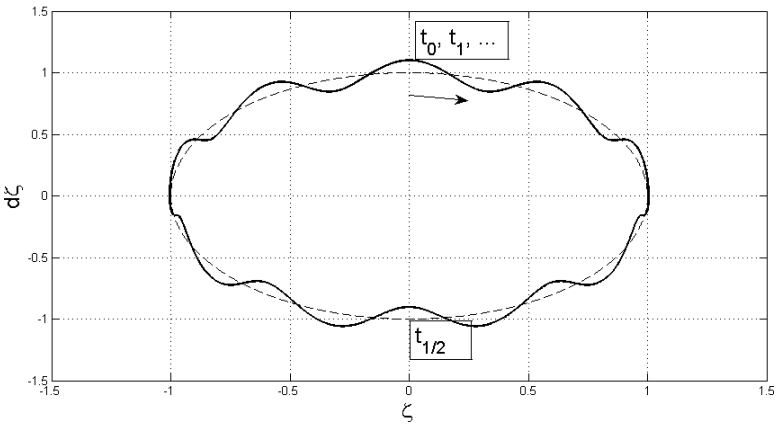

Figure 6.12: Behavior in phase-space of the example-function $\zeta = \sin(t) + 0.01\sin(10t)$. The dynamic system will switch parameters (radius in phase-space) when crossing $\zeta = 0$, which is excluded here. From t_0 (at $\zeta = 0$) the system travels in the direction of the arrow, until it reaches $t_{1/2}$, again at $\zeta = 0$. Here the system switches from its high water state to a low water state, to the instant of t_1 (back at $\zeta = 0$). Finding a relation between t_0, t_1, ... can give insight in periodic system behavior.

the system reaches the chaotic regime. Slight changes in initial conditions result in dramatic changes in the end situation: a main characteristic of chaos. An example of period-2 motion of the piecewise-linear oscillator that models the Mok Bay can be found in figure 6.7 and 6.8.

Bifurcations and higher-period motion

A linear Helmholtz oscillator experiences a fixed amplitude and phase after decay of initial conditions, as shown in the above derivation. This means that for a single linear Helmholtz oscillator each passing of ($\zeta = 0$, $\dot{\zeta} > 0$) the conditions of ζ and $\dot{\zeta}$ will be equal. For both the original and linearized model (consisting of two coupled linear models) however, higher-period motion is found. For certain parameters not every *first* crossing, but every *second* crossing has similar conditions, at least in the linearized model. This is a first indication that the behavior of the oscillator might experience transition to chaotic behavior by *bifurcations*. Bifurcations are the points at which the system gets into a new equilibrium state. This can consist of multiple stable (and unstable) points: the higher-period motion. Of the various types of bifurcations, the bifurcation tree in figure 6.14 describes the period-*doubling* motion. Under conditions of an increasing system parameter (on x-axis), the periodic motion of the oscillator is doubled to period-2, doubled again to period-4 motion, etc. before chaos is observed.

The original analytic model (D.9) shows also (for certain parameter settings) each third (see figure 6.16), fourth, ..., eleventh period similar con-

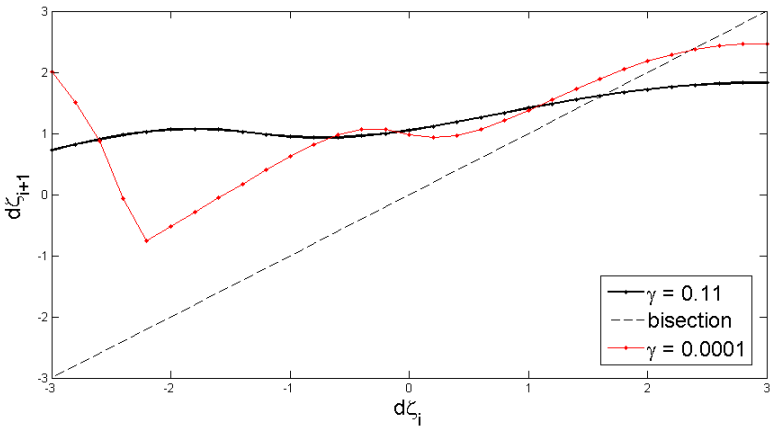

Figure 6.13: Subsequent values for $\dot{\zeta}$ of the intersections of the Poincaré plane, now as function of its preceding value. The black broken line indicates the bisector of the axes. The slope at the intersection with the bisector indicates the stability of the function. Two different values for the damping parameter γ are shown.

ditions of crossing. Though after for example the period-11 motion, the system is stabilized again yielding period-3 motion. Such bifurcations are comparable to the piecewise-linear oscillator described by Coombes and Osbaldestin (2000), modeling the human neural response. Here period-*adding* bifurcations are found and the corresponding bifurcation diagram consists of windows of periodicity and chaos. Yang and Lu (2004) found period-adding bifurcations without intermediate chaotic regimes (also in a model describing neural oscillatory responses and also consisting of a piecewise-linear oscillator). Duarte *et al.* (2006) reported similar (discontinuous) return maps (Poincaré representations) as found in this thesis (see figure 6.16), having both period-doubling bifurcations and saddle-node bifurcations.

As can be seen in figure 6.17, the underlying characteristics of subsequent passings of the Poincaré plane are significantly different for the original (o) and linearized model (x). This indicates that for initial conditions $\zeta_0 \approx 1$ (very small oscillations around the sine forcing, which local derivative is equal one) the models might be similar, for larger initial values of $\dot{\zeta}$ the assumptions at the linearization is not accurate enough for further comparison.

The bifurcation diagram of the piecewise linear Helmholtz oscillator can be found in 6.18. A bifurcation diagram with higher resolution should be made using a more efficient algorithm and more general nonlinearity parameter. The varied parameter γ represents only friction, whereas nonlinearity is varied more directly by the forcing, ratio of water areas etc. Decreasing the amount of parameters (ideally into one nonlinearity parameter) is also recommended.

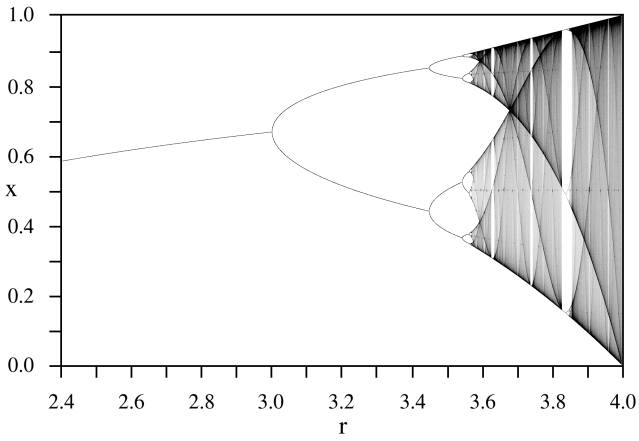

Figure 6.14: Bifurcation diagram for the logistic map $x_{n+1} = rx_n(1 - x_n)$. For increasing system parameter r through period-doubling bifurcations finally the chaotic regime is reached ($r > 3.6$). Clearly visible are the period-doubling bifurcations at $r \approx 3.0$, $r \approx 3.45$, etc. and system stabilization at $r \approx 3.82$. From $http://en.wikipedia.org/wiki/Bifurcation_diagram$.

Conclusion

Further investigation on the presented piecewise linear Helmholtz oscillator can give insight whether its behavior in parameter space is described by period-adding bifurcations (and possibly) with intermediate regimes of chaos, as described by Coombes and Osbaldestin (2000), Duarte *et al.* (2006) and Yang and Lu (2004). Localizing the shallow Mok Bay in parameter space can in turn show the theoretical presence (or absence) of such behavior for *this* bay.

Both the presented model and its implementation are thus topic of further research since hardly anything is documented on dynamics of driven, viscous, piecewise-linear Helmholtz oscillators. A better linearization might be related to small variations in *derivative* ($\dot{\zeta}$), rather than amplitude (ζ). Such linearization can be used to find a simplified analytic expression, from which directly specific parameters can be found that lead to bifurcations (slope -1 in return map). Both the simplified model and a reduced number of parameters (that span the parameter space) will yield a more efficient calculation of system behavior (return map or Poincaré plane, bifurcation diagram).

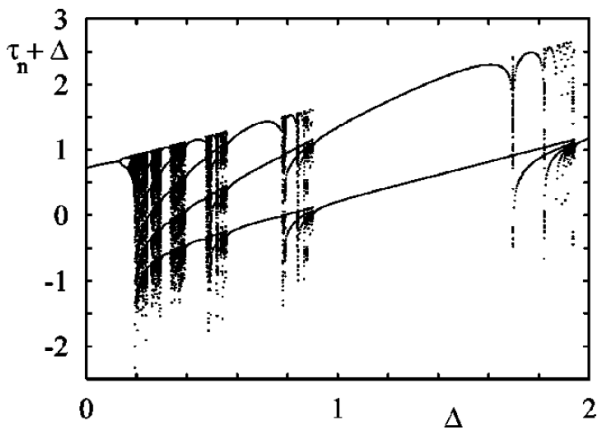

Figure 6.15: Period-adding bifurcation diagram for the neuron-oscillator as described by Coombes and Osbaldestin (2000). For stimuli period $\Delta < 0.1$ one finds period-1 motion which soon becomes chaotic motion for increasing Δ. Stabilization occurs however, yielding period-6 motion ($\Delta \approx 0.22$), followed by a chaotic regime, period-5 motion, etc. From Coombes and Osbaldestin (2000).

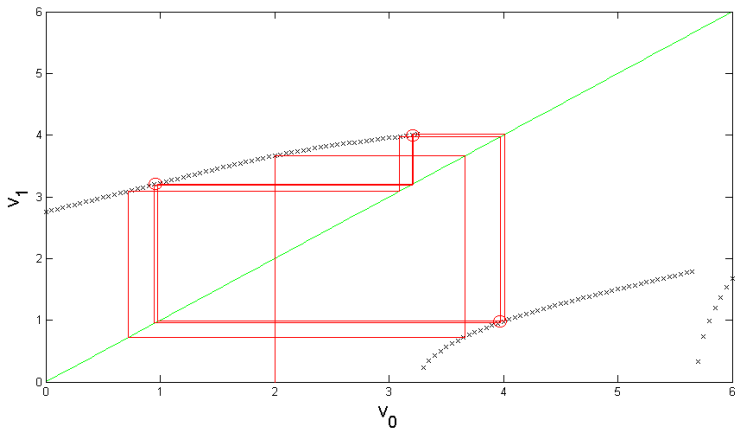

Figure 6.16: Discontinuous return map (x) of the subsequent crossings of the Poincaré plane, as response to an initial condition of $\dot{\zeta}_0 = v_0 = 2$ (red line). After a few periods the stable period-3 motion (marked by red circles) is reached. Used parameters: $\omega_1 = 12.12$, $\omega_2 = 8.06$, $\gamma = 0.1$ and $\Delta t = 0.001$.

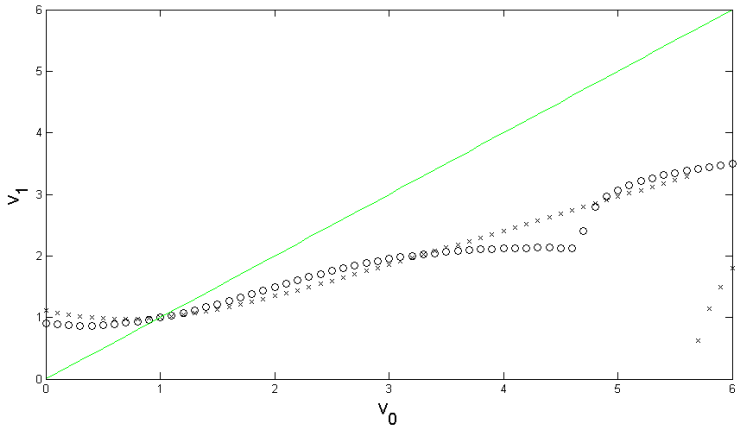

Figure 6.17: Underlying characteristics of the subsequent passings of the Poincaré plane for the analytic (o) and linearized model (x). The single-frequency sine function has local derivative equal one at intersection of the Poincaré plane, explaining why the linearized and analytic model coincide for this point: the oscillations are small enough for the linearization assumptions to be valid. The local slope at the intersections with the bisector (green) indicates whether these are (in)stable equilibriums.

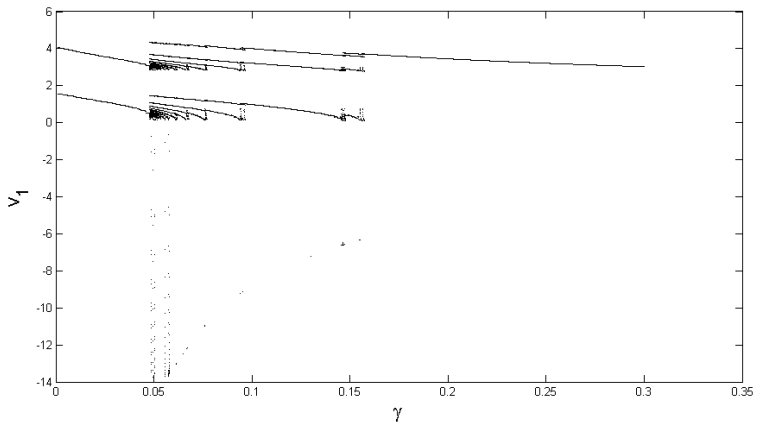

Figure 6.18: Bifurcation diagram for the piecewise linear Helmholtz oscillator as function of the friction parameter $\gamma = c/2m$. Used parameters: $\omega_1 = 12.12$, $\omega_2 = 8.06$ and $\Delta t = 0.01$.

Chapter 7

Discussion

Based on the theoretical proof that an almost-enclosed co-oscillating bay can behave as a nonlinear Helmholtz resonator, measurements have been performed at the entrance and head of the Mok Bay (Texel, the Netherlands). Traditional analysis (harmonic and Fourier analysis) have been applied and show agreement with the nearby obtained results from 5-year ferry observations.

Splitting the measurements in a high- and low water series allowed for separate analysis of the Mok Bay during these events. Using LSHA (allowing gaps in time series) two distinct frequencies of resonance were linked to high and low water. Together with high coherence between water *level* and water *flow* at these frequencies, the Helmholtz model turned out to describe the oscillations well. Oscillations in water level might be small, $\mathcal{O}(0.01)$, the corresponding flow oscillations are of the order of the tidal flow, $\mathcal{O}(1)$. This shows the significance of understanding the system behavior, especially if it is highly nonlinear.

Measurements with the TUD jet ski and the GPS-tracked waterline resulted in an estimation of the hypsometric curve of the Mok Bay, yielding dimension estimates for the Helmholtz model. For both high- and low water, the model made an overestimation of about (10%). This can however be attributed to the effective entrance width being smaller than the real width due to wall- and bottom friction. Also, the length of the channel in practice can differ from our estimate from the depth measurements.

The obtained time series is however too short (9 days) to quantify any presence of chaotic behavior. Wind-setup can have a major influence on the water level, especially for such short series. Consequently an analytic model was set up to analyze the behavior of two coupled Helmholtz resonators, representing the high- and low water states. The piecewise linear Helmholtz oscillator was linearized in order to obtain an analytic expression for the subsequent crossings of the Poincaré plane, but turned out to be only applicable for too small amplitudes of oscillation. Such analytic expression

should give insight to what parameters are relevant for bifurcations to occur in the system's parameter space. Assuming small *derivatives* ($\dot{\zeta}$), rather than amplitudes (ζ) might give a better linearization without having a too small domain of applicability.

The original analytic model for the piecewise linear Helmholtz oscillator has too many parameters to map its behavior properly, but certain sets of parameters already show period-adding bifurcations. These are indications of nonlinear behavior that possibly leads to a chaotic response. After mapping the complete range of interest using *one* nonlinearity parameter, placing of the Mok Bay in this regime will show whether chaotic behavior could be present in the Mok Bay. Extended measurements can in turn show the actual presence (or absence) of this behavior, of which especially the oscillating flow is of importance for estuarine flushing and consequently to the local ecosystem. Furthermore, already this first attempt to find a chaotic response to (assumed deterministic) tidal forcing in a natural estuary showed promising results, both from measurements and further simulations. This gives rise to the question whether many more tidal estuaries behave in a similar unexpected nonlinear fashion.

Chapter 8

Aknowledgements

Even in this 9-month thesis many parties were involved, which I would like to thank here. Of course my supervisors Leo, Henrik, Janine and Sjoerd for all explanations, help and practical advices;

The department of Marine Technology, especially Jan-Dirk, for their custom made frameworks and help at the drop-off and collecting of the equipment;

The Joost Dourlein Amphibious Training Camp Texel for their corporation, permission for our many visits and the opportunity to mount equipment in their harbor;

The team of Matthieu, Roeland and Sierd from Delft University of Technology / SHORE monitoring for their 2-day visit and effort to chart the Mok Bay using their echo sounder-equipped jet ski;

Roland Nauw for his effort to prepare the radio controlled (GPS equipped) boat for our attempt to locate the oyster beds;

The colleagues at Physical Oceanography, especially Anna, Carola, Jenny, Femke and Sjoerd for the many relativizing cups of coffees and dinners;

Appendix A

Photographs

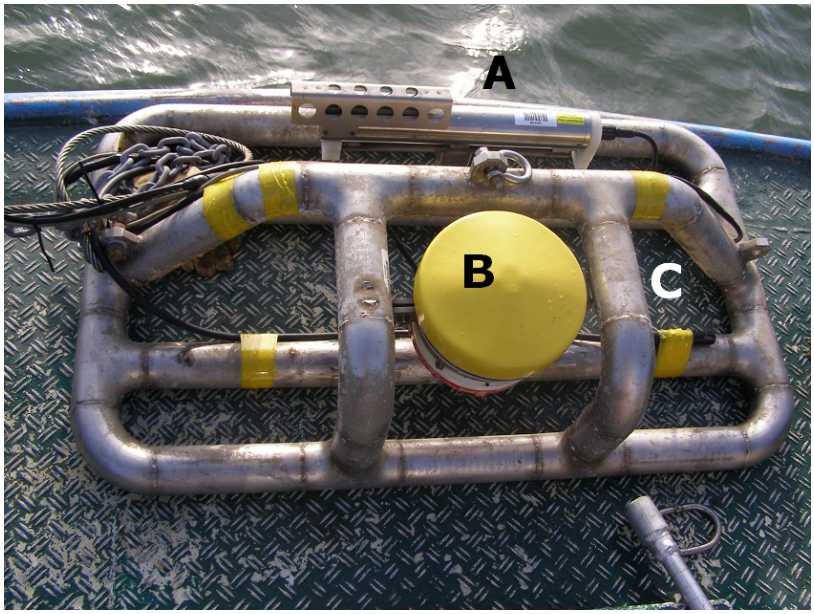

Figure A.1: Aluminum frame on deck of R.V. Stern, including the mounted CTD (A), ADCP (B) and OBS (C).

Figure A.2: Picture of the box with communication electronics as mounted at the MK-2 beacon (yellow, bottom). Visible are the step-by-step guide for connecting the electronics (yellow, left) and battery pack in the lower half of the box.

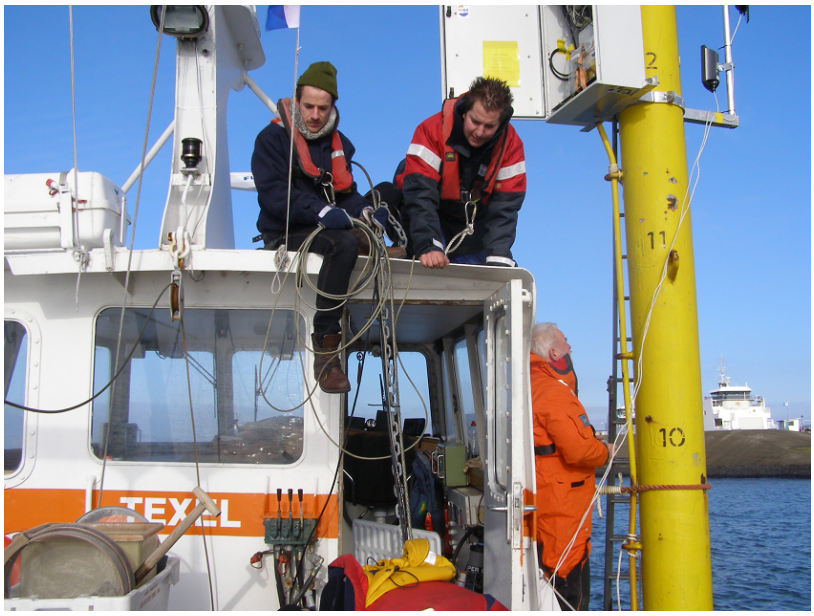

Figure A.3: Preparation of the electronics before the actual drop-off of the frame. In this picture (clockwise from upper-left corner): Jordy de Boer, Jan-Dirk de Visser, Jack Schilling and Ewout Adriaans (bottom).

Figure A.4: Aluminum frame with electronics moments before drop-off. Yellow cover protects the ADCP transducer faces and was removed before actual measurements.

Figure A.5: Radio-controlled (fish-feeding) boat equipped with GPS to chart the oyster beds (bottom half). This was only partly successful due to battery capacity and difficulties when stranding.

Appendix B

Non-dimensionalization of the Helmholtz equation

Starting with the momentum equation integrated over the strait's length L,

$$L\frac{\mathrm{d}u}{\mathrm{d}t_*} = g(\zeta_i - \zeta_e) + \frac{1}{2}(u_i^2 - u_e^2) - L\frac{k}{H}|u|u \tag{B.1}$$

and the basin's excess volume

$$\frac{\mathrm{d}V_*}{\mathrm{d}t_*} = -uHB,$$

the non-dimensional parameters

$$V_* = A_o HV, \quad t_* = t/\sigma_H, \quad \sigma_H^2 = gHB/A_0 L, \tag{B.2}$$

and

$$\zeta_i = H\zeta, \quad \zeta_e = HZ_e, \tag{B.3}$$

are substituted. Use the expression for the excess volume and B.2 to obtain a dimensionless expression for the channel velocity u

$$\frac{\mathrm{d}V_*}{\mathrm{d}t_*} = -uHB \quad \longrightarrow \quad u \quad = -\frac{\mathrm{d}V_*}{\mathrm{d}t_*}\frac{1}{HB} = -\frac{\mathrm{d}V}{\mathrm{d}t}\frac{HA_0}{HB\frac{1}{\sigma_H}} = \quad -\frac{\mathrm{d}V}{\mathrm{d}t}\frac{A_0\sigma_H}{B}$$

and its time derative

$$\frac{\mathrm{d}u}{\mathrm{d}t_*} \quad = -\frac{\mathrm{d}^2V_*}{\mathrm{d}t_*^2}\frac{1}{HB} = -\frac{\mathrm{d}^2V}{\mathrm{d}t^2}\frac{HA_0}{HB\frac{1}{\sigma_H^2}} = -\frac{\mathrm{d}^2V}{\mathrm{d}t^2}\frac{HA_0gHB}{A_0HBL} = \quad -\frac{\mathrm{d}^2V}{\mathrm{d}t^2}\frac{gH}{L}.$$

The first term of B.1 can now be made dimensionless as

$$L\frac{\mathrm{d}u}{\mathrm{d}t_*} \quad = -L\frac{\mathrm{d}^2V}{\mathrm{d}t^2}\frac{gH}{L} = \quad -gH\frac{\mathrm{d}^2V}{\mathrm{d}t^2} \tag{B.4}$$

Caused by the water level difference over the strait (or, pipe), the pressure difference can now be written as

$$g(\zeta_i - \zeta_e) \quad = g(H\zeta - HZ_e(\sigma t)) = \quad gH\zeta(V) - gHZ_e(\sigma t). \tag{B.5}$$

Note that now the inverse relation $\zeta = \zeta(V)$ is used, in stead of $V = V(\zeta)$ as in 2.16, and σ is the scaled frequency σ_e/σ_H. The water level overshoot that restores the system (first term on RHS) will be taken to the left hand side, and the tidal forcing (second term on RHS) we have now made dimensionless too.

The radiation damping term is by Maas (1997) introduced as simply being

$$gHr\frac{\mathrm{d}V}{\mathrm{d}t}, \tag{B.6}$$

where

$$r = \frac{\sigma B}{2L}.$$

The dynamic pressure $\frac{1}{2}(u_i^2 - u_e^2)$ over the strait was already derived in the text, and is now combined with the (also quadratic) bottom friction. The dimensionless form of this is obtained by substituting

$$\frac{1}{2}(u_i^2 - u_e^2) \quad = \quad -\delta|u|u$$

together with the bottom friction term $-L\frac{k}{H}|u|u$ as

$$-\left(\delta + L\frac{k}{H}\right)|u|u \quad = -L\left(\frac{\delta}{L} + \frac{k}{H}\right)|u|u = \quad -L\left(\frac{\delta}{L} + \frac{k}{H}\right)\left|\frac{\mathrm{d}V}{\mathrm{d}t}\right|\frac{\mathrm{d}V}{\mathrm{d}t}\frac{A_0^2\sigma_H^2}{B^2}.$$

In short,

$$-\left(\delta + L\frac{k}{H}\right)|u|u \quad = \quad gH\gamma\left|\frac{\mathrm{d}V}{\mathrm{d}t}\right|\frac{\mathrm{d}V}{\mathrm{d}t}, \tag{B.7}$$

where

$$\gamma = \left(\frac{\delta}{L} + \frac{k}{H}\right)\frac{A_0}{B}.$$

Changing sign in and taking out gH from every term (B.4, B.5, B.6 and B.7), we now can write the final dimensionless expression for a Helmholtz resonator in terms of the excess volume $V(t)$:

$$\frac{\mathrm{d}^2V}{\mathrm{d}t} + \zeta(V) = Z_e(\sigma t) - r\frac{\mathrm{d}V}{\mathrm{d}t} - \gamma\left|\frac{\mathrm{d}V}{\mathrm{d}t}\right|\frac{\mathrm{d}V}{\mathrm{d}t}. \tag{B.8}$$

Appendix C

Derivation of the Harmonic Analysis

The discrete time series of a measurement $x(t_n)$, n=1, ..., N can be splitted into

$$x(t_n) = \overline{x} + x'(t_n) = \overline{x} + \hat{x}(t_n) + x_r(t_n) \tag{C.1}$$

where x is the measured value, $\overline{x}$ is the record mean and x' is a fluctuation. This fluctutation can in turn be replaced by a least squares harmonic analysis (LSHA) approximation $\hat{x}$ and a residual x_r. To avoid inaccuracies due to round-off errors, the mean value $\overline{x}$ of the record is subtracted, resulting in

$$x'(t_n) = \hat{x}(t_n) + x_r(t_n) = C + \sum_{q=1}^{M} C_q \cos(2\pi f_q t_n - \phi_q) + x_r(t_n). \tag{C.2}$$

Since the mean of measured fluctuations $\langle x'(t) \rangle$ is per definition zero, the following holds:

$$\left\langle x'(t_n) \right\rangle = 0 = \langle C \rangle + \left\langle \sum_{q=1}^{M} C_q \cos(2\pi f_q t_n - \phi_q) + x_r(t_n) \right\rangle. \tag{C.3}$$

Using $\langle C \rangle = C$,

$$C = -\left\langle \sum_{q=1}^{M} C_q \cos(2\pi f_q t_n - \phi_q) + x_r(t_n) \right\rangle. \tag{C.4}$$

in which C is thus the negative mean value of the LSHA fit and residual together. Assuming a good LSHA fit (i.e. a small residual x_r),

$$C = - < \sum_{q=1}^{M} C_q \cos(2\pi f_q t_n - \phi_q) > . \tag{C.5}$$

Physically this stands for the flux (when analyzing velocity) due to uncomplete cycles of sinusoids, which does *not* contribute to a possible total flux in the measurement site. The total flux in that case would be found by adding both $\overline{x}$ and C. The summation term in (5.2) is a best fit by the LSHA which approximates $\hat{x}$. C_q, f_q and ϕ_q are the constant amplitude, frequency and phase of the qth constituent respectively. Apart from non-stationary behaviour in the present constituents, it is the residual x_r that contains information on the local (estuarine) behavior. Substituting

$$C_q = (A_q^2 + B_q^2)^{1/2}, \quad \phi_q = \tan^{-1}(B_q/A_q), \quad C = A_0 \tag{C.6}$$

into (5.2), one finds

$$x'(t_n) = A_0 + \sum_{q=1}^{M} \left[A_q \cos(2\pi f_q t_n) + B_q \sin(2\pi f_q t_n)\right] + x_r(t_n), \tag{C.7}$$

in which the coefficients A_q and B_q are now to be determined.

The target of the LSHA is to minimize the variance, e^2, of the residual time series $x_r(t_n)$, which is defined as

$$e^2 = \sum_{n=1}^{N} x_r^2(t_n) = \sum_{n=1}^{N} \left\{ x'(t_n) - \left[A_0 + \sum_{q=1}^{M} M(t_n) \right] \right\}^2 \tag{C.8}$$

where

$$M(t_n) = \left[A_q \cos(2\pi f_q t_n) + B_q \sin(2\pi f_q t_n)\right].$$

Minimizing the variance means finding zeros for the partial deratives of the variance to both A_q and B_q. Setting the partial deratives to zero and using the chain rule,

$$\frac{\partial e^2}{\partial A_0} = 0 = 2\sum_{n=1}^{N} \left[\left\{ x'_n - \left[A_0 + \sum_{q=1}^{M} M(t_n) \right] \right\} [1] \right]$$

$$\frac{\partial e^2}{\partial A_q} = 0 = 2\sum_{n=1}^{N} \left[\left\{ x'_n - \left[A_0 + \sum_{q=1}^{M} M(t_n) \right] \right\} [-\cos(2\pi f_q t_n)] \right]$$

$$\frac{\partial e^2}{\partial B_q} = 0 = 2\sum_{n=1}^{N} \left[\left\{ x'_n - \left[A_0 + \sum_{q=1}^{M} M(t_n) \right] \right\} [-\sin(2\pi f_q t_n)] \right] \tag{C.9}$$

One constituent simplification

To show how this can be solved by matrix inversion, we assume only one tidal constituentset, $M = 1$. Then,

$$\frac{\partial e^2}{\partial A_0} = 0 = 2\sum_{n=1}^{N}\left\{x'_n - (A_0 + [A_1\cos(2\pi f_1 t_n) + B_1\sin(2\pi f_1 t_n)])\right\}.$$

$$\frac{\partial e^2}{\partial A_1} = 0 = 2\sum_{n=1}^{N}\left[\left\{x'_n - (A_0 + [A_1\cos(2\pi f_1 t_n) + B_1\sin(2\pi f_1 t_n)])\right\}[-\cos(2\pi f_1 t_n)]\right]$$

$$\frac{\partial e^2}{\partial B_1} = 0 = 2\sum_{n=1}^{N}\left[\left\{x'_n - (A_0 + [A_1\cos(2\pi f_1 t_n) + B_1\sin(2\pi f_1 t_n)])\right\}[-\sin(2\pi f_1 t_n)]\right]$$

Substituting

$$c = \cos(2\pi f_1 t_n), \quad s = \sin(2\pi f_1 t_n), \quad A_0 = \overline{x} \tag{C.10}$$

and bringing all constants outside the summations gives

$$A_0\sum_{n=1}^{N} 1 + A_1\sum_{n=1}^{N} c + B_1\sum_{n=1}^{N} s = \sum_{n=1}^{N} x'_n.$$

$$A_0\sum_{n=1}^{N} c + A_1\sum_{n=1}^{N} c^2 + B_1\sum_{n=1}^{N} sc = \sum_{n=1}^{N} x_n c$$

$$A_0\sum_{n=1}^{N} s + A_1\sum_{n=1}^{N} sc + B_1\sum_{n=1}^{N} s^2 = \sum_{n=1}^{N} x'_n s$$

This, in turn, can be rewritten to the matrix equation $\mathbf{Ax} = \mathbf{b}$, where

$$\underline{\underline{A}} = \begin{bmatrix} \sum_{n=1}^{N} 1 & \sum_{n=1}^{N} c & \sum_{n=1}^{N} s \\ \sum_{n=1}^{N} c & \sum_{n=1}^{N} c^2 & \sum_{n=1}^{N} sc \\ \sum_{n=1}^{N} s & \sum_{n=1}^{N} sc & \sum_{n=1}^{N} s^2 \end{bmatrix}, \tag{C.11}$$

$$\underline{x} = \begin{bmatrix} A_0 \\ A_1 \\ B_1 \end{bmatrix}, \tag{C.12}$$

and

$$\underline{b} = \begin{bmatrix} \sum_{n=1}^{N} x'_n \\ \sum_{n=1}^{N} x'_n c \\ \sum_{n=1}^{N} x'_n s \end{bmatrix}. \tag{C.13}$$

Inverting $\mathbf{A}$, one can solve the system

$$\underline{x} = \underline{\underline{A}}^{-1}\underline{b} \tag{C.14}$$

for the coefficients A_0, A_1 and B_1. These are the desired constants describing the contribution of each constituent to the quantity on which the LSHA is applied.

M-constituents

For a LSHA with one constituent, the dimension of $\mathbf{A}$ is 3×3, which increases as $(2M+1)\times(2M+1)$ for M constituents. This can be explained by the fact that $\overline{x}$ or, A_0, appears only once in every equation. So this contribution does not increase for increasing M, whereas A_q and B_q both appear M times. The vectors $\mathbf{x}$ and $\mathbf{b}$ increase on the same ground to length $(2M+1)$:

$$\underline{\underline{A}} = \begin{bmatrix} N & c_1 & c_2 & \dots & c_m & s_1 & s_2 & \dots & s_m \\ c_1 & cc_{11} & cc_{12} & \dots & cc_{1M} & cs_{11} & cs_{12} & \dots & cs_{1M} \\ c_2 & cc_{21} & cc_{22} & \dots & cc_{2M} & cs_{21} & cs_{22} & \dots & cs_{2M} \\ \vdots & \vdots & \vdots & \ddots & \vdots & \vdots & \vdots & \vdots & \vdots \\ c_M & cc_{M1} & cc_{M2} & \dots & cc_{MM} & cs_{M1} & cs_{M2} & \dots & cs_{MM} \\ s_1 & sc_{11} & sc_{12} & \dots & sc_{1M} & ss_{11} & ss_{12} & \dots & ss_{1M} \\ s_2 & sc_{21} & sc_{22} & \dots & sc_{2M} & ss_{21} & ss_{22} & \dots & ss_{2M} \\ \vdots & \vdots & \vdots & \vdots & \vdots & \vdots & \vdots & \ddots & \vdots \\ s_M & sc_{M1} & sc_{M2} & \dots & sc_{MM} & ss_{M1} & ss_{M2} & \dots & ss_{MM} \end{bmatrix} \tag{C.15}$$

$$\underline{x} = \begin{bmatrix} A_0 \\ A_1 \\ A_2 \\ \vdots \\ A_M \\ B_1 \\ B_2 \\ \vdots \\ B_M \end{bmatrix}, \quad \underline{b} = \begin{bmatrix} yc_0 \\ yc_1 \\ yc_2 \\ \vdots \\ yc_M \\ ys_1 \\ ys_2 \\ \vdots \\ ys_M \end{bmatrix}. \tag{C.16}$$

For visualization reasons, a few substitutions have been done:

$$c_i = \sum_{n=1}^{N} [\cos(2\pi f_i t_n)], \quad s_i = \sum_{n=1}^{N} [\sin(2\pi f_i t_n)]$$

$$cc_{ij} = cc_{ji} = \sum_{n=1}^{N} [\cos(2\pi f_j t_n)\cos(2\pi f_i t_n)]$$

$$ss_{ij} = ss_{ji} = \sum_{n=1}^{N} [\sin(2\pi f_j t_n)\sin(2\pi f_i t_n)]$$

$$cs_{ij} = sc_{ji} = \sum_{n=1}^{N} [\sin(2\pi f_j t_n)\cos(2\pi f_i t_n)],$$

and

$$yc_i = \sum_{n=1}^{N} x'_n [\cos(2\pi f_i t_n)], \quad ys_i = \sum_{n=1}^{N} x'_n [\sin(2\pi f_j t_n)].$$

After solving the matrix system (C.14) all coefficients A_q and B_q are now known. Using (C.6), these can be transformed back into q specific amplitudes and phases which together form the best LSHA fit of the measured data.

Appendix D

Analytic derivation of the inviscid and viscous response

D.1 Inviscid response

For now, the inviscid form (i.e. $r = \gamma = 0$) of (2.18) is used for a simplified model of this parametric oscillator:

$$\frac{\mathrm{d}^2 V}{\mathrm{d}t^2} + \zeta(V) = \zeta_e(t). \tag{D.1}$$

The tidal forcing $\zeta_e(t)$ is a single-frequency forcing: $\zeta_e(t) = F_0 \cos(\omega t)$. Using $V = \zeta A$ and a solution of the form

$$\zeta = a \sin(\omega t) + b \cos(\omega t) \tag{D.2}$$

this can be rewritten to

$$-A_i a \omega^2 \sin(\omega t) - A_i b \omega^2 \cos(\omega t) + a \sin(\omega t) + b \cos(\omega t) = F_0 \cos(\omega t). \tag{D.3}$$

Here A_i is the instantaneous surface area (at high- or low water state), a and b are to be determined. Since the forcing of the inviscid system consists of only a cosine term (with frequency ω being equal in all terms), it follows that $a = 0$. Consequently b can be determined to be

$$b = \frac{F_0}{1 - A_i \omega^2}. \tag{D.4}$$

The particular solution to the second order differential equation (the homogeneous part is zero for this inviscid system) is in the general form

$$\zeta(t) = c_1 \sin(\omega_0 t) + c_2 \cos(\omega_0 t) + b \cos(\omega t). \tag{D.5}$$

The system's eigen frequency is $\omega_0 = \sqrt{1/A}$ and the coefficients c_1 and c_2 are determined from the initial conditions ($\zeta(0) = 0, \dot{\zeta}(0) = 0$) by solving the matrix equation

$$Cx = D. \tag{D.6}$$

Here

$$C = \begin{bmatrix} \sin(\omega_0 t) & \cos(\omega_0 t) & \cos(\omega t) \\ \omega_0 \cos(\omega t) & -\omega_0 \sin(\omega_0 t) & -\omega \sin(\omega t) \\ 0 & 0 & 1 \end{bmatrix}, \quad x = \begin{bmatrix} c_1 \\ c_1 \\ b \end{bmatrix}$$

and

$$D = \begin{bmatrix} \zeta(0) \\ \dot{\zeta}(0) \\ b \end{bmatrix} = \begin{bmatrix} 0 \\ 0 \\ b \end{bmatrix}.$$

At every switch between ebb and flood (and vice versa) the system (D.6) is solved again for x since it now has new system parameters. The condition of the bay at the switch is used as initial conditions for this new solution.

Continuity between two states requires that both the water surface level and volume transport through the channel (modelled as a pipe) are continuous: $\zeta^- = \zeta^+$ and $Q^- = Q^+$, where Q denotes the channel flow. Superscripts indicate the instants before ($^-$) and after ($^+$) switch of states. Using the fact that the inflow is related to surface area A as $Q = \dot{\zeta} A$, the following should be satisfied:

$$\zeta^+ = \zeta^-, \qquad \dot{\zeta}^+ = \dot{\zeta}^- \frac{A^-}{A^+}. \tag{D.7}$$

Obviously the surface area experiences a sudden jump, it is a step function. Satisfying $\dot{\zeta}^+ = \dot{\zeta}^-$ would cause a discontinuity in the water flow through the channel. The sudden increase in surface area demands a sudden increase of flow and thus $Q^+ \neq Q^-$. By setting the sudden change in $\dot{\zeta}$ equal to the increase in area, a continuous flow through the channel is obtained. For as long as the bathymetry is not defined as a continuous function, this is a proper continuity relation.

Knowing the initial conditions, an exact solution of the water level (or excess volume) can be calculated separately for each LW and HW. As soon as the water surface area switches to its new value, an exact derivative can be calculated and used as new initial condition. This results in an exact representation of the inviscid stepwise-linear oscillator.

D.2 Viscous response

If one *does* include friction and assumes only linear dissipation (neglecting the last term on the RHS in equation 2.18), the standard solution to the widely documented mass-spring system can be used here. Leaving quadratic friction out, (2.18) becomes

$$\frac{\mathrm{d}^2 V}{\mathrm{d}t^2} + \zeta(V) = Z_e(\sigma t) - r\frac{\mathrm{d}V}{\mathrm{d}t}. \tag{D.8}$$

Substitute $Z_e(\sigma t) = \zeta_e(t) = F_0 \cos(\omega t - \phi_d)$ and $V = \zeta A$ to find

$$A\frac{\mathrm{d}^2\zeta}{\mathrm{d}t^2} + rA\frac{\mathrm{d}\zeta}{\mathrm{d}t} + \zeta = F_0 \cos(\omega t - \phi_d). \tag{D.9}$$

This is similar to the equation of motion for a forced, viscous mass-spring system:

$$m\frac{\mathrm{d}^2x}{\mathrm{d}t^2} + c\frac{\mathrm{d}x}{\mathrm{d}t} + kx = F_0 \cos(\omega t - \phi_d). \tag{D.10}$$

Here, x represents the system's excitation, k is the spring constant and c the damping constant. Subscript d indicates that the phase is related to the driving force, time t is explicitly related to the forcing.

D.2.1 General solution

The solution to (D.10) consists in its general form of a transient and a steady-state solution (or, homogenous and particular solution respectively). By the use of boundary conditions this general solution can be applied to the problem of concern to find the exact solution. Initial conditions decay over time as described by the transient solution, after which a state is reached for which both phase and amplitude are constant. In the case of coupled linear oscillators, consisting of two such systems as described by (D.10), the transient solution might be of importance continuously.

Transient solution

The transient solution is described by the equation of motion when no forcing is applied, i.e. the RHS of (D.10) is equal to zero:

$$m\frac{\mathrm{d}^2x}{\mathrm{d}t^2} + c\frac{\mathrm{d}x}{\mathrm{d}t} + kx = 0 \tag{D.11}$$

A decaying solution is expected, for which the form $x = e^{rt}$ is used. Note that r is different from the damping parameter in D.9. Inserting this in (D.10) yields

$$mr^2e^{rt} + cre^{rt} + ke^{rt} = 0,$$

for which $x = e^{rt}$ only is a solution if r satisfies the auxiliary equation

$$mr^2 + cr + k = 0.$$

This equation has roots given by

$$r = \frac{-c}{2m} \pm \frac{\sqrt{D}}{2m},$$

where $D = c^2 - 4mk$. The system is said to be overdamped if $D > 0$, critically damped if $D = 0$ and underdamped when $D < 0$. For the Mok Bay we assume an underdamped system ($D < 0$), so the roots are complex:

$$r = -\gamma \pm i\omega',$$

where $\omega' = \sqrt{\omega_0^2 - \gamma^2}$ and $\gamma = c/2m$. The found values for γ and ω' can now be used in the general form of the homogeneous solution:

$$x_h(t) = C_1 e^{-\gamma t}\cos(\omega' t) + C_2 e^{-\gamma t}\sin(\omega' t). \tag{D.12}$$

Substituting $C_1 = A_h \sin(\phi_h)$, $C_2 = A_h \cos(\phi_h)$ and making use of the trigonometric relation

$$\sin(\alpha)\cos(\beta) + \cos(\alpha)\sin(\beta) = \sin(\alpha + \beta),$$

the following expression for the homogeneous solution is found.

$$x_h(t) = A_h e^{-\gamma t}\sin(\omega' t + \phi_h) \tag{D.13}$$

Both the amplitude A_h and phase ϕ_h will be determined using boundary conditions.

Steady-state solution

After the transient solution has decayed, the system responds 'fixed' with respect to the periodic forcing. Both the amplitude and phase are now constant, i.e. the steady-state (or, particular) solution. Again one starts with the equation of motion for the viscous mass-spring system, now having a periodic forcing:

$$m\frac{\mathrm{d}^2x}{\mathrm{d}t^2} + c\frac{\mathrm{d}x}{\mathrm{d}t} + kx = F_0\cos(\omega t - \phi_d) \tag{D.14}$$

The 'complex variables method' introduces an imaginary part to the equation, after which only the real part of the solution is used. For the current equation of motion this yields:

$$\begin{aligned} m\frac{\mathrm{d}^2x}{\mathrm{d}t^2} + c\frac{\mathrm{d}x}{\mathrm{d}t} + kx &= F_0\left[\cos(\omega t - \phi_d) + i\sin(\omega t - \phi_d)\right] \\ &= F_0 e^{i(\omega t - \phi_d)}. \end{aligned} \tag{D.15}$$

Assume a solution of the form $x(t) = A_p e^{i(\omega t - \phi)}$, then (D.15) can be rewritten as

$$-\omega^2 m A_p e^{i(\omega t - \phi)} + i\omega c A_p e^{i(\omega t - \phi)} + k A_p e^{i(\omega t - \phi)} = F_0 e^{i(\omega t - \phi_d)}. \tag{D.16}$$

Dividing both sides by the exponential as used on the LHS results in the auxiliary equation:

$$\begin{aligned} -\omega^2 m A_p + i\omega c A_p + k A_p &= F_0 e^{i(\phi-\phi_d)} \\ &= F_0 \left(\cos(\phi-\phi_d) + i\sin((\phi-\phi_d))\right). \end{aligned} \tag{D.17}$$

The real and imaginary part of this equation can be solved separately to find

$$F_0 \cos(\phi-\phi_d) = A_p(k - m\omega^2)$$
$$F_0 \sin(\phi-\phi_d) = \omega c A_p.$$

This can in turn be used to find the amplitude A_p and phase ϕ of the steady-state part of the solution (particular solution). Using $\cos^2(\phi) + \sin^2(\phi) = 1$ and solving for A_p and ϕ yields

$$A_p = \frac{F_0/m}{\sqrt{(\omega_0^2 - \omega^2)^2 + 4\gamma^2\omega^2}} \tag{D.18}$$

$$(\phi - \phi_d) = \tan^{-1}\left(\frac{\omega c}{k - m\omega^2}\right).$$

Here $\gamma = c/2m$ and $\omega_0^2 = k/m$. The particular solution can now be written as

$$x_p(t) = A_p \cos(\omega t - \phi), \tag{D.19}$$

where

$$\phi = \tan^{-1}\left[\frac{c\omega}{k - m\omega^2}\right] + \phi_d. \tag{D.20}$$

The general solution to (D.10) is simply the sum of the homogenous and particular solution:

$$x(t) = A_h e^{-\gamma t} \sin\left(\omega' t + \phi_h\right) + A_p \cos\left(\omega t - \phi\right), \tag{D.21}$$

consisting of a decaying homogeneous solution (first term on RHS, subscript h) and a steady-state particular solution (second term on RHS, subscript p).

D.2.2 Exact solution

To obtain the exact solution for the water level $x(t)$ (or ζ in D.9), the boundary conditions are used to find expressions for A_h and ϕ_h in the homogeneous part of the general solution. Boundary conditions at $t = t_{bc}$ dictate $x = x_{bc}$ and $\frac{\mathrm{d}x}{\mathrm{d}t}|_{t=t_{bc}} = v_{bc}$. Using equation D.21 one finds

$$A_h = \frac{x_{bc} - A_p \cos(\omega t_{bc} - \phi)}{e^{-\gamma t_{bc}} \sin(\omega' t_{bc} + \phi_h)}. \tag{D.22}$$

The derivative of equation D.21 can be found using the product rule, and is expressed as

$$\frac{\mathrm{d}x}{\mathrm{d}t} = -\gamma A_h e^{-\gamma t} \sin(\omega' t + \phi_h) + A_h e^{-\gamma t} \omega' \cos(\omega' t + \phi_h) - \omega A_p \sin(\omega t - \phi). \tag{D.23}$$

Using the fact that

$$\tan(\omega' t_{bc} + \phi_h) = \frac{A_h e^{-\gamma t_{bc}}}{A_h e^{-\gamma t_{bc}}} \frac{\sin(\omega' t_{bc} + \phi_h)}{\cos(\omega' t_{bc} + \phi_h)},$$

and the equations (D.21) and (D.23) at $t = t_{bc}$, the expression for ϕ_h is found as

$$\phi_h = \tan^{-1}\left[\frac{\omega'(x_{bc} - A_p \cos(\omega t_{bc} - \phi))}{v_{bc} + \gamma(x_{bc} - A_p \cos(\omega t_{bc} - \phi) + A_p \omega \sin(\omega t_{bc} - \phi)}\right] - \omega' t_{bc}. \tag{D.24}$$

To use the widely documented solution for a viscous mass-spring system for the Helmholtz resonator, one uses $x = \zeta$, $m = A$, $c = rA$ and $k = 1$ (equation D.9 and D.10). The set of equations ((D.18), (D.20), (D.21), (D.22) and (D.24)) gives an analytic expression to the solution of the viscous Helmholtz oscillator, albeit in a very general way.

Appendix E

Nomenclature

E.1 Symbols

A	The water surface area
A_0	*idem*, at zero surface elevation from mean sea level
A_*	Dimensionless water surface area
A_h	Amplitude (homogeneous solution)
A_p	Amplitude (particular solution)
B	Channel width
c	Damping constant
C	Sample mean value
C_q	Amplitude of qth constituent
e	Euler exponent
f_f	Fundamental frequency
f_N	Nyquist frequency
f_q	Frequency of qth constituent
f_s	Sampling frequency
Δf	Frequency resolution
$f_{1/2}$	Half-power frequency
g	Gravitational acceleration
H	Channel depth
H_*	Dimensionless channel depth
J_n	n^{th} Bessel function of first kind
k	Spring stiffness constant
L	Channel length
L_E	Effective channel length
m	Mass
M	Number of constituents
N	Number of measurements

p	Pressure
Q	Quality factor
r	Friction parameter
R	Reflection coefficient
Δt	Time resolution
t	Time
t_e	Time (external forcing)
T	Period ($1/f$)
T_f	Fundamental period
u_e	External flow velocity
u_i	Internal flow velocity
u_0	Channel-averaged flow velocity
U_0	Free-stream velocity
$\mathbf{u}$	Velocity vector
v_E	Eastward velocity
v_N	Northward velocity
v_{al}	Alongstream velocity
v_{bc}	Time derative of water level (boundary condition)
v_{cr}	Crossstream velocity
V_*	Dimensionless volume
x	Water level excitation (Chapter 6)
x	Measured quantity (Chapter 5)
x_bc	Water level (boundary condition)
z	Vertical coordinate
z_*	Dimensionless vertical coordinate
Z_e	Amplitude of external water level forcing
α	Coordinate rotation angle
γ	Friction parameter (Chapter 2)
γ	Growth rate (Chapter 5)
δ	Proportionality constant (Chapter 2)
ϵ	Proportionality constant (Chapter 2)
ϵ	Proportionality constant (Chapter 6)
ϵ	Residual (Chapter 5)
ε	Residual (Chapter 5)
ζ	Water level elevation from mean sea level
ζ_*	Dimensionless water level elevation
ζ_e	External water level elevation
ζ_i	Internal water level elevation
λ	Wave length
μ	Dynamic viscosity

ν	Kinematic viscosity
τ	Shear stress
τ_{lam}	Shear stress by laminar flow
τ_{turb}	Shear stress by turbulent flow
ρ	Density
σ	Frequency of forcing
σ_H	Helmholtz frequency
ϕ	Phase
ϕ_d	Phase of external forcing
ϕ_h	Phase of homogeneous solution
ϕ_p	Phase of particular solution
ϕ_q	Phase of qth constituent
∇	Gradient operator
ω	Frequency
ω_n	Basin eigen frequency (for waterlevel $\zeta < 0$)
ω_p	Basin eigen frequency (for waterlevel $\zeta > 0$)
ω_0	Basin eigen frequency

E.2 Abbreviations

ADCP	Acoustic Doppler current profiler
cpd	Cycles per day
CCW	Counter clockwise
CTD	Conductivity, Temperature, Depth meter
CW	Clockwise
FFT	Fast Fourier Transform
GPS	Global Positioning System
LAN	Local Area Network
LSHA	Least squares harmonic analysis
N.A.P.	Normaal Amsterdams Peil, Amsterdam Reference Level
NIOZ	Netherlands Institute for Sea Research
OBS	Optical backscatter meter
PSU	Practical Salinity Unit
SSE	Sum of squared errors
SST	Sum of squared total
SSF	Sum of squared fit
TUD	Delft University of Technology
UDS	Universal Device Server

Bibliography

Abarbanel, H., Brown, R., Sidorowich, J., and Tsimring, L. (1993). The analysis of observed chaotic data in physical systems. *Reviews of Modern Physics*, **65**(4), 1331–1392.

Adams, R. (2002). *Calculus: a Complete Course.* 4th ed. Pearson Canada Inc.

Beerens, S. (1995). Mixing by chaotic advection in tidal areas. *PhD thesis.*

Bodén, H., Ahlin, K., and Carlsson, U. (2009). *Signaler och Mekaniska System.* World Scientific Publ., Stockholm.

Buijsman, M. and Ridderinkhof, H. (2007). Long-term ferry-ADCP observations of tidal currents in the Marsdiep inlet. *Journal of Sea Research*, **57**(4), 237 – 256.

Cartwright, D. (1999). *Tides, a Scientific History.* Cambridge University Press.

Coombes, S. and Osbaldestin, A. (2000). Period-adding bifurcations and chaos in a periodically stimulated excitable neural relaxation oscillator. *Physical Review E*, **62**(3), 4057–4066.

Cvitanovic, P. (1983). *Universality in Chaos (or, Feigenbaum for cyclists)*, volume 39.

Doelman, A., Koenderink, A. F., and Maas, L. (2002). Quasi-periodically forced nonlinear Helmholtz oscillators. *Physics D*, **164**, 1–27.

Duarte, J., Silva, L., and Ramos, J. (2006). Types of bifurcations of Fitzhugh-Nagumo maps. *Nonlinear Dynamics*, **44**, 231–242.

Emery, W. and Thomson, R. (2001). *Data Analysis Methods in Physical Oceanography.* Elsevier Publishing Company.

Fabrikant, L. (1995). Harbor oscillations generated by shear flow. *Journal of Fluid Mechanics.*, **282**, 203–217.

Flinchem, E. and Jay, D. (2000). An introduction to wavelet transform tidal analysis methods. *Estuarine, Coastal and Shelf Science*, **51**, 177–200.

Frison, T. (2000). Dynamics of the residuals in estuary water levels. *Physics and Chemistry of the Earth (B)*, **25**(4), 359–364.

Golmen, L., Molvaer, J., and Magnusson, J. (1994). Sea level oscillations with super-tidal frequency in a coastal enbayment of western Norway. *Continental Shelf Research*, **14**(13/14), 1439 – 1454.

Grassberger, P. and Procaccia, I. (1983). Measuring the strangeness of strange attractors. *Physica 9D*, pages 189–208.

Groeskamp, S. (2010). Solitary internal waves in marsdiep tidal channel. *Master thesis, Utrecht University.*

Honda, K., Terada, T., Yoshida, Y., and Isitani, D. (1908). An investigation on the secondary undulations of oceanic tides. *Journal College of Science, Imperial University of Tokyo*, **24**, 1–113.

Kennel, M., Brown, R., and Abarbanel, H. (1992). Determining embedding dimension for phase-space reconstruction using a geometrical construction. *Physical Review A*, **45**(6), 3403–3411.

Khokhlov, V., Glushkov, A., Loboda, N., Serbov, N., and Zhurbenko, K. (2007). Signatures of low-dimensional chaos in hourly water level measurements at coastal site of Mariupol, Ukraine. *Stochastic Environmental Research and Risk Assessment*, **22**, 777–787.

Kreuzer, E., Kleczka, M., and Schaub, S. (1991). Chaotic dynamics of a simple oscillator - a pictorial introduction. *Chaos, Solitons & Fractals*, **1**(5), 439–456.

Kundu, P. K. and Cohen, I. M. (2008). *Fluid Mechanics. 4th* ed. Academic Press.

Maas, L. (1997). On the nonlinear Helmholtz response of almost-enclosed tidal basins with sloping bottoms. *Journal of Fluid Mechanics*, **349**, 361–380.

Maas, L. and Doelman, A. (2001). Chaotic tides. *Journal of Physical Oceanography*, **32**, 870–890.

Mooers, C. N. (1999). *Coastal Ocean Prediction.* American Geophysical Union.

Murguia, J. and Campos-Canton, E. (2006). Wavelet analysis of chaotic time series. *Revista Mexicana de Fisica*, **52**(2), 155–162.

Nakano, M. (1957). On the eddies of Naruto Strait. *Meteorological Research Agency*, **7**(4), 425–434.

Nayfeh, A. and Mook, D. (1979). *Nonlinear Oscillations.* John Wiley & Sons, Inc., New York.

Parker, B. (1991). *Tidal Hydrodynamics.* John Wiley & Sons, Inc.

Pope, S. (2000). *Turbulent Flows.* Cambridge University Press.

Rabinovich, A. (2009). *Handbook of Coastal Engineering.* World Scientific Publ., Singapoure.

Sanford, L. (1985). Turbulent mixing in experimental ecosystem studies. *Marine Ecology Progress Series*, **161**, 265–293.

Sano, M. and Sawada, Y. (1985). Measurement of the Lyapunov spectrum from a chaotic time series. *Physical Review Letters*, **55**(10), 1082–1085.

Savikumar, B. (2004). Chaos theory in geophysics: past, present and future. *Chaos, Solitons and Fractals*, **19**, 441–462.

Schreiber, T. (1999). Interdisciplinary application of nonlinear time series methods. *Physics Reports*, **308**, 1–64.

Squires, G. (1993). *Practical physics.* 3rd ed. Cambridge University Press.

Terra, G. (2005). Nonlinear tidal resonance. *PhD thesis, Utrecht University.*

Unesco (1985). The international system of units (SI) in oceanography. report of IAPSO working group on symbols, units and nomenclature in physical oceanography (SUN). *Unesco Technical Papers in Marine Science*, **45**.

Yang, Z. and Lu, Q. (2004). Characteristics of period-adding bursting bifurcation without chaos in the Chay neuron model. *Chinese Physics Letters*, **21**(11), 2124–2127.